UNIVERSITY
OF TRENTO - Italy
Department of Materials Engineering
and Industrial Technologies

XXIV cycle

Doctoral School in Materials Science and Engineering

Molecular Dynamics and X-ray Powder Diffraction Simulations

Investigation of nano-polycrystalline microstructure at the atomic scale coupling *local structure configurations* and *X-ray Powder Diffraction* techniques

Alberto Leonardi

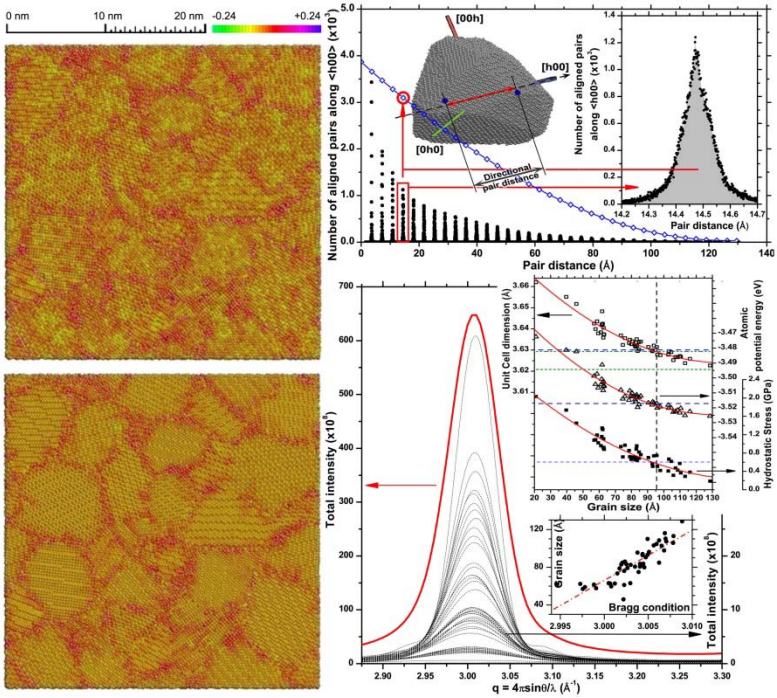

November 2012

MOLECULAR DYNAMICS AND X-RAY POWDER DIFFRACTION SIMULATIONS

INVESTIGATION OF NANO-POLYCRYSTALLINE MICROSTRUCTURE AT THE ATOMIC SCALE COUPLING LOCAL STRUCTURE CONFIGURATIONS AND X-RAY POWDER DIFFRACTION TECHNIQUES

Alberto Leonardi

E-mail: alby_leo@yahoo.it

Approved by:

Prof. Paolo Scardi, Advisor
Department of Materials Engineering and Industrial Technologies
University of Trento, Italy.

Prof. Matteo Leoni
Department of Materials Engineering and Industrial Technologies
University of Trento, Italy.

Ph.D. Commission:

Prof. Alberto Quaranta
Department of Materials Engineering and Industrial Technologies
University of Trento, Italy.

Prof. Rozalya Barabash
Materials Science & Technology Div.
Oak Ridge National Laboratory, Tenneesee (US).

Prof. Marco Milanesio
Department of Science and advanced technologies
University of Piemonte Orientale, Italy.

University of Trento, faculty of engineering

Department of Materials Engineering and Industrial Technologies

November 2012

University of Trento - Department of
Materials Engineering and Industrial Technologies

Doctoral Thesis

Alberto Leonardi - 2012
Published in Trento (Italy) – by University of Trento

ISBN: 978-88-8443-455-5

"The essence of science lies not in discovering facts, but in discovering new ways of thinking about them. “

W. L. Bragg

Abstract

Atomistic simulations based on Molecular Dynamics (MD) were used to model the lattice distortions in metallic nano-polycrystalline microstructures, with the purpose of supporting the analysis of the X-ray powder diffraction patterns with a better, atomic level understanding of the studied system.

Complex microstructures were generated with a new modified Voronoi tessellation method which provides a direct relation between generation parameters and statistical properties of the resulting model. MD was used to equilibrate the system: the corresponding strain field was described both in the core and in surface regions of the different crystalline domains. New methods were developed to calculate the strain tensor at the atomic scale.

Line Profile Analysis (LPA) was employed to retrieve the microstructure information (size and strain effects) from the powder diffraction patterns: a general algorithm with an atomic level resolution was developed to consider the size effects of crystalline domains of any arbitrary shape. The study provided a new point of view on the role of the grain boundary regions in nano-polycrystalline aggregates, exploring the interference effects between different domains and between grain boundary and crystalline regions. Usual concepts of solid mechanics were brought in the atomistic models to describe the strain effects on the powder diffraction pattern. To this purpose the new concept of Directional - Pair Distribution Function (D-PDF) was developed. D-PDFs calculated from equilibrated atomistic simulations provide a representation of the strain field which is directly comparable with the results of traditional LPA (e.g. Williamson-Hall plot and Warren-Averbach method).

The D-PDF opens a new chapter in powder diffraction as new insights and a more sound interpretation of the results are made possible with this new approach to diffraction LPA.

Table of contents

Chapter I

Introduction

Computational Materials Science is one of the newest and most promising branches of science and engineering. Owing to their versatility, computational techniques can be employed both to assess consistency between experiments and theories, and to complement them. For example, predictions can be made by using different models or by implementing different hypothesis, so to find the best experimental conditions under which some known, or new and unexpected phenomena appear ((Zheng, et al., 2010), (Bulatov, et al., 1998), (Greaves, et al., 2011), (Jang, et al., 2012), (Norris, et al., 2011)).

The key modelling tool for nano-structured materials is atomistic simulation: mimicking the behaviour of each atom in a given microstructure can provide information ranging from spatial arrangement (atomic coordinates and displacement in space and time) to energetic properties (from which e.g. temperature, stress, and vibrational spectra can be calculated). Most models, especially the microstructural ones, can be reliable and rigorous even by considering atoms as classical particles (Molecular Dynamics (MD)). Characteristics such as the grain boundary structure can then be evaluated by recording the displacements between a starting ideal crystal and the corresponding equilibrium configuration ((Van Swygenhoven, 2002), (Derlet, et al., 2005), (Frøseth, et al., 2005)).

The increasing power of computers is constantly pushing up the capabilities and limits of MD: ever larger clusters of atoms (i.e. microstructures), can be nowadays equilibrated under a wide variety of imposed environmental conditions. One million atoms can easily be handled by a desktop PC, whereas computer clusters are usually employed for more demanding tasks (several hundred million atoms). Still, transient phenomena are frequently poorly traced (Van Swygenhoven, 2002) and thus the risk is high of a strong biasing of the result by a wrong choice of the starting microstructure. Hence, it is crucial that statistical and physical coherency is kept between simulated microstructure and (as available) experimental results ((Gross, et al., 2002), (Xu, et al., 2009), (Xu, et al., 2010)).

A convenient way to link atomistic simulations and experiments is based on X-ray powder diffraction. In fact, a diffraction pattern contains complete information on a nano-crystalline specimen: roughly speaking, structure (i.e. atomic positions) is encoded in peak position and intensity whereas microstructure dominates the peak breadth and shape. The ability to entangle is left to the reliability of the models employed in data analysis.

The main goal of this work is to couple X-ray powder diffraction and a description of the local atomic arrangement for a better understanding of the nano-polycrystalline microstructure at the atomic scale.

Several limitations of current models need to be removed to reach this goal. First of all the microstructure biasing has to be reduced and in particular, the topological and statistical properties of the initial microstructure need to be similar to experimental (or realistic) ones. Several algorithms have been suggested for polycrystalline microstructure generation, the most common being the Poisson Voronoi Tessellation (PVT), which has the considerable drawback of leading to unrealistic topologies and grain distributions. Suitable constrains can overcome the assumptions of constant uniform growth rate and simultaneous nucleation implied by PVT ((Gross, et al., 2002), (Suzudo, et al., 2009)). Using such evolutionary methods, some features of the simulated polycrystalline microstructures are forced to agree with experimental results (e.g. a log-normal grain size distribution). Still, the resulting microstructure is affected by the geometrical and topological restrictions of the Voronoi construction, such as sphericity, edge or triple junction length, bond and dihedral angles (Xu, et al., 2009). Chapter II presents a new approach to generate microstructures with a desired grain size distribution, which is further extended by an evolutional algorithm to simultaneously obtain a set of properties, like grain shape or volume fill density. Results of this work are then used throughout the rest of the Thesis work.

Chapter III deals with the critical problem concerning the different definition and meaning of strain when macroscopic and atomistic descriptions are compared. An appropriate relation is established between strain in the microstructure (discrete) and the continuous microstrain (or root mean squared (r.m.s.) strain) measurable by

X-ray diffraction. A possible extension of the continuum theory to account for the atomistic nature is proposed and implemented from the available knowledge of atomic positions.

X-ray diffraction can provide information on both structure and microstructure of materials. The latter is the focus of the so-called Line Profile Analysis (LPA), so much used in nearly all areas of science and technology to determine size of the crystalline domains and content of lattice defects. The same problem, as discussed in the last two chapters, can be viewed by the atomistic modelling, with the considerable advantage that phenomena and features not directly accessible to experiments can also be studied. Chapter IV, focus in particular on the role of grain boundaries, and their contribution to the coherent scattering which determines the observed features of the diffraction peak profiles.

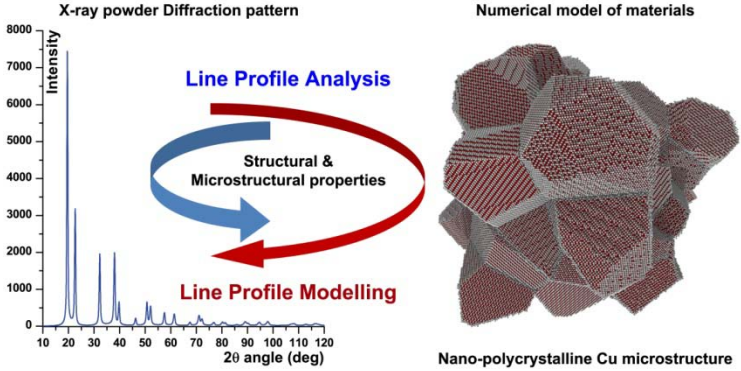

Figure I - 1. Nano-polycrystalline Cu microstructure and the corresponding X-ray powder diffraction pattern.

The broadening of line profiles can be studied in terms of structural and microstructural properties such as domain size and distortion field. X-ray diffraction provides a convenient way to express the results of an MD simulation (either for single crystals or polycrystalline aggregates), as with the Debye Scattering Equation (DSE) ((Debye, 1915), (Cervellino, et al., 2010), (Gelisio, et al., 2010)) no extra assumptions are required to generate the powder pattern from the atomic positions. However, so far DSE patterns from MD simulations have been little studied, using only the most simplified and less reliable tools of traditional LPA ((Derlet, et al., 2005), (Leonardi, et al., 2011)). The lack of appropriate and reliable LPA methods prevents from studying many physical phenomena that can be investigated by an atomistic simulation, e.g., during the MD equilibration process. Chapter VI shows how a new concept of Directional Pair Distribution Function (D-PDF) can be developed from atomistic simulations to interpret and fully understand the diffraction line profiles. This development, as schematically illustrated in Figure (1), allows us to

fully understand the line broadening effect due to the finite size and arbitrary shape of crystalline grains in a microstructure, while at the same time considering the effect of r.m.s. strain on the atomic level.

The proposed approach can be used to validate existing methods, and in particular the Warren-Averbach method ((Warren, et al., 1950), (Warren, 1959), (Warren, et al., 1952)), which is a standard in LPA. More generally, the D-PDF concept supports a better understanding and use of MD simulations, and their relation with real microstructures in terms of a well-known, easy to perform experimental technique like diffraction.

The present Thesis is organized in chapters mapping one or more articles published on (or submitted to) several scientific journals. Each chapter is then presented as a complete research report, comprising a dedicated abstract and paragraphs of introduction, results and discussion, and conclusions. In this way each chapter can be read independently of the others, even if the order of the presentation and the content clearly refer, as a whole, to the same research project briefly introduced above.

Chapter II

Modelling of Material Microstructures

Part of this chapter has been published in:

Alberto Leonardi, Paolo Scardi, Matteo Leoni,

"Realistic nano-polycrystalline microstructures: beyond the classical Voronoi Tessellation",
Philosophical Magazine, 92 – 8 (2012) 986-1005.

Alberto Leonardi, Matteo Leoni, Paolo Scardi,

"Atomistic modelling of polycrystalline microstructures: an evolutional approach to overcome topological restrictions",
Computational Materials Science, 67 (2013) 238-242.

2.1 Abstract

The Modified Voronoi Tessellation (MVT) method is proposed for the computer simulation of realistic microstructures. Differently from standard tessellations, the present method provides a desired grain size distribution in a one-step non-evolutionary procedure. This is obtained by relaxing the constraints of Voronoi Tessellation on position and orientation of the grain boundaries, with the only side effect of forming a limited amount of eliminable voids. As an example, it is shown how to directly obtain a size distribution of grains of given variance and with a shape statistically close to a lognormal.

An evolutional algorithm is then proposed to overcome the topological restrictions of tessellation methods employed for polycrystalline microstructure generation. By suitably tuning the generator parameters, the new algorithm allows the generation of a microstructure simultaneously with e.g. given cell size distribution, cell shape isotropy and volume fill density, impossible to obtain using any of the existing tessellation techniques. The relationship between generation parameters and resulting properties of the size distribution is investigated.

2.2 Introduction

Atomistic modelling is increasingly employed for the study and the prediction of the properties of materials at the nano scale. Starting point of all those studies is a realistic model for the microstructure ((Gleiter, 2000), (Suryanarayana, et al., 2000), (Mahadevan, et al., 2002)) including grain shape and size distribution, chemical composition, atomic positions, as well as specific models of grain boundaries. The microstructure, in fact, plays a key role in determining the mechanical and physical properties of a polycrystalline aggregate ((Zheng, et al., 2005), (Zhu, et al., 2006), (Fátima Vaz, et al., 1988), (Kurzydzsowski, 1990)): a poor microstructure modelling might lead to results that albeit correct, are not representative of a real object (Gross, et al., 2002). Statistical properties are especially relevant: grain arrangement, grain shape and size distributions, as typically observed by a Transmission Electron Microscope, have usually a peculiar behaviour that is far from being random (Liu, et al., 2010) and thus needs to be accurately reproduced.

To simulate a microstructure, a net of connected closed cells should be created. The operation, also known as space tessellation, is not trivial. Several algorithms have been proposed for periodic (Fedorov, 1971), aperiodic ((Mackay, 1982), (Penrose, 1974), (Ishihara, et al., 1986)) and for stochastic tessellation: Delaunay Triangulation (DT - (Delaunay, 1934), (Muche, 1996)), Voronoi Tessellation (VT - (Sibson, 1980), (Aurenhammer, 1991), (Kumar, et al., 1992), (Lucarini, 2009), (Lucarini, 2008), (Thomas, 1996)), Laguerre Tessellation (LT - (Xue, et al., 1997), (Lautensack, et al., 2008)) and Johnson-Mehl Tessellation (JMT - (Farjas, et al., 2008), (Møller, 1992)) are traditionally employed to create interconnected cells with no gaps ((Mahadevan, et al., 2002)). The regularity in periodic and aperiodic tiling seems convenient to describe the atomic arrangement inside grains (e.g. structure of crystals and quasicrystals (Ishihara, et al., 1986)), but is not appropriate to represent a realistic microstructure, as opposed to stochastic tessellations.

Starting point for all stochastic tessellations is a box, in most cases with imposed Periodic Boundary Conditions (PBCs), in which a set of points (centres or generators) is laid. The point creation process and the algorithm generating the associated cells differentiate the various tessellation methods. A homogeneous Poisson point process with parameter λ is a convenient and commonly adopted generator, as it is compatible with the study of aggregates obtained from random nucleation sites ((Lucarini, 2009) , (Lucarini, 2008) , (Meijering, 1953)). Even if modelling inevitably involves the evolution of this microstructure (e.g. by an equilibration process), results can be influenced by the initial configuration ((Zeghadi, et al., 2007(a)), (Zeghadi, et al., 2007(b))) and, in turn, by the tessellation method. An issue is usually to what extent simulated microstructures resemble the

real ones, or are at least capable to capture their main features ((Gleiter, 2000), (Suryanarayana, et al., 2000)).

Voronoi Tessellation (VT) is the most popular in several fields of research ((Baccelli, et al., 2001), (Gilbert, 1962), (van de Weygaert, 1994)) owing to its simplicity ((Tanemura, 1988), (Ferenc, et al., 2007), (Hinde, et al., 1980), (Goldman, 2010)), space-filling nature and to the availability of theoretical results on the topological properties (especially in the case of Poisson-Voronoi Tessellation (PVT)) ((Lucarini, 2009), (Lucarini, 2008), (Meijering, 1953), (Calka, 2003), (Goldman, et al., 2003), (Miles, et al., 1982), (Møller, 1994), (Drouffe, et al., 1984), (Christ, et al., 1982), (Hilhorst, 2005)). Although VT leads to microstructures closely resembling real ones, topological and statistical properties (e.g. dihedral angles, number of triple junctions, area of grain boundaries and junction lengths) are not always compatible with the experimental results (Xu, et al., 2009). For instance, in a PVT the cell volumes follow a distribution close to the gamma ((Fátima Vaz, et al., 1988), (Kumar, et al., 1992)), certainly not the most common in the literature on materials analysis where the lognormal distribution prevails ((Gleiter, 2000), (Suryanarayana, et al., 2000), (Fátima Vaz, et al., 1988), (Rhines, et al., 1982), (Wang, et al., 2007), (Takayama, et al., 1991)). To obtain grains with a different distribution, the available options are to employ a different point process (e.g. Ginibre-Voronoi (Goldman, 2010) or Laguerre-Voronoi ((Yang, et al., 2002), (Fan, et al., 2004), (Wu, et al., 2010)) tessellations), or to start with a traditional VT and to modify the positions of the generators using an evolutionary approach (e.g. Constrained Voronoi Tessellation, CVT ((Gross, et al., 2002), (Xu, et al., 2009)) or the method of Suzudo and Kaburaki (Suzudo, et al., 2009)).

Neither the traditional tessellation algorithms, nor those alternative methods, however, are able to directly produce an ensemble of cells with a lognormal distribution of volumes of arbitrary variance. The CVT has in principle the flexibility to do that for distributions narrower than the PVT, but always with tedious extra computing and at the expenses of the grain shape that becomes arbitrary.

A new method is here proposed, the Modified Voronoi Tessellation (MVT), which eliminates most limitations of traditional tessellations, albeit at the expenses of leaving some voids. To be fully correct, the result is therefore a pattern and not a tessellation. The MVT introduces three additional degrees of freedom (Cell Growth Factors (CGFs), Face Growth Factors (FGFs) and Plane Interface Orientations (PIOs)) to tune the topological properties of the resulting models. The topological properties of the obtained ensemble will be presented and compared with the existing literature. It will be also shown that a distribution of domains possessing a target variance and a shape statistically close to the lognormal can be obtained directly from a random distribution of centres, without the need for extra evolutionary steps.

Unfortunately, a deterministic solution is not yet available to build a microstructure with a desired set of target properties: to this purpose, an evolutional method, defined as Constrained MVT (CMVT) is proposed. Starting from an arbitrary solution, in each iteration step a collection of models is produced by changing selected generator parameters of a grain subgroup. For each model a convergence parameter is computed by applying a penalty function and suitable weight factors. After each step the best model is chosen as the new solution. As shown in the present paper, this approach provides models with desired topological properties, circumventing any restrictions imposed by the method adopted for the pattern generation.

2.3 Methods

2.3.1 Traditional stochastic tessellation methods

Four main classes of stochastic methods for space tessellation have been proposed in the literature to describe materials microstructure. They can be found under the names of Delaunay Triangulation (DT), Voronoi Tessellation (VT), Laguerre Tessellation (LT) and Johnson-Mehl Tessellation (JMT). All those methods comply with the basic requirement of metallographic theory, i.e. that the grains fill the whole space with no gaps (Mahadevan, et al., 2002).

Delaunay tessellation, the most simple, constructs the cells from triangulation of each generator with three closest neighbours (Delaunay, 1934), resulting in tetrahedral domains. Only the triangulation for which the circumsphere of each cell do not contain any generator can be considered as Delaunay tessellation. In this way, for a given set of points the Delaunay tessellation is unique. Some analytical results for the properties of a 3D Poisson-Delaunay tessellation are available and can be found in (Muche, 1996). In particular, the distribution of sizes is determined by the point process used to define the generators: a quasi-Poisson distribution is obtained in the 3D case and the only possible changes to it can be obtained by changing the position of the points. Furthermore, cells are always tetrahedral, this being a large limit for a direct applicability of the method to real cases. Delaunay tessellation is quite rigid in that all geometrical properties for each cell are already decided by the positioning of the generators (Delaunay, 1934).

Dual to the DT is Voronoi tessellation (VT). The VT considers the planes bisecting the segments connecting each generator with all neighbours ((Sibson, 1980), (Aurenhammer, 1991), (Kumar, et al., 1992), (Lucarini, 2008), (Lucarini, 2009), (Thomas, 1996)): the cells are the set of points closest to the chosen centre. In the computing of the distances, the Euclidean norm is employed. The resulting cells are strictly convex polyhedron with a number of faces equal to the number of closest neighbours (Figure (1a)). It should be noted that the convexity condition is

strictly related to the fact that the Euclidean norm is used: the situation can be different if different norms are employed (see e.g. (Gravner, et al., 1997)).Among Voronoi tessellations, the most used is Poisson-Voronoi Tessellation (PVT) where the centres are generated using the Poisson point process. As noted by Lucarini (Lucarini, 2008), the PVT has "*a great relevance at practical level because it corresponds, e.g., to studying crystal aggregates with random nucleation sites and uniform growth rates*".

The LT and LVT (Laguerre Voronoi Tessellation) on the contrary, are not evolutionary: they use a non-Poissonian process to position the generators. In particular, the centres are chosen in such a way that spheres with a known size distribution centred on them do not overlap ((Yang, et al., 2002), (Wu, et al., 2010)). In practice, the LT and LVT increase the degrees of freedom of the VT by placing the interface plane in a position shifted with respect to the midpoint of the segment connecting the neighbouring generators (Figure (1b)). This intersection position, guaranteeing neighbouring spheres not to collide, can be seen as the result of a pseudo growth-rate associated to each centre and expressed under the form of sphere radius ((Fan, et al., 2004), (Wu, et al., 2010), (Lochmann, et al., 2006)).

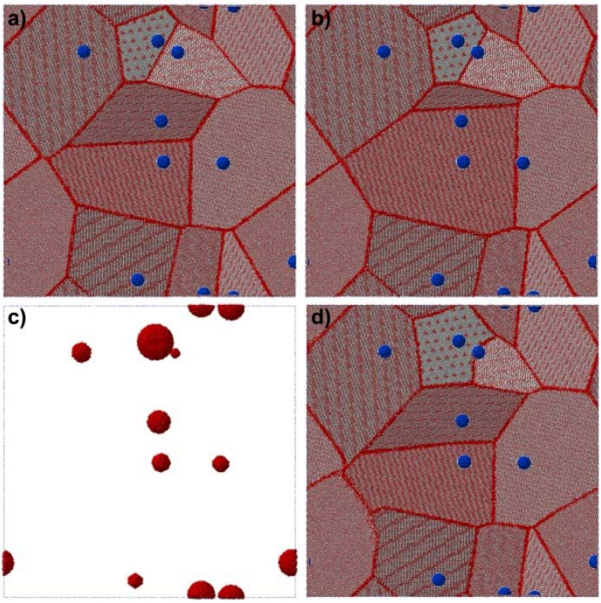

Figure II - 1. Resulting microstructures by using (a) VT, (b) LT, (c, d) JMT. The generator centres are marked by blue dots. The starting nuclei in (c) evolve in the microstructure shown in (d) by a uniform growth at constant rate.

With the idea of a growth rate in mind, the JMT tries to obtain a microstructure by defining a reference cell around each centre and simulating a constant and uniform growth of them. All cells are inflated till they collide and this collision is tracked point by point. Spherical cells are generally used as starting point, resulting in curved cell-cell interfaces. The final geometrical structure is completely unknown ((Farjas, et al., 2008), (Gilbert, 1962), (Pineda, et al., 2004), (Ferenc, et al., 2007)) and concave cells can be possibly obtained. The big advantage of the JMT lays in its physical basis, as it tries to simulate the actual process of nucleation and growth in order to obtain a realistic microstructure (Figures (1c), (1d)).

2.3.2 Modified Voronoi Tessellation (MVT)

Voronoi Tessellation enforces a dependence of the cell shape on the mutual positioning of the generators: this limits and constrains the possible configurations and topological properties that can be obtained when describing the packed arrangements of objects with a given distribution. To better clarify this point and its implications, let's consider the simple case of a cluster of randomly arranged spheres (effectively mimicking an aggregate of equiaxed grains) with a lognormal distribution of diameters (see Figure (2a)). Clearly, the Voronoi Tessellation obtained from the centres of the spheres does not match the actual microstructure (see the dashed lines and the shaded area in Figure (2a)). Voronoi Tessellation is in fact unable to randomly pack a given set of unequal spheres: once a (quasi-)spherical shape of the cells is chosen and a given sphere is selected (grey cell in Figure (2b)), the possible size and position of the neighbouring cells is determined. Given a point, the direction where to place a neighbour determines the orientation of a face of the cell (direction and face are orthogonal), whereas the distance fixes the cell size along that direction. To avoid the unphysical resulting superposition (cf. Figure (2b)), the neighbouring objects should then elongate (Figure (2c)). This is an intrinsic limitation of Voronoi Tessellation that goes beyond the sophisticate evolutionary procedures employed e.g. by Gross & Li (Gross, et al., 2002) and by Suzudo and Kaburaki (Suzudo, et al., 2009) to build a microstructure with a given distribution. The impossibility of VT to pack equiaxed objects is also the main reason why any evolutionary method inevitably creates non-spherical cell shapes (see Figure (2c)).

As a matter of fact, any tessellation based on the classical norm (excluding the JMT) would lead, in a real case, to polyhedral grains approximating the spheres and not to true spheres. The microstructure of Figure (2a) is actually compatible with a Laguerre Tessellation with generators in the centres of the spheres; to obtain a Laguerre Tessellation of a given sphere set, first a Random Close Packing of Spheres (RCPS) must be calculated (Fan, et al., 2004). This computationally-intensive step cannot be avoided and is not easily parallelisable.

To quickly and directly reproduce an arrangement like the one depicted in Figure (2a) starting from randomly positioned centres, we propose a Modified

Voronoi Tessellation (MVT). The main differences between PVT (but also VT in general) and MVT lays in the configuration of the cell-cell interface. In particular, its position along the distance of neighbouring centres (Plane Interface Position, PIP) and its orientation with respect to the plane orthogonal to that vector (Plane Interface Orientation, PIO) are modified. Changing those factors, i.e. going towards a more realistic nucleation/growth process (as in the LT and JMT methods), allows the simulation of realistic microstructures with various statistical distributions of geometrical properties and grain types.

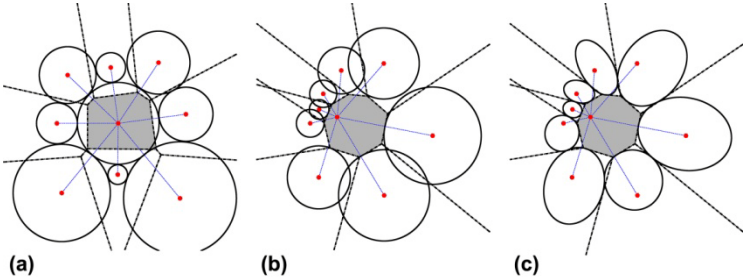

Figure II - 2. (a) Random packing of spheres with a lognormal distribution of diameters. The centres of the spheres form the dashed Voronoi net. (b) Trying to pack spherical objects around a given (quasi-spherical one (gray). The Voronoi points needed to create the gray object must be centres of intersecting spheres. (c) To avoid intersections, the neighbouring objects have to be deformed.

The release of position and orientation of the plane interface is obtained by introducing two additional factors in the geometric procedure of the VT (cf. Figure (3)): a growth factor (GF) displacing each PIP from the mid-point between two generators and a rotation factor (RF) that changes the associated PIO. The growth factor is obtained as the product of a cell growth factor (CGF) isotropic for the cell, plus a face growth factor (FGF) taking into account a directional dependence of the cell expansion (or contraction). The PIP along the segment connecting two nearest centres A and B is obtained by equilibrating the GF of the corresponding grains, as in:

$$\begin{aligned} GF(A) &= CGF(A) \bullet FGF(AB) \\ GF(B) &= CGF(B) \bullet FGF(BA) \\ PIP &= d(AB) \bullet \frac{GF(A)}{GF(A)+GF(B)} \end{aligned} \qquad (1)$$

where d(AB) is the distance between A and B.

To allow for PIOs not permitted by the Voronoi Tessellation, the rotation factors (or better the rotation angles (ψ, θ) along two normal axes centred on the Voronoi PIP) are introduced. Clearly, the VT is obtained from MVT assuming constant GF and null RFs.

The cells in MVT are convex polyhedra, but they are usually not space filling: some void regions are created at the cell junctions, as the relaxation of the Voronoi tessellation constraints does not guarantee the compatibility of the geometry of the cells. These voids can be seen as a closed porosity and can form connected networks so counting them has a limited meaning. The presence of the voids is not a serious limitation for the aim of the present work, i.e. the application of the MVT to build a microstructure. Independently of the porosity, the boundary microstructures obtained by filling the cells with atoms are non-physical and need at least a MD equilibration ((Xu, et al., 2009), (Xu, et al., 2010)). Therefore, as there is no definitive experimental result on the boundary structure (Van Swygenhoven, 2002), several methods can be proposed to take the voids into account or to eliminate them when filling the cells with atoms: some alternatives will be proposed in next section.

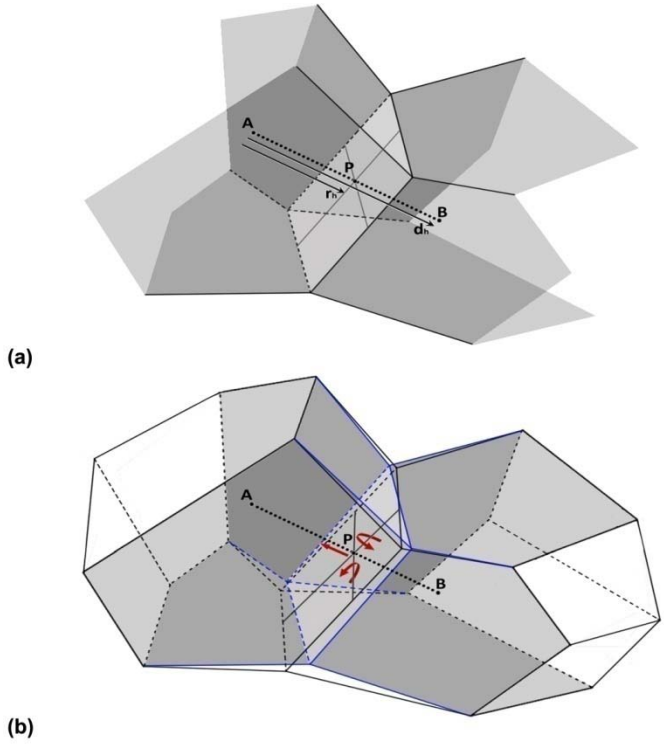

Figure II - 3. Neighbouring grains. (a) Traditional Voronoi Tessellation. Poisson-Voronoi generators A and B and corresponding Voronoi PIP (P). The distance between the generators d(AB) and the distance of the PIP from A (r_A) are also shown. (b) Modified Voronoi Tessellation. The three possible operations introduced by the modified method, i.e. shift and two rotations of the plane interface.

The only limitations to the generality of the resulting cell shape are the number of faces and their flatness. The latter restriction can be removed, for example, by roughening the surface of the cells during the microstructure generation (more precisely, when filling the cells with a given crystallographic structure).Sinusoidal functions (Figure (4a)) or additional protruding shapes (Figure (4b)) can be used to roughen the grain–grain interfaces. However, exotic and, more generally unstable local configurations of the atomic arrangement will be relaxed by the equilibration process.

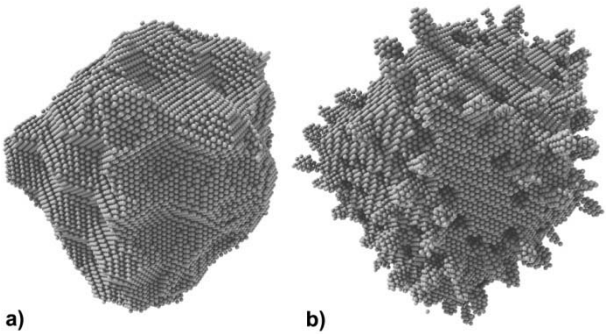

Figure II - 4. Non flat grain-grain interfaces: sinusoidal shape (a), additional stand out shapes on the surface (b).

2.3.2.1 Relationships between traditional tessellations and the MVT

To frame the MVT in the existing literature, an analogy between tessellation methods and a nucleation/growth process can be used as shown in Figure (5). The combinations of growing rate and nucleation time show several behaviours respect which VT, LT and JMT methods are limiting cases of a more general tessellation procedure, whereas the MVT is the most flexible linear approximation. Moreover, in MVT the directional contribute introduce a third additional factor not possible to involve in the JMT method.

More precisely, a classical PVT is compatible with an instantaneous nucleation of the generators and a uniform growth of the cells whereas the JMT assumes nucleation being time-dependent and growth being uniform. It can be readily seen, in fact, that the GF for the VT are, for instance,

$$\begin{aligned} \mathrm{VT} &\Leftrightarrow \begin{cases} CGF(A) = CGF(B) \\ FGF(AB) = FGF(BA) \end{cases} \\ &\Leftrightarrow GF(A) = GF(B) \\ &\Leftrightarrow PIP = d(AB)/2 \end{aligned} \qquad (2)$$

The VT and JMT, however, are essentially different in the construction of the interfaces, planar in the one case and curved in the other. Owing to its construction, a VT with curved interfaces cannot be obtained, whereas a JMT with planar interfaces is a special case of the MVT.

Laguerre tessellation, on the other hand, has a quite complex GF:

$$\mathrm{LT} \Leftrightarrow GF(A), GF(B) \left| \frac{GF(A)}{GF(A)+GF(B)} = 1.0 + g_A^2 - g_B^2 \right. \qquad (3)$$

$$\Leftrightarrow PIP = \frac{d(AB)\left(1.0 + g_A^2 - g_B^2\right)}{2}$$

A suitable combination of nucleation times and growth rates in respect to the nucleation centres distance is in fact necessary as to guarantee the interfaces between neighbouring grains to be planar and shifted and space filling with respect to the VT case.

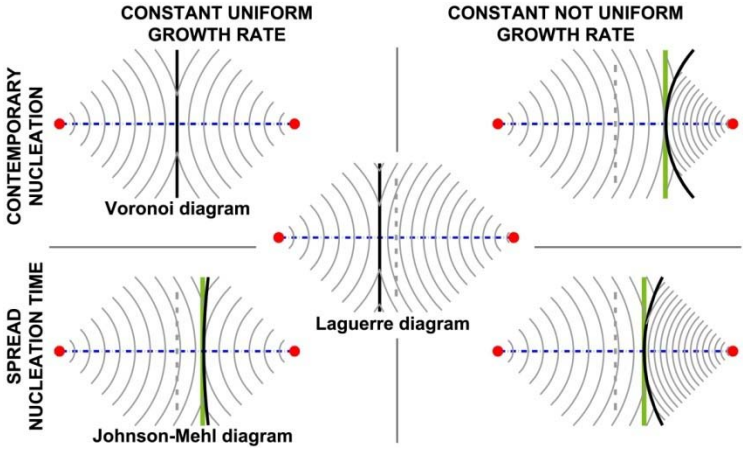

Figure II - 5. Classification of the various tessellation methods with analogy to nucleation and growth with planar or curved interface. The MVT diagram approximations of non-planar interfaces are shown by the green lines.

The analogous of all traditional models assuming a non-uniform growth rate can also be obtained as special case of the MVT. For instance a JMT with planar interfaces and anisotropic grain growth can be easily built. Of course, the issue still remain, in some cases, on space filling. As a final remark, the MVT method is able to approximate every configuration by an interface plane, clearly, in the special cases depicted by the VT or LVT it will be equivalent to them.

2.3.3 Constrained Modified Voronoi Tessellation (CMVT)

The MVT allows the construction of a model with a target cell volume distribution simply by choosing an appropriate distribution of CGFs (Suzudo, et al., 2009). If necessary, some of the topological properties of the cells can be modified by suitably tuning the model parameters (e.g. the Cell Centre Positions (CCPs)). Unfortunately, a deterministic solution is not yet available to build a microstructure with a desired set of target properties: to this purpose, an evolutional method using Reverse Monte-Carlo (RMC) and genetic algorithms is here presented.

The CMVT analyzes a large collection of models made by the MVT method using different sets of generator parameter values and selects the one that best matches the target configuration. The models are produced by an iterative process involving a key model (i.e. the best model in a subgroup analyzed in the previous iteration step) as starting condition. As in CVT, we minimize here an objective function χ^2, given by the sum of the squared distances between target and current M properties (respectively, P^{target} and $P^{refined}$):

$$\chi^2 = \sum_k^M \left[P_k^{target} - P_k^{refined} \right]^2 \quad (4)$$

The optimization algorithm involves the following basic scheme:

1) Build a starting solution (Key Model, (KM)) and compute its χ^2(KM).
2) Create a set of trial solutions by changing a few generator parameters of the KM.
3) Based on the trial solutions, generate a set of trial patterns and their corresponding χ^2(i).
4) Replace the KM with the best model among the current one and the new ones.
5) If the χ^2 is not minimum or is larger than a chosen threshold value, cycle again from step (2).

Several statistical and topological properties, e.g. cell size distribution, cell shape isotropy, misorientation and volume fill density can be simultaneously optimized. Some of them, such as e.g. cell size distribution and cell shape isotropy, show little compatibility (it is difficult to create rounded cells with a given distribution, based on a VT) and therefore a careful convergence strategy is needed to avoid local minima and instability of the optimisation process. The solution envisaged here is to employ a modified objective function:

$$\chi^2 = \chi^2_{spread} + \sum_k^M \left(w_k \left[P_k^{target} - P_k^{refined} \right]^2 \right) \quad (5)$$

where a set of weights (wk) and an extra penalty (χ^2spread) are included to take the relative relevance of each target property into account, and to avoid a large spreading in the values of the improved properties. The weights and penalty are compromise values chosen case by case to guarantee the mutual compatibility of

the target properties. The refined cell structure can be used as is, or employed to generate a polycrystalline cluster as assumed here.

For fast computing, both synchronous and asynchronous multithreading were investigated. In the synchronous case, the Key Model is tested and possibly replaced at the end of each iteration step, requiring all threads to be finished and thus breaking the parallelism. In the asynchronous approach each thread works independently, comparing and possibly replacing the Key Model with its own, without waiting for all other threads to end. The latter approach improves the computing performance by eliminating the dead times, but it is usually less efficient as it requires more iterations (see Figure (19)).

2.4 Results and discussion

2.4.1 Atomic density and voids in MVT-derived microstructures

To visually compare the effects induced by different point growth factors on the resulting microstructure, a pseudo-planar case was simulated. A set of centres was produced using a Poisson process with λ= 1 on a square planar region with periodic boundary conditions. Starting from the same set of 14 points, four different microstructures were generated using different MVT setups (see Figure (6)). In Figure (6a), the classical PV Tessellation is shown: the interfaces are halfway between neighbouring points and space filling is guaranteed. In Figure (6b) a lognormal distribution of CGF described as:

$$f(x) = \frac{1}{x\sigma\sqrt{2\pi}} \exp\left(-\left(\frac{\ln x - \mu}{2\sigma} \right)^2 \right) \qquad (6)$$

with σ = 0.30, μ = 1.00 was chosen. The shape and size of the domains modifies and a fraction of empty volume is generated in the impingement points of three or more grains. The quantity and the extension of the void regions can be changed by using a more complex set of parameters: in Figure (6c) for instance three different FGF (100 for <1 0 0>, 75 for <1 1 1> and 50 for <0 1 1>; directions referred to the orientation of the local crystallographic reference chosen for each cell) are selected, whereas in Figure (6d) a random perturbation of the interface angles (in the +/- 20.0° range) is applied.

The incoherent positioning of the interfaces is the cause for the presence of voids in the MVT: this results in a larger flexibility, as a large spread in atomic density can be obtained by suitably choosing the modelling parameters and by careful filling of the voids. Coherent modifications in the position of the interfaces would have resulted in space filling, but at the expenses of MVT generality.

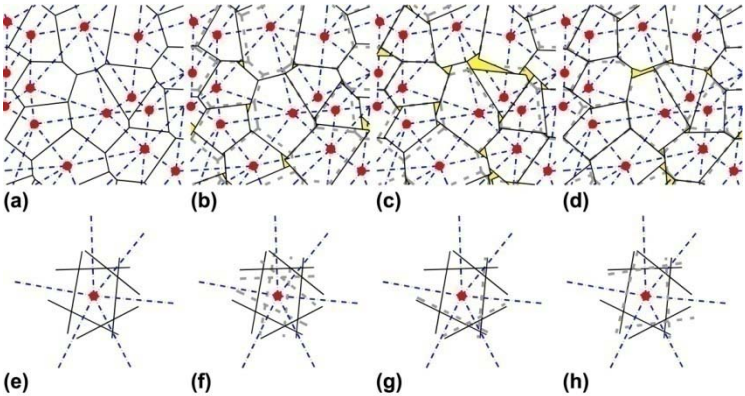

Figure II - 6. Changes in the microstructure caused by a different choice of model parameters. (a) Voronoi construction, (b) MVT with a lognormal distribution of CGF, $\mu = 1$, $\sigma = 0.30$. (c) MVT with different FGF (100 for <1 0 ,0>, 75 for <1 1 1> and 50 for <0 1 1>). (d) MVT with random perturbation of the PIO (limited to +/- 20°). In (e), (f), (g), (h) the detailed construction of a cell with the conditions (a), (b), (c) and (d), respectively. The dashed lines show the modifications occurring to the Voronoi cell in the various cases.

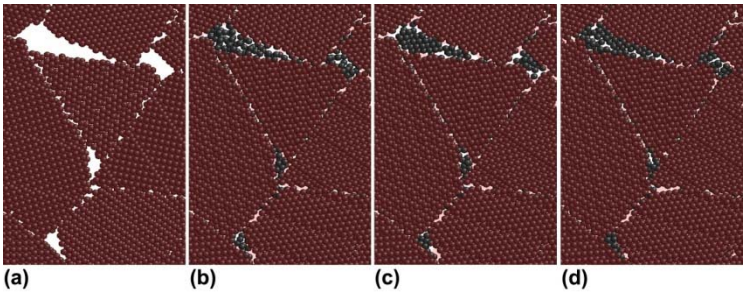

Figure II - 7. Filling of the void resulting from the MVT with (a) empty space (no filling); (b) amorphous phase (c) crystalline phase and (d) extension of the grains. See text for details.

Voids are filled when the atoms are placed inside the pattern of cells. Four alternatives are here proposed (Figure (7)):

1) leaving voids empty (Figure (7a)): this would effectively simulate a packed aggregate of grains as obtained e.g. in a packed powder;
2) filling voids with a glass phase of given density (Figure (7b)). This would allow a system with completely incoherent grain boundaries to be simulated;
3) filling voids with additional grains possessing independent orientation (Figure (7c)). A fully crystalline structure is obtained, but a possibly unphysical large fraction of very small grains is introduced in the system;
4) growing neighbouring grains into the voids (Figure (7d)). Slightly irregular grain shapes are obtained, but maximum density can be reached. The process is

similar to the Johnson-Mehl growing but here a more complex picture of CGF and FGF can be taken into account.

The maximum quantity of atoms that can be placed in the box is not fixed, but depends on factors such as:

- the method used to fill in the cells with the crystallographic structure (for example, a realistic microstructure can be obtained by deleting atoms closer than 85% of the first neighbours distance (Xu, et al., 2009), Figure (8a));
- the way the pattern of cells is built, and the statistical properties of the microstructure (size distribution, grains number and shape type).

The approach used to fill the grain-grain interface regions entails a strong fluctuation of the quantity of atoms in space: the number is larger for overlapping grain boundary structures (Figure (8b)) than for separate domains (Figure (8c)). Furthermore, the total quantity of atoms in the system can be easily handled by randomly placing atoms in the gap region between separate domains, thus reproducing a liquid phase (Figure (8d)).

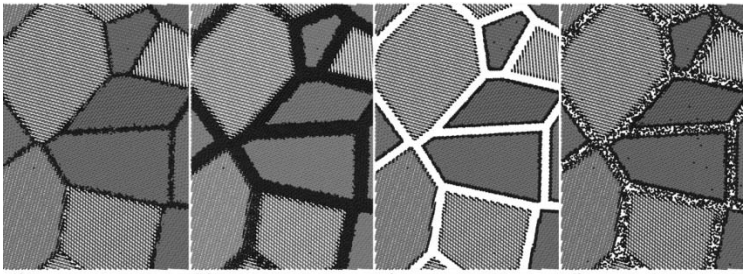

Figure II - 8. Cross-section of a Voronoi microstructure. The cells are filled with *fcc* metal structure, whereas the grain-grain interface is handled by: eliminating atoms closer than 85% of the shortest neighbour distance (a), and unphysical overlapping of the grain structure for a fixed depth (b), removing atoms at the surface of the cells and leaving separate grains (c), removing atoms at the surface of the cells and filling the so-obtained voids with a liquid phase (d).

However, independently of all other parameters, the number of grains (i.e. centres) is the key factor to determine the relative atomic density AD (defined as the ratio between the actual atomic density and the maximum one) for a cluster (cf. Figure (9a)). Due to the presence of voids, the atomic density obtained with the MVT is intrinsically lower than that given by the PVT; the difference disappears when the voids are filled using the 4th model (see list above, cf. Figure (9a)).

Increasing the number of centres N causes a decreases of the atomic density and a corresponding increase in the surface-area-to-volume ratio (SA/V): the two

curves in Figure (9a) can be well reproduced by the two exponentials AD=0.92455+0.05106 exp(N/290.938) and SA/V=0.14626-0.1669 exp(-N/306.434).

Even for a single grain, full atomic density is never obtained in the general case unless box and lattice are suitably chosen (e.g. box scaled with respect to the unit cell and box corners sitting on lattice points).

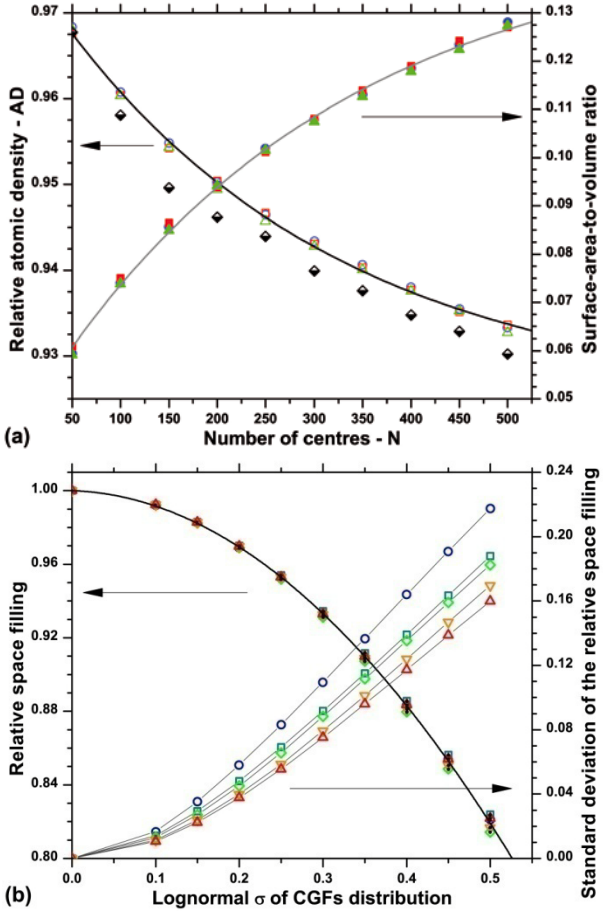

Figure II - 9. (a) Relative atomic density and surface-area-to-volume ratio versus number of centres for four pattern methods: (i) PVT (circle), (ii) CVT with target lognormal distribution σ = 0.15 (square), (iii) MVT with a lognormal distribution of CGF having σ = 0.10 (diamond) and (iv) same as (iii) but with voids filled according to model F4 (triangle). In (b) statistical properties (mean and standard deviation) of the relative space filling in the model versus lognormal σ for the MVT as a function of the number of centres: 1000 (circle), 2000 (square), 3000 (diamond), 4000 (down triangle) and 5000 (up triangle).

In any case, nanomaterials cannot be simulated with full atomic density owing to the presence of a large fraction of lower-density grain boundaries where empty volume accumulates. The situation presented in Figure (9a), however, refers only to the geometrical construction: changes are expected when the geometrical microstructure is evolved using, e.g. Molecular Statics or Molecular Dynamics.

The actual values of the input parameters of MVT have a strong effect on the space filling ability. A decrease in space filling ability is usually observed when increasing the dispersion of growth and rotation factors: however, the trend is not monotonous and it is possible to find combinations of parameters which give a better filling of the space. The relative space filling Sf (fraction of volume occupied by the cells in a unity volume inside the box) is independent of the density of centres in the simulation box and decreases steadily for increasing breadth of the input distribution. As an example, Figure (9b) shows the case of a lognormal distribution of CGF with $\mu = 1$. The curve can be well modelled as $Sf = 1 - 0.01449\,\sigma - 0.069477\,\sigma^2$. When increasing the breadth of the input distribution of CGFs, the distribution of the Sf becomes more symmetrical (the skewness approaches zero) and its standard deviation becomes proportionally larger (see Figure (9b)). It is clear that the higher the σ (i.e. the wider the distribution of sizes), the more difficult is to get a random spatial arrangement of the objects, thus the higher the chances that empty regions (voids) remain (lower space fill). An increase in space filling with respect to Figure (9b) can be obtained by using the CMVT method (Leonardi, et al., 2013).

2.4.2 Statistical properties of the MVT

It is quite interesting to study further the microstructures obtained by MVT when imposing a lognormal distribution of CGF, all other modification parameters being zero (i.e. GF equal to CGF). Figure (10a) shows the average cell volume (V) distributions for the microstructures resulting from the application of the MVT method to the same set of 5000 centres using different lognormal distributions of CGF. The specimens will be identified as MVT x L y where x is the number of centres and y is the σ of the lognormal distribution of CGF ($\mu = 1.0$). Lognormal curve fits are also provided in Figure (10a) as a guide for the eye. For a given distribution of CGF, the result does not modify if the CGF associated to each centre, the μ of the CGF and the box dimensions are changed.

The cell volume is just a possible parameter to characterise the size of irregular objects such as the tessellation cells. The equivalent volume cell radius, total cell surface area, face surface area and number of faces per cell (NF), are also employed to characterise the topology of the resulting objects. It can be observed that the distributions of cell radius and cell surface area obtained with a lognormal distribution of CGF are close to lognormal too. The Cumulative Distribution Functions (CDFs) were compared in the case of some samples made by several number of centres (1000 to 5000) and lognormal variances of the CGFs ($\sigma = 0.10$ to 0.50).

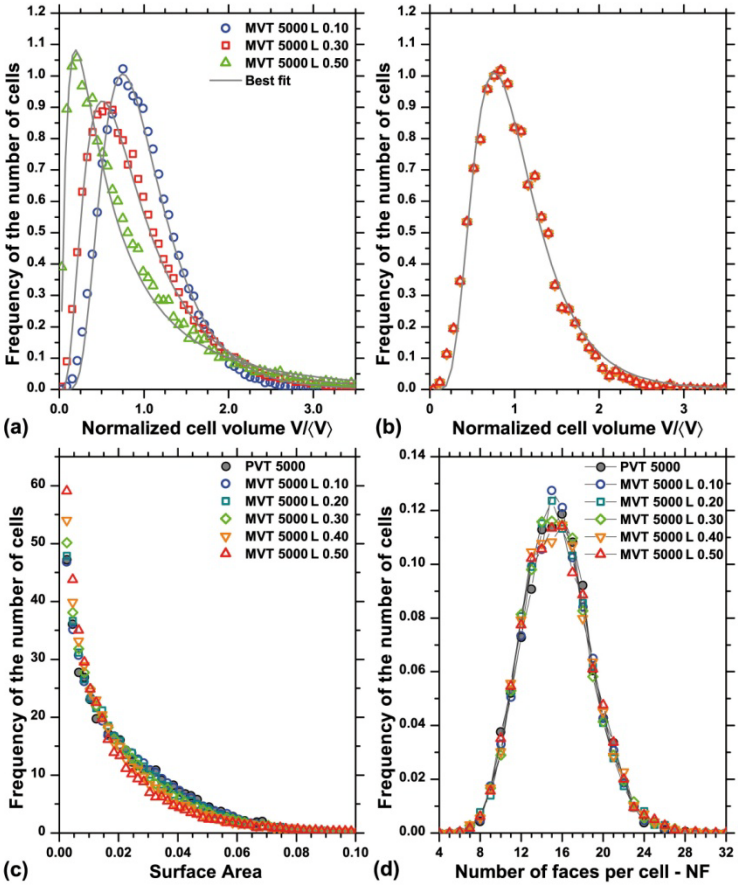

Figure II - 10. Cell volume distribution for a few MVT 5000 samples obtained (a) with different CGF distributions and (b) with fixed distribution (σ = 0.1) and increasing box size expressed as number of unit cells along the edge: 100 (circle), 150 (square), 200 (diamond), 250 (up triangle), 300 (down triangle). In (c) and (d), respectively, the distributions of total cell surface area and number of faces per cell. The curve proposed by Tanemura (Tanemura, 2003) is shown in (d) as continuous line.

The largest difference between the observed and the best fitted lognormal CDFs are below the 5% critical Kolmogorov-Smirnov limit. Moreover, the smaller the number of centres and the variance of the lognormal distribution of the CGFs, the higher the level of significance. For instance, significance is larger than 10% in the case of MVT 1000 samples. The mean of the resulting distribution depends on box size and number of points, i.e. on the average volume per point, whereas the variance depends only on the input parameters and is unaffected by the box size. This is clearly shown in Figure (10b) presenting the analysis of some MVT 5000

samples made with the same lognormal distribution of CGFs (μ = 1.0 and σ = 0.10) but increasing box size. The independence on box size of the statistical properties allows a coherent scaling of the results obtained on a sample to any other one.

As expected (Figure (10c)) the surface area of the faces and their frequency are almost inversely related. Quite different is the behaviour of NF shown in Figure (10d): all simulated microstructures show exactly the same distribution whose mean (15.5352) is very close to the average facedness of the PVT ($2+48\pi 2/35 \approx 15.53547$ ((Meijering, 1953), (Hilhorst, 2009), (Tanemura, 2003))) and whose shape is compatible with the slightly skewed generalised Gamma distribution proposed by Tanemura (Tanemura, 2003). The agreement comes from the fact that the mutual arrangement, of the centres and thus the average number of near neighbours, is not changed by the MVT. The number of faces of the polyhedral grains, on the other hand, is strictly connected to the geometric construction involved and it is usually close to the number of faces of the dual Voronoi cell construction (10d).

The number of faces is sufficient to characterise several topological properties of the cell. In fact, by using Euler's formula for convex polyhedron we can relate NF with the number of vertices (NV) and the number of edges (NE) of a cell as NV – NE + NF = 2. The NV can in turn be computed using the equation: NV = 2NF – 4. The changes in NF and in the average volume of the corresponding cell are usually linearly correlated through Lewis' law (Lewis, 1928): <V>NF = αL (NF - NF0). In the present case, however, a parabolic trend is evident (cf. Figure (11a)): a parabolic violation of Lewis' law has been already pointed out in both simulated and measured dispersed polycrystalline microstructures ((Xu, et al., 2009), (Yang, et al., 2002), (Aboav, et al., 1969), (Beck, 1954), (Rivier, 1985)).

The nonlinear trend seems associated to the process employed to lay the centres in the box. In fact, limiting the minimum distance between centres eliminates the nonlinearity: Figure (11b), for instance, shows the modification occurring to Figure (11a) when rising to 20Å the minimum distance between generators. Small deviations from the trends occur at the edges of the NF curve owing to the limited statistics (number of grains) associated to those points. The parameters of the curves slightly change with the increase in the standard deviation of the cell volume distributions, but invariably intercept the axis at NF = 3 (degenerate case). This suggests that the deviation in the slopes of the MVT models is due to the presence of voids, decreasing the cell volume especially of the larger cells. The influence of the voids decreases with the cell size and the axis intercept agree with the impossibility to define a closed polyhedron with less than 4 faces.

A final check for the properties of the cell ensemble is provided by the ratio between the average number of faces in all neighbouring cells to a cell of NF faces (m(NF)) and the number of faces per cell. The relationship is well described by the Aboav-Weaire law (Chiu, 1995):

$$NF \cdot m(NF) = \left[\langle NF \rangle - \alpha\right] + \left[\langle NF \rangle \alpha + \mu^2\right] \qquad (7)$$

where α and μ are fitting parameters. Mathematically, it expresses the tendency for any random tessellation to have small grains surrounded by large ones and *vice versa*.

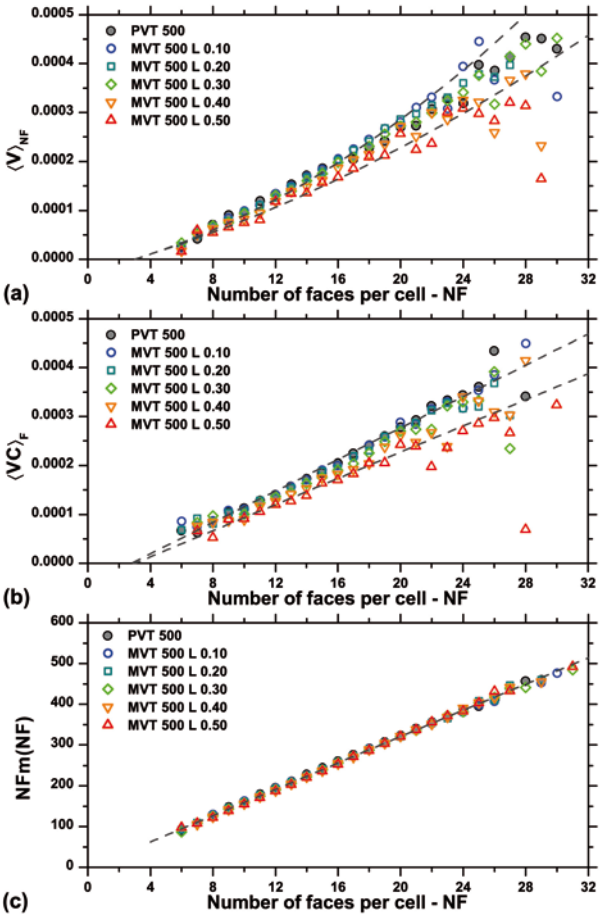

Figure II - 11. (a) and (b) Lewis plots for the MVT 5000 samples of Figure 6a. The plot in (b) was obtained by limiting the minimum distance between centres to 20Å. In (c) the Aboav-Weaire plot is shown for the MVT 5000 samples of Figure 6a. Fits are proposed for the limiting cases MVT5000 L 0.1 and MVT 5000 L 0.5.

Plots for the cases analysed here are shown in Figure (11c): the MVT and PVT methods show exactly the same slope and the same deviation from the best linear fit. Different distributions, resulting from the PVT and MVT with lognormal CGF, lead to analogous trends: this is consistent with the fact that both algorithms

start with a similar random arrangement of points and that the MVT does not heavily modify the number of faces of Voronoi cells (cf. Figure (10)). A small downward curvature in Figure (11c) seems to be present, confirming the observation of Hilhorst (Hilhorst, 2009), thus strengthening the idea that the Aboav-Weaire law might be just a good local approximation for the correct trend. In the range shown, the modified curve proposed in (Hilhorst, 2009) i.e. NF m(NF) = 8 NF+23.15 NF5/6-15.96 NF2/3 does not appreciably depart from Eq. (7).

2.4.3 Relationship between input parameters and resulting microstructure

A systematic relationship exists between the input CGF distribution and the resulting cell size distribution. It should be stressed that different choices can lead to completely different resulting distributions. For the sake of brevity, just the lognormal case is analysed in detail. Without losing in generality, a collection of samples was simulated with increasing number of centres and different lognormal CGF distributions with lognormal mean μ = 1. A cubic box with PBCs and a side of 100 unit cells was employed. The same naming convention for the samples proposed before will be used here.

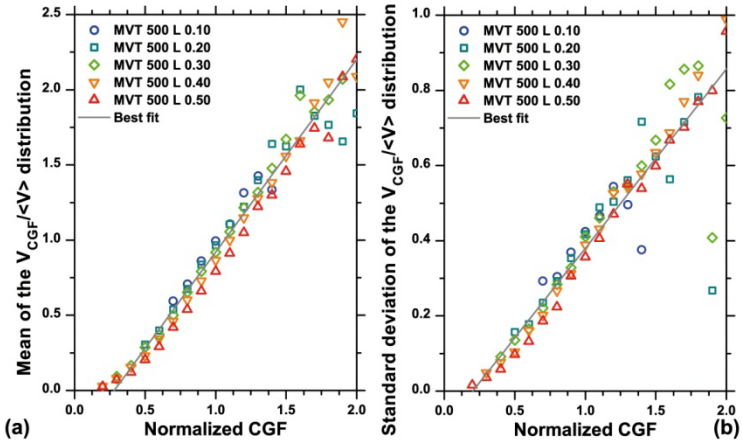

Figure II - 12. Mean (a) and standard deviation (b) of the normalised cell volume distributions as a function of the normalised CGF (where V is the volume of the cells having a reference CGF). Data relative to the MVT5000 L 0.10 (circle), MVT5000 L 0.20 (square), MVT5000 L 0.3 (diamond), MVT5000 L 0.4 (down triangle), and MVT5000 L 0.50 (up triangle).

As an example, Figure (12) shows the relationship between the input CGF and the corresponding mean and standard deviation of the (lognormal) grain volume distribution. The direct dependence between CGF and mean cell volume (or size in

general) expresses the fact that if the centres would be isolated, their size at a given time would be proportional to their growth rate. The standard deviation for each CGF value, on the other hand, is related to the magnitude of the difference between isolated growth and actual growth (constrained by the interference with the other centres). Therefore, the growth rate represents somehow the probability of interference between neighbouring centres. In particular, centres with a small growth rate (small CGF) interfere with the neighbouring centres after a longer time than those with a higher growth rate (high CGF).

The PVT method is the simplest case of constant-rate growth. Therefore, the cell size distribution of a PVT reflects exactly the distribution of the half distances of the neighbouring centres. In a sample created by the PVT method, the cell radius computed from the cell volume and from the mean plane interfaces distance show exactly the same distribution and almost the same values. A change in the size distribution is strictly connected to any change of the arrangement of the centres. For instance, the CVT method drives the centres towards a configuration where the distribution of plane interface distances is comparable with the target cell volume distribution. As previously noted, this leads to non spherical cells; in particular, cells with the largest standard deviation are more anisotropic (Xu, et al., 2009). Removing the constraints imposed by the Voronoi construction, allows moving the centres independently of the cell shape: a full control over anisotropy (and therefore roundness of the cells) is thus possible.

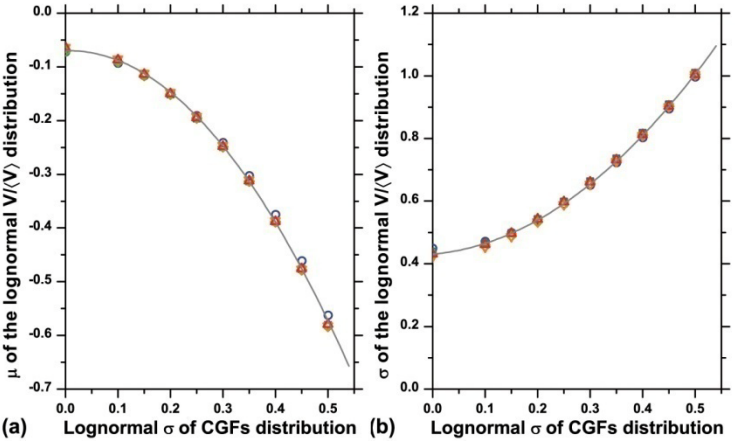

Figure II - 13. Relationship between the σ of the input lognormal distribution of CGF and the parameters μ and σ ((a) and (b), respectively) of the resulting best fitted lognormal output distribution of V/<V> for specimens of increasing number of centres (1000: up triangle, 2000: down triangle, 3000: diamond, 4000: square, 5000: circle).

Figure (13) shows a clear parabolic relation between σ of the CGF (σ_{in}) and both μ and σ of the corresponding cell volume distribution. Independent of the number of centres, the two parabolas can be parameterised as $\mu = -0.0674 - 2.0149\ \sigma$ in (13a) and $\sigma = 0.4454 + 2.2455\ \sigma$ in (13b). The result is compatible with the PVT where $\sigma = 0.445$ is obtained when fitting the resulting distribution with a lognormal (Meijering, 1953). The data spread around the best fit in Figure (13) can be related to the statistics of the corresponding distributions. The picture does not change if the size of the box, the number of centres and the μ of the lognormal CGF distribution are changed. The behaviour shows significant deviations if the homogeneous Poisson point process with parameter $\lambda=1$ is not used. A characteristic relation is observed when imposing a minimum distance between neighbouring cell generator centres: the higher the threshold value of the neighbour distance, the smaller the variances of the log-normal best fit cell volume distributions (see Figure (14)). The possibility of having the same cell statistical and topological properties, by varying only one or simultaneously more than one generator parameters, support the unconstrained nature of MVT. Actually, compared with homogeneous Poisson, slightly lower significance values are found for the agreement between cell volume and log-normal distributions.

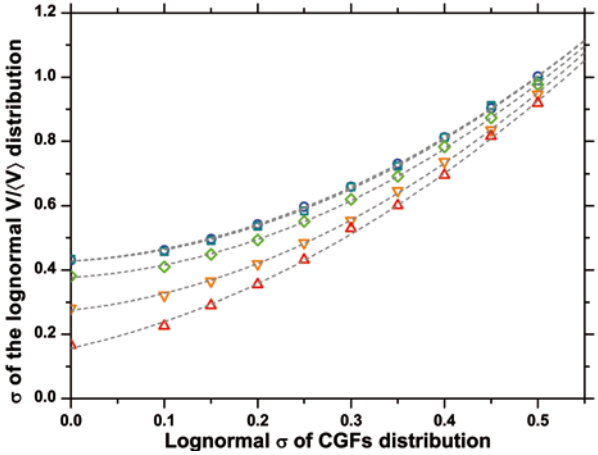

Figure II - 14. Relation between σ of the input lognormal distribution of CGF and the resulting σ of the best fit lognormal output distribution of V/<V> for specimens of increasing shortest distance between generator centres. Shortest distances are expressed as fraction of the minimum neighbour distance for the density equivalent *fcc* structure: 1/3 (up triangle), 1/4 (down triangle), 1/6 (diamond), 1/12 (square), and Poisson point process (circle).

Systematic effects related to the simulation parameters can be detected also for other topological properties such as the average cell surface density (CSD), i.e. the ratio between the cumulative cell surface and the box volume. Figure (15) shows

the trend of the CSD versus the σ of the input distribution of CGF. The average cell surface density decreases with increasing distribution width. The trend is similar independently of the number of centres, but the actual values steadily increase with the increasing quantity of generators. An increase of the standard deviations of CGF distribution causes a general decrease of the global surface of the cells: in fact, the larger the spread of the cell sizes, the smaller the volumetric contribution of smaller cells for a constant box volume. It is well know that in a box of constant volume a system of smaller spheres would have a larger surface than a system of large ones. For a given distribution, moreover, an increase in the number of centres causes a decrease of the mean cell size, and therefore a corresponding increase in the cell surface density, as experimentally observed.

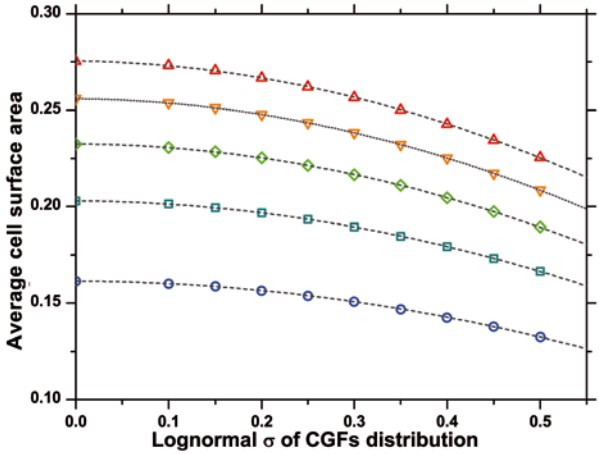

Figure II - 15. Dependence of the cell surface density versus the σ of the input CGF for an increasing number of centres (1000: up triangle, 2000: down triangle, 3000: diamond, 4000: square, 5000: circle).

2.4.4 Reliability of MVT statistics by the evolutionary CMVT

All evolutionary processes were started here with a cubic box having Periodical Boundary Conditions (PBCs). A thousand centres were placed in the box by a homogeneous Poisson point process with λ=1 and were assigned suitable CGF values. The initial CGFs were chosen according to a Log-normal Probability Density Function (PDF) with unit mean:

$$PDF_{Log-normal} = \frac{1}{x\sqrt{2\pi\sigma^2}} \exp\left[-\left(\frac{\ln x - \mu}{2\sigma}\right)^2\right] \qquad (8)$$

At each iteration step, four new models are generated starting from the KM and varying the free generation parameters of 90% of the cells (randomly chosen). In

a similar way as in (Leonardi, et al., 2012(d)), samples are here named CMVT x L y I z, where x is the number of centres, y is the starting σ_{input} of the Log-normal PDF of the input CGFs, and z is the number of iterations. It has been already shown in (Leonardi, et al., 2012(d)) that null FGFs and PIOs lead to a normalised cell volume PDF being close to the expected Log-normal. In that case, the standard deviation of the Log-normal frequency distributions of the target normalised cell volume ($\sigma_{expected}$) and of the input CGF (σ_{input}) are quadratically dependent and $\sigma_{expected}=0.4454+2.2455\ \sigma^2_{input}$ (Leonardi, et al., 2012(d)).

Three cases were simulated here: CMVT 1000 L 0.10, 0.20 and 0.30. Significant sample populations were defined for each one of those cases, repeating 100 times the evolutionary process with different random initial configurations. The starting average levels of significance over the population with respect to the expected PDF (σ = 0.4679, 0.5352 and 0.6475) were, respectively, 23.01%, 35.34% and 38.74%. The levels of significance computed via Kolmogorov-Smirnov (KS) hypothesis test were improved by the constrained algorithm. The initial configurations were evolved by varying each starting CGF by a random factor $0.10 < \delta < +0.10$, without changing any other generator parameter.

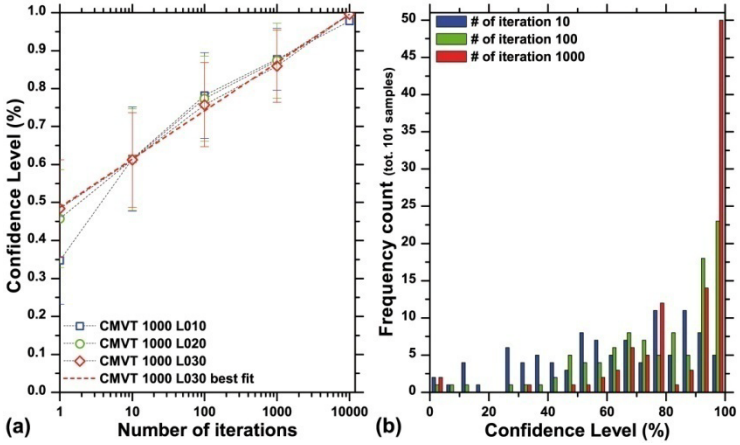

Figure II - 16. (a) mean and standard deviation of the levels of significance of the CMVT 1000 L 0.10, 0.20 and 0.30 I 1000 populations during the evolutionary processes; the results for a single run of CMVT 1000 L 0.10, 0.20 and 0.30 I 10000 is also provided to confirm the observed trend (in this case the standard deviations are not available). (b) distributions of significance levels of CMVT 1000 L 0.30 after 10, 100, and 1000 iteration steps.

After an initial transitory phase (ca. 10 iterations), the evolutionary processes of the three cases show the same logarithmic trend and the same absolute values of the level of significance computed by the KS test (see Figure (16)). Moreover, the larger the number of iterations, the larger the average levels of significance and the

smaller the average variances (Figure (16a)). When increasing the number of iterations, the distribution of the levels of significance tends to become more left-skewed (Figure (16b)). Hence, a target level of significance can generally be reached by varying just the CGF values, without changing the generators (as in the CVT method).

The normalized cell volume distributions of the evolved samples (averaged over each of the three populations) are in good agreement with the target PDFs, as computed by the KS hypothesis test (cf. Figure (17a)). The evolutionary process has significantly changed the absolute values of the CGFs, raised from 1.0 to 2.8 in 1000 iterations. Nevertheless, the normalized CGF distributions of the evolved samples are very close to the initial ones. The average frequencies over each of the three populations show Log-normal PDFs (see Figure (17b)). The standard deviations of the Log-normal best fit of the CGF distributions of CMVT 1000 L 0.10, 0.20 and 0.30 I 1000 are close to the input values (respectively: 0.1363, 0.2165 and 0.3104).

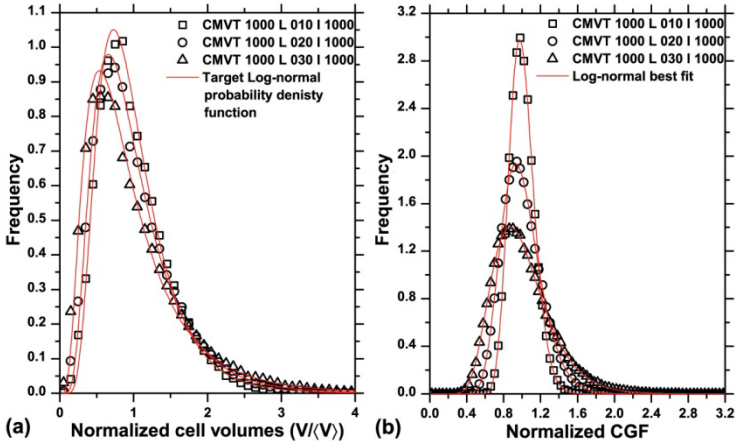

Figure II - 17. Normalized cell volume (a) and CGF (b) frequency distributions of CMVT 1000 L 0.10, 0.20 and 0.30 I 1000.

2.4.5 Multiple target properties optimization with CMVT

Differently from the CVT, the CMVT method is able to yield several independent pattern configurations with similar statistical and topological properties by combining more than one generator parameter (e.g. CGFs and CCPs). This greater flexibility allows the CMVT method to optimize at the same time more than one statistical and topological property of the model.

To prove this, a model of 1000 cells (CMVT 1000 L 0.10 I 100000) was evolved in a cubic box having Periodical Boundary Conditions (PBCs) by the CMVT method varying the CGFs and CCPs with three given target properties: Log-normal

cell size distribution, maximum volume fill density and cell shape isotropy. Since a generic collection of spheres cannot tessellate the space, volume fill density and spherical shape turn out to be incoherent. The equiaxed shape has been thus chosen as target property and the standard deviation of the distance between cell faces and generator centres was minimised.

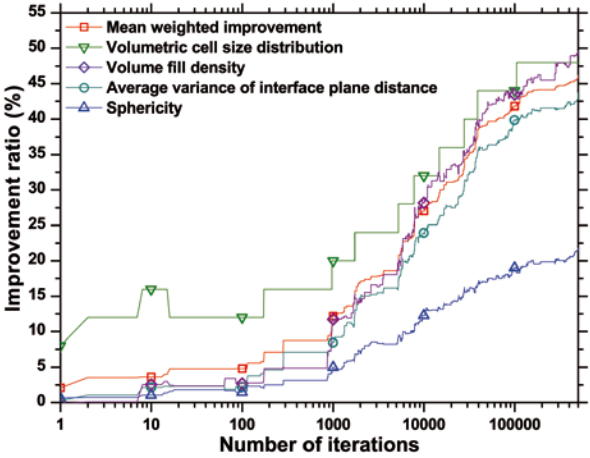

Figure II - 18. Improvement history of the properties for the evolutional process about CMVT 1000 L 0.10 (a limit number of 100000 iterations was imposed).

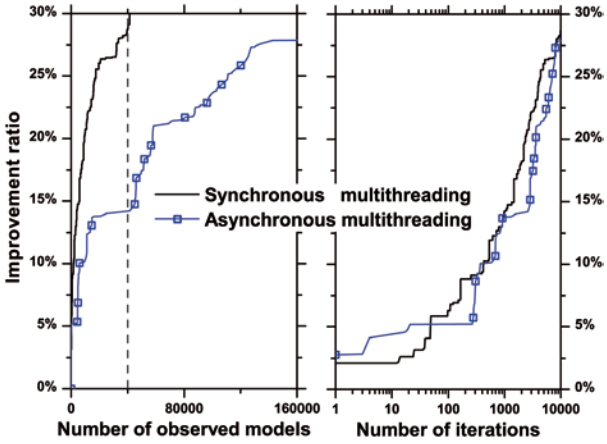

Figure II - 19. Improvement ratio for synchronous (dark continuum line) and asynchronous (blue dotted line) multithreading approaches vs. number of observed models (left) and number of iterations (right). Four threads were employed in both cases: in the synchronous case each thread explores one model per iteration, whereas in the asynchronous one, four models per thread are investigated each iteration.

The convergence efficiency was improved by assigning a higher weight to the equiaxial character (double with respect to the others). In this case, the new models created at each iteration step are obtained by randomly changing both the generator centres (two in the box and two near the corresponding positions of the KM) and the CGF (by a random factor $0.10 < \delta < +0.10$). Figure (18) shows the percent improvement of each property P, defined as $(P_{current}-P_{initial})/(P_{target}-P_{initial})\%$, during the evolutional process: the improvement is logarithmic, with convergence speed increasing stepwise with the iteration number. Synchronous and asynchronous multithreading approaches were employed. Despite the larger collection of models investigated by the second approach, the improvement ratio seems strictly dependent on the number of iterations (see Figure (19)).

Once the pattern with the required properties is obtained, the atomistic microstructure can be built. In each cell, the generator and the centres of mass are more or less coincident. A planar section (Figure (20a)) shows features that cannot be obtained by other tessellation methods: for instance, the grain-grain interfaces are not placed in the middle between the generator centres as in the case of the VT method, and the topological properties of the cells are not directly correlated with the cell size distribution. This can be also appreciated in Figure (20b), presenting the distributions of the variances of the distances between grain centres and grain interface planes of both the CMVT 1000 L 0.10 I 100000 and two other models having the same cell size distribution, but made by CVT and MVT.

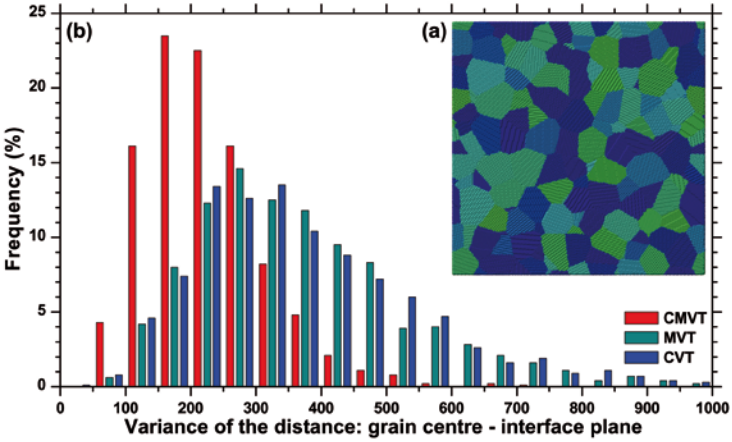

Figure II - 20. (a) Plane section of CMVT 1000 L 0.10 I 100000 polycrystalline microstructure. (b) Frequency distribution of the variance of the distances between grain centres and grain interface planes.

The CVT and MVT samples show very close frequency distributions ($\mu \approx 375$, $\sigma \approx 180$), whereas the evolved CMVT has clearly smaller mean and standard

deviation ($\mu \approx 225$, $\sigma \approx 92$). Still, an ideal value for the sphericity (Ψ) defined on the basis of the surface and volume of the cells (S and V, respectively) as:

$$\Psi = \frac{\pi\left[6V/\pi\right]^{\frac{2}{3}}}{S} \tag{9}$$

cannot be achieved by any VT or MVT pattern, being each cell a convex polyhedron.

Since a generic collection of spheres cannot tessellate the space, volume fill density and sphericity turn out to be incoherent. Notwithstanding, a significant improvement of the sphericity is still found in the CMVT simulation (see Figure (21)).

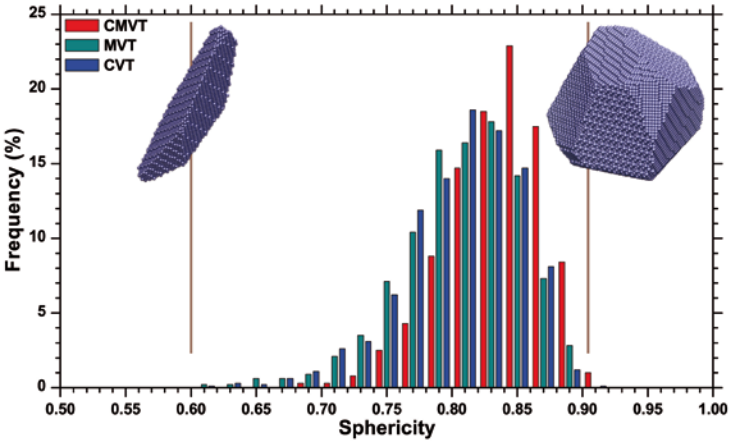

Figure II - 21. Frequency distribution of the sphericity for CMVT 1000 L 0.10 I 100000. The two extreme shapes for the given cluster are shown as a reference.

2.4.6 MVT computing performance

We have shown that the MVT can directly provide a microstructure with a given size distribution variance and with a shape close to lognormal. Unlike the VT, however, computing time for the MVT is not linearly related to the number of centres, but it depends on the actual properties of the input distribution. This is a consequence of simultaneously dealing with all centres and corresponding growth factors to compute the shape of the resulting cell, while keeping full record of the voids.

The increase in computing time is clear in Figure (22) that shows the total time required to build a model of 1000 grains in a box with PBCs when increasing the σ of the CGF distribution. Calculations were performed on an Intel Core 2 processor (4 physical cores) at 2.8 GHz in multithread mode (4 computing threads). Clearly the MVT needs a longer time to deal with the cases where a centre is surrounded by other centres having a wide variety of CGF: a broader CGF distribution increases the probability of this condition to be met. Of course, as previously pointed out, the

broader the distribution, the larger the fraction of void space (cf. Figure (9b)), thus the longer time and the larger memory for recording information about intersection of interface planes.

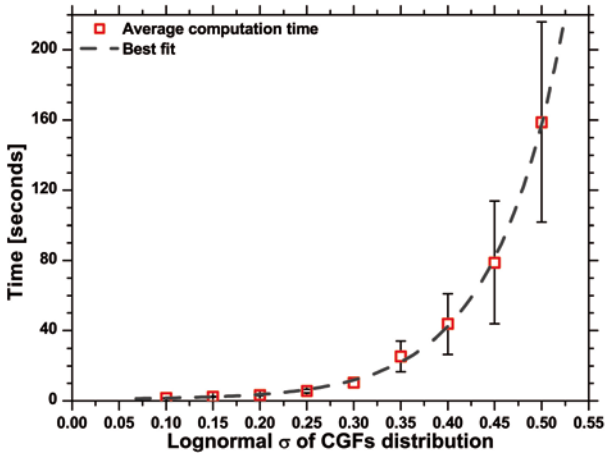

Figure II - 22. Time required by the MVT method to compute the microstructure (i.e. to identify the faces of all cells) for the MVT 1000 set of specimens.

When compared with the few available literature data on advanced tessellation methods (cf. (Suzudo, et al., 2009)), the actual values in Figure (22) suggest that MVT can be orders of magnitude faster than the available algorithms to obtain a target distribution of cells. In fact, to obtain a target lognormal distribution of 1000 grains on a computer with 80 cores, Suzudo and Kaburaki (Suzudo, et al., 2009) needed at least 1150 seconds of CPU time (the actual value might be higher depending on the target precision). Scaled to a 4-cores machine such as the one employed here, this would correspond to more than 23000s, clearly out of range with respect to Figure (22). No data are available for the CVT proposed in (Xu, et al., 2009): however, the authors state that at least 500 steps are needed to reach a good level of convergence, versus a single step required by MVT.

2.5 Conclusion

A Modified Voronoi Tessellation (MVT) has been proposed to simulate a realistic microstructure. To obtain that, MVT starts with a random distribution of centres in a box (with or without periodic boundary conditions) and builds the corresponding cells by relaxing the Voronoi constraints on the cell-cell interfaces, i.e. by shifting and rotating them with respect to the midpoint between neighbouring centres. The resulting microstructure (pattern) is characterised by the presence of voids that can be easily eliminated when filling the cells with atoms. A one-to-one relationship between the input model parameters and the characteristics of the output distribution has been found, allowing a target distribution to be directly obtained. For instance a lognormal distribution of grain sizes can be directly simulated with a 5% level of significance. The statistical correlation between the Log-normal distribution of the Cell Growth Factors (CGFs) and the Log-normal cell sizes distribution of a pattern made by the MVT method was confirmed and extended by the Constrained MVT.

The Constrained Modified Voronoi Tessellation method (CMVT) is also proposed to generate polycrystalline microstructures characterized by more than one target statistical and topological property. Space fill density, size distribution and isotropic cell shape are optimized by varying the generator parameters (Cell Centre Positions and Cell Growth Factors): a logarithmic improvement is obtained through an evolutional approach. Thus, realistic microstructures can be obtained beyond the limits imposed by the traditional tessellation techniques.

Computing time increases with the target distribution width, but it is highly competitive to literature alternatives providing similar results.

Chapter III

Analysis of Atomistic Simulation Data

Part of this chapter has been published in:

Alberto Leonardi, Kenneth Roy Beyerline, Tao Xu, Mo Li, Matteo Leoni, Paolo Scardi

"Microstrain in nanocrystalline samples from atomistic simulation",
Zeitschrift für Kristallographie Proceeding, I (2011) 37-42.

Alberto Leonardi, Matteo Leoni, Mo Li, Paolo Scardi

"Strain in atomistic models of nanocrystalline clusters",
Journal of Nanoscience and Nanotechnology, (2012) accepted.

3.1 Abstract

Atomistic modelling was employed to investigate the effect of microstrain on X-ray diffraction patterns in nano-crystal microstructures. Stress and a strain defined on atomic scale from atom positions were computed to represent the local deformation associated with the microstructure (e.g. grain boundaries).

Strain, as an easy and clearly defined concept in continuum mechanics, has no direct counterpart in atomistic models. Existing methods, relying on the concept of atomic coordination number, do not provide a complete description of isotropic and anisotropic strains across metallic nano-crystalline microstructures. To overcome those limitations a new method is proposed: the Voronoi Cell deformation (VCD) fully accounts for the local geometry and provides a description of the strain field independent of the atomic coordination.

Our emphasis is put on the separate contributions from dynamic and static atomic displacements to the corresponding powder diffraction patterns. As a typical case of study, a nano-polycrystalline microstructure of 50 Cu grains (ca 1.5 million atoms) was considered.

3.2 Introduction

Atomistic simulation is recognised as a reliable tool to investigate the structure and properties of nano-scale materials as it can provide atomic-level picture along with the macroscopic collective behaviour comparable to experimental results. This is particularly valuable in the field of nano-structured materials where the microstructures can be created using space filling models ((Gross, et al., 2002), (Suzudo, et al., 2009)) and then simulated by Molecular Dynamics (MD).

Atomistic modelling is increasingly employed to study properties and behaviour of materials under different conditions (Derlet, et al., 2005). Although results do not always match those of traditional experiments, this approach is informative and can most frequently capture the main features of the physical phenomena of interest ((Jang, et al., 2006), (Cao, 2009), (Van Swygenhoven, et al., 2000), (Li, et al., 2006)). The limited extension of the time scale commonly accessible to MD simulations penalizes some applications, like those concerning plasticity, but is perfectly adequate to represent thermal and elastic properties.

A major task is extracting models of behaviour compatible both with the macroscopic observation and with the MD scale. Most of the relevant literature in the field employs methods utilizing stress, pressure or level of coordination ((Samaras, et al., 2003), (Zimmerman, et al., 2004), (Derlet, et al., 2005)) while strain is seldom used (Stukowski, et al., 2009). For certain theoretical analysis, this is sufficient since direct extraction of strain from the stress is not easy. However, the methods based on stress or pressures are not of general applicability to a given sample as they rely on the knowledge of atomic velocity or interatomic potential. Strain, however, is not properly defined at the atomic level because the traditional definition, based on continuum mechanics, does not apply to discrete systems on the atomic level. The complexity is even larger if atomic vibrations are to be considered as well.

Among the available methods, Neighbours Analysis (NA) studies the local geometrical arrangement of neighbours to detect structural features at the atomic level ((Ackland, et al., 2006), (Honeycutt, et al., 1987)). NA is a powerful tool to identify defects and phases in large systems, but is intrinsically unable to provide strain values. Therefore, NA is complemented by methods to calculate local pressure and stress ((Samaras, et al., 2003), (Derlet, et al., 2003), (Derlet, et al., 2006)), as those properties are directly related to the energy of each atom, with no need to define or calculate strains.

Here we will show that a direct calculation of the local strain is possible, based on the knowledge of the atomic positions acquired in our atomistic calculations. More recently, methods have been proposed to compute the local atomic strain by comparing the arrangement of neighbours with respect to a perfect reference structure ((Stukowski, et al., 2009), (Lewis, 1928)). A major drawback is the impossibility to deal with strongly deformed structures, where atoms may not be fully

coordinated. To overcome this limitation we propose the Voronoi Cell Deformation (VCD) method. Based on Voronoi Tessellation, the VCD avoids the somehow arbitrary concept of cut-off radius, required by existing methods ((Stukowski, et al., 2009), (Lewis, 1928)). Moreover, as it makes no reference to the atomic coordination, the VCD can be used across heavily defected regions as well as in the core of nano-structured domains.

Furthermore, from the dynamics, or time evolution of the atoms trajectories, we can compute the mean square displacements which contribute directly to the line broadening in the powder diffraction patterns. As a result, we are able to compare, on a continuum scale, the characteristics of the calculated strain distribution and the microstrain obtained from a traditional X-ray diffraction (XRD) Line Profile Analysis (LPA).The line profile broadening in an XRD pattern is affected by the distribution of strains at the atomic level (microstrain) inside a material. Microstrain can be analyzed by traditional and modern line profile analysis methods: a correct evaluation in nano-crystalline materials is however difficult due to the peculiar microstructure (e.g. large fraction of grain boundaries). An independent approach is therefore needed to directly link the information on the atomic scale with a simulated diffraction pattern. So a judicious validation can be made regarding the pros and cons of these line profile analysis methods.

3.3 Methods

3.3.1 Molecular Dynamics simulation

A nano-polycrystalline copper microstructure was created by randomly placing 50 centres in a box of 260.28 Å side length, using a homogeneous Poisson point process with parameter λ=1 ((Kumar, et al., 1992), (Lucarini, 2008), (Lucarini, 2009)). Cells were identified in the box using Voronoi Tessellation and considering Periodical Boundary Conditions. This microstructure was then evolved by an inverse Monte Carlo method (Constrained Voronoi Tessellation (Xu, et al., 2009)) to obtain a lognormal grain-size distribution of rounded grains (σ ~0.35). Each cell was filled with a randomly oriented (Morawiec, 1995) ideal *fcc* structure (Cu unit cell parameter, a_0 = 3.615 Å); atoms closer than 85% of the minimum distance in the *fcc* structure (a_0/sqrt(2)) were clipped as suggested in (Xu, et al., 2010).

The starting crystalline microstructure was then equilibrated at 100K via the LAMMPS code (Plimpton, 1995) using the Embedded Atom Method (EAM) (Daw, et al., 1983) and the Cu potential of Foiles and Baskes (Foiles, et al., 1986).The temperature, pressure, volume and total energy of the microstructure are shown along the equilibration process in Figure (1). While, temperature and pressure slightly fluctuate around mean values, the volume and total energy quickly decay to a steady state.

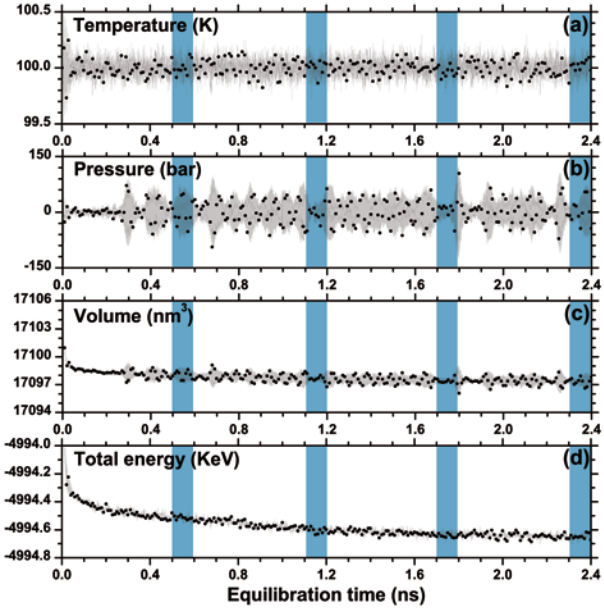

Figure III - 1. Fluctuation of temperature, pressure, volume and total energy of the cluster during the equilibration process. The vertical blue bars identify the time sequences of frames analysed.

Four independent analyses were done respectively at 0.5, 1.1, 1.7 and 2.3 ns since the beginning of the simulation (blue bar in Figure (1)). At each time, a set of atomic positions snapshots (Frames) was sampled with a time interval of 1 ps. This large interval was chosen to remove any correlation in the sampled atomic positions. To cancel out the dynamic effects, a mean atomic position was computed for each atom in the system by averaging the coordinates in a hundred of frames (other approaches are possible ((Stukowski, et al., 2009), (Hasnaoui, et al., 2002))). A fifth set of thousand sequential snapshots was also averaged at 2.4 ns equilibration time (Hasnaoui, et al., 2002), observing deviations between the two average approaches. Hard to obtain in a real experiment, these mean positions (Averaged Frame (AF)) bear information just on the static distortion field; whereas the single frames (Single Frame (SF)) couple the dynamic too.

Results comparable to those discussed here are also shown in (Leonardi, et al., 2012(c)), regarding a nano-polycrystalline aluminium microstructure of 200 grains equilibrated at 100K by Al potential (Jacobsen, et al., 1987).

3.3.2 Global mean square displacement (global MSD)

From the averaged positions the atomic mean square displacements averaged over the samples (global MSD) were obtained (see Figure (2)).

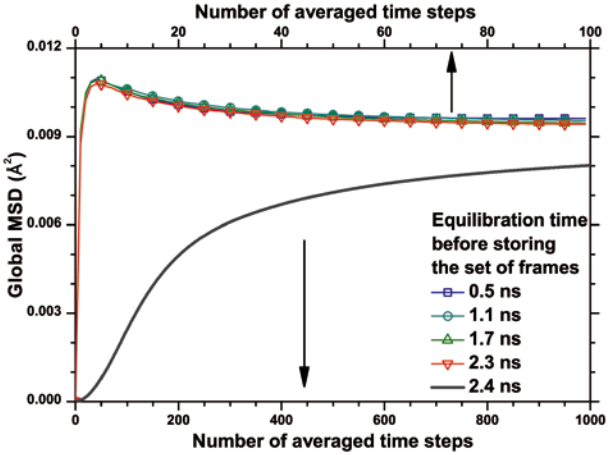

Figure III - 2. Global average of mean square displacements (global MSD) over an increasing number of frames for five sets of atomic position snapshots (sampled with a time interval of 1 ps (dot line), sequential (line)).

By taking the average over an increasing time, one can see clearly different profiles of the MSDs in different parts in the nano-crystalline samples. For example, as shown in Figure (3), the grain boundaries have higher MSD than the inside of the grains, characterizing the presence of a strain field in the system in a steady state (Frøseth, et al., 2005).

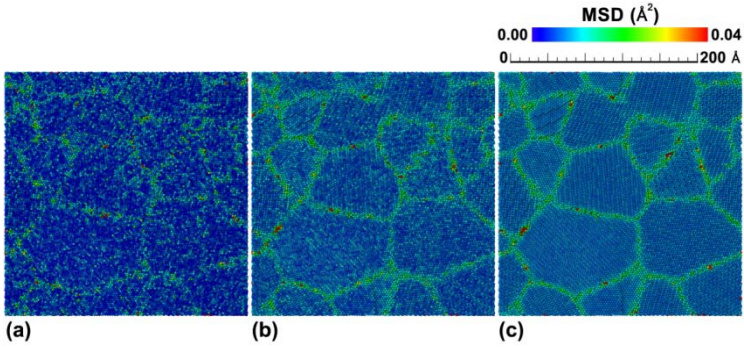

Figure III - 3. Mean square displacements over an increasing number of frames resulting from the time average during the equilibration process (3, 12, 100 frames, respectively).

3.3.3 Local coordination and surface shape

Structural defects in atomistic nano-polycrystalline models can be identified taking into account changes in the local atomic arrangement (Figure (4)). Ackland analysis consists in a graph of ideal structures showing positions surrounded by *fcc*, *bcc* or *hcp* crystal system, as obtained by recognising the number and the relationship of the neighbour positions (Ackland, et al., 2006). Moreover, the mean features of the local distortion field can be guessed from the fluctuation of the level of coordination (Figure (4b)) defined as "-n" if n first neighbours are missing, and "+n" if up to the n-th neighbours are fully coordinated.

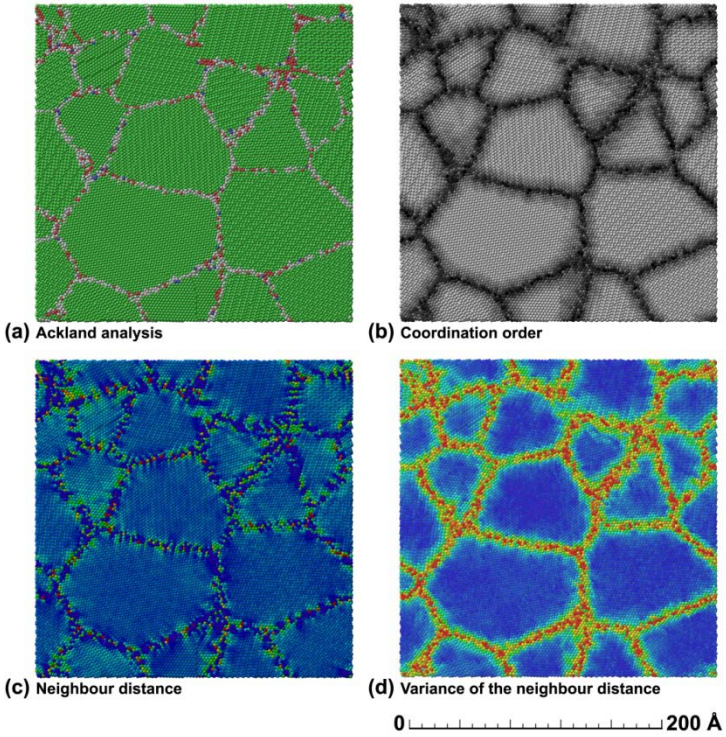

Figure III - 4. Deformation field in the cross-section of the numerical model estimated by: (a) Ackland analysis (*fcc*, *hcp* and *bcc* respectively green, rose, violet), (b) local coordination order (colour scale from black to white, from at least 4 missing neighbours to 4thorder fully coordinated neighbours), (c) average neighbour distance (from 2.434 to 2.635 Å) and (d) the corresponding variance (from 0.000 to 0.110 Å^2).

The deformation field in the AF equilibrated Cu nano-polycrystalline microstructure was qualitatively pointed out by the level of coordination in Figure

(4b), whereas the core of the defects were emphasized by the switch in crystal symmetry from *fcc* to *hcp*, *bcc* or any other different lattice (4a). A preliminary estimation of the local strain magnitude was provided by the mean neighbour distance (4c), which implicitly accounts for local atomic volume. Actually, if atoms are forced to be closer or farther from the equilibrium point, thermodynamic fluctuation will be forced to be, respectively, smaller or larger. Hence, a fine estimation of compressive or tensile hydrostatic stress can be given by the variance of atom neighbour distance over time. Unfortunately, the available analysis methods rely on an arbitrary cut-off radius to choose the neighbours.

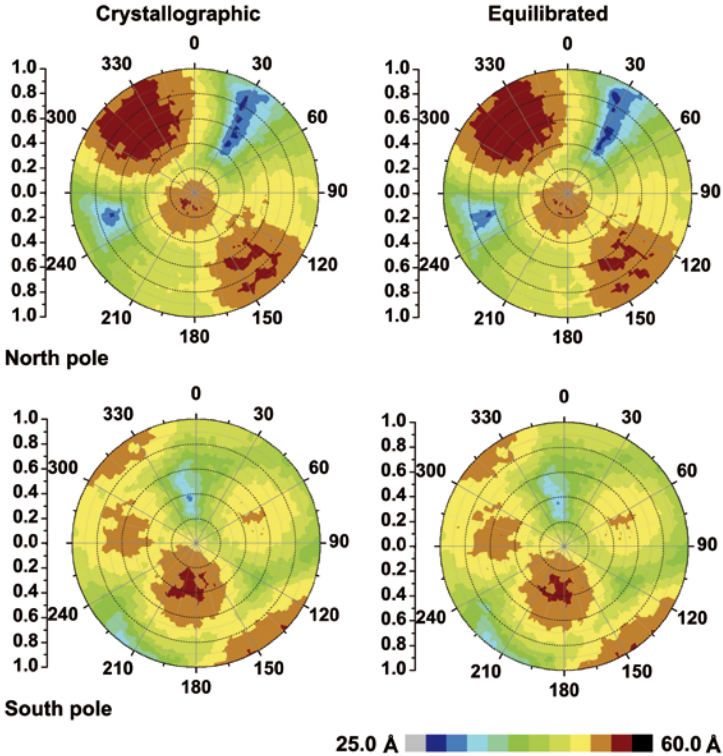

Figure III - 5. Polar projection of the surface distance from the centre of a randomly chosen grain of the Cu nano-polycrystalline microstructure (north (top) and south (bottom) poles), for the Crystallographic and the AF equilibrated models (left and right, respectively).

On the surface or at the grain-grain interface, the arrangement of atoms of the starting crystalline microstructure is adjusted by the equilibration procedure. The shape of each crystal domain is also remodelled, to reach a lower level of total energy for the system. The shape changes can single out general features of the

deformation field acting on the microstructure over a wide set of environmental conditions (e.g. varying temperature and pressure). Negligible differences are observed between the surface polar projections of a randomly chosen grain from the starting (Crystallographic) and from the equilibrated AF microstructure. Hence, in the studied system grain boundary structure is suggested as the only source of distortion of the local atomic structure.

3.3.4 Strain at the atomic level

In solid mechanics, the local deformation is expressed by a normalized gradient tensor under the continuum approximation. This assumption is not valid in MD simulations, as the atomistic nature of matter is intrinsically discrete. Furthermore, without any additional information, dynamic effects are seen as strain.

A reference configuration is needed to define the local strain. If the whole un-deformed microstructure is known, the local strain matrix can be directly computed from the minimization of the squared difference between the analyzed and the ideally undeformed structures (Li, et al., 2005). When the ideal reference is unknown or have no physical meaning (e.g. close to the interface boundary zones in a polycrystalline system) a local crystallographic structure can be adopted.

Two methods have been recently introduced to compute the strain matrix by comparing the arrangement of the neighbours with respect to the ideal local configuration. Both start by finding the neighbours and assigning them a specific order. Then, the method of Stukowski et al. involves a linear least-square fitting of a strain matrix to transform the ideal structure into the observed (deformed) one (Stukowski, et al., 2009). As an alternative, the Crystallographic Cell Deformation method (CCD) (Leonardi, et al., 2011) estimates the significant geometric deformation of the local structure by identifying the principal crystallographic axes and lengths. Hence, the displacements of the deformed cell walls with respect to the ideal *fcc* structure were used to build the local strain tensor according to solid mechanics definitions (Spencer, 1980), computing the direct and cross deformation coefficients. Finally, the principal strains and directions were computed by diagonalizing the local strain tensor.

Those methods are characterised by three principal features:

i. neighbours are identified by considering an arbitrary cut-off radius;
ii. deformation is computed by exploiting some topological properties of the local structure (e.g. symmetry);
iii. deformation at the atomic level is linked to the arrangement of the whole set of near neighbours and so a fully coordinated structure is needed (this condition is easily met in the core of the grains, but is not verified at the grain boundaries).

Those assumptions, unfortunately, limit the applicability of the corresponding methods and in particular do not allow the evaluation of strain in the most deformed regions: for example, the crystal structure at the grain boundary is completely distorted so that it is impossible to univocally identify a local *fcc* lattice and calculate the local strain (Derlet, et al., 2003).

3.3.4.1 The Voronoi Cell Deformation method (VCD)

The Voronoi Tessellation (VT) method is a tool for investigating the arrangement of the neighbours (Mott, et al., 1992).

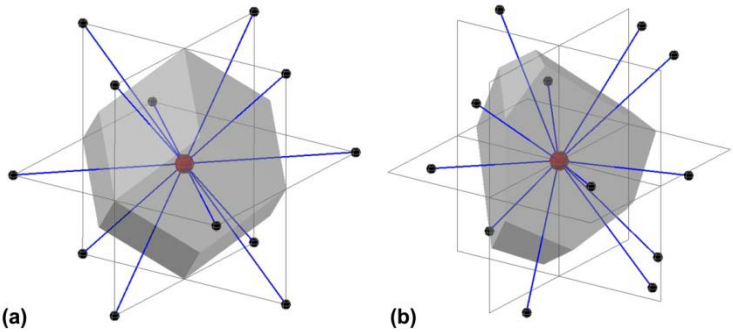

Figure III - 6. Voronoi tessellations for a perfect (a) and for a distorted (b) *fcc* structure.

As shown in Fig. (6), each atom is the generator of a Voronoi Cell (VC) dual to the neighbours' arrangement. The geometric properties of the VC can be therefore analysed in place of the unit crystal structure. As a matter of fact, the strain at the atomic level affects the VC geometry, and thus the moments of mass. If the density of mass is assumed uniform in space, the moments of mass can be replaced by the moments of volume (see Appendix III.A).

The strains at the atomic level along the principal directions are easily estimated by the ratio of the principal inertia of the deformed and reference structures. Linking the inertia values of the VCs to the equivalent parallelepiped solids, the three stretch ratios ($0 < \lambda < \infty$) can be fully defined. From them, the strain can be computed as:

$$\varepsilon = \frac{1}{k}(\lambda^k - 1) \tag{1}$$

where k = 1 or k = 2 allow, respectively, the engineering and Lagrange strain to be obtained. In the end, the strain matrix can be written in terms of the principal strain associated to the principal inertia.

The space-filling nature of the VT guarantees the congruence of the resulting strain values. The isotropic strain at the atomic level can be measured directly from the first moment of mass or it can be computed by the product of the stretch ratios.

In both cases the macro-scale deformation is consistent with the local deformation. Therefore, a discrepancy is detected between measured and real crystal deformation, which is due to the assumption of the equivalent inertia of a rectangular box involved.

A variant of the VCD can be introduced to better take the geometric positions of the neighbours into account: the VT is again employed to identify the neighbours according to the procedure proposed by O'Keeffe (O'Keeffe, 1979). The strain at the atomic level is then computed from the fluctuation of the moments of mass (see Appendix III.B). Differently from the above discussed procedure, the atomistic nature is fully exploited: the mass is therefore considered as concentrated at each atom position (Voronoi moment of mass Cell Deformation method (VmmCD)). Without losing in generality, each atomic position is assigned a unitary mass: in agreement with the geometric nature of the deformation, each Voronoi neighbour contributes to the local structure with a magnitude related to the size of the linked VC face. The point masses need thus being weighted by the relative VC-side surface area (weighted VmmCD method).

3.3.4.2 The evolutional Voronoi Cell Deformation method (eVCD)

The VCD method solves the strain matrix by assuming a link between inertia values of the VCs and of the equivalent parallelepipeds. This is true only in some crystal structure, e.g. the simple cubic. An evolutional algorithm has to be used to avoid any link to a specific crystallographic VC shape.

The principal directions, the inertia and the true isotropic deformation at the atomic level were computed on a given cluster by using the VCD method. Starting from applied deformations (λ_i, λ_j and λ_k), the agreement of the deformed reference structure with the configuration detected in the model is evaluated by a likelihood function χ^2:

$$\chi^2 = \sum_{i=1}^{3} \left(I_i^{model} - I_i^{real} \right)^2 \qquad (2)$$

which is equal to the sum of the squared difference between the inertia of the real and of the refined structure (model). The deformations that provide the best matching between data and model are selected as principal strains at the atomic level.

The efficiency of the procedure can be optimized by suitable algorithms. For instance, the true isotropic deformation, computed by the VCD method, is exploited to decrease the number of degrees of freedom of the problem. In fact, one of the stretch ratios can be computed from the isotropic strain as:

$$\lambda_{vol} = \lambda_i \lambda_j \lambda_k \quad \Leftrightarrow \quad \lambda_i = \frac{\lambda_{vol}}{\lambda_j \lambda_k} \qquad i \neq j \neq k \qquad (3)$$

Although computationally time consuming, the eVCD can be used with highly distorted structures or with atoms that are not fully coordinated, giving values of the principal strains comparable to the real ones.

3.3.5 Isotropic and Anisotropic strains

The deformation field in the atomistic models was characterized by the most significant isotropic and anisotropic tensor components. The local structure, surrounding each atomic position, was defined. Then, the principal strain tensor (ε_I, ε_{II} and ε_{III}) and thus the isotropic (volumetric) and anisotropic (deviatoric) components were computed by the following equations ((Godeke, et al., 2002), (Narasimhan, 1993), (Fung, et al., 2001), (Ting, 1996)):

$$\varepsilon_{iso} = \varepsilon_I + \varepsilon_{II} + \varepsilon_{III} + \varepsilon_I\varepsilon_{II} + \varepsilon_I\varepsilon_{III} + \varepsilon_{II}\varepsilon_{III} + \varepsilon_I\varepsilon_{II}\varepsilon_{III} \quad (4)$$

$$\varepsilon_{aniso} = \frac{2}{3}\sqrt{\left(\varepsilon_I - \varepsilon_{II}\right)^2 + \left(\varepsilon_I - \varepsilon_{III}\right)^2 + \left(\varepsilon_{II} - \varepsilon_{III}\right)^2} \quad (5)$$

The distributions of those two scalars were checked in the case of an elementary deformation field. A square parallelepiped cell was filled with a periodic *fcc* crystal structure; then, every atomic position was displaced according to the local strain components (Figure (7)).

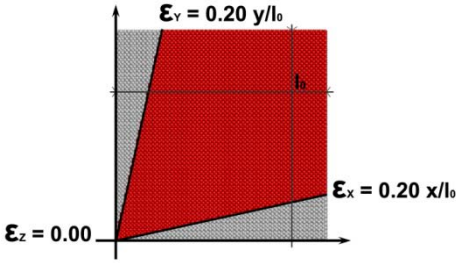

Figure III - 7. Strain field diagrams in the square parallelepiped cell model.

Periodical Boundaries Conditions (PBCs) were applied, achieving fully coordinated structures at each atomic position. That assumption allowed the CCD method to estimate the strain at the atomic level everywhere in the model. At the same time, the local detectable structures were geometrically affine to the reference crystal structure. The real and estimated local isotropic and anisotropic strain fields obtained with different computing methods are shown in Figure (8).

The absolute values of the isotropic strain computed by all methods are close to the expected (true) ones. Only the weighted VmmCD method slightly changes the pattern of the strain field in a non-linear way. Conversely, the values of the anisotropic strain have a strong dependence on the computing method. Again, the

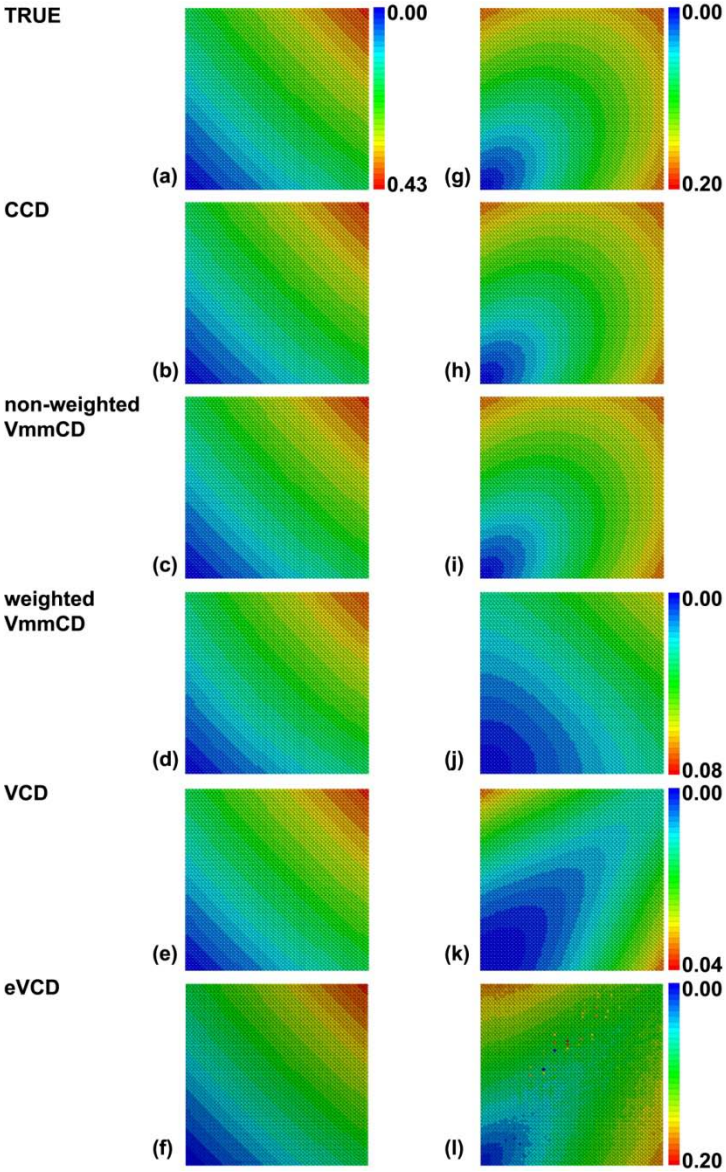

Figure III - 8. Strain field computed by the applied deformation (a, g) and estimated by several methods: CCD (b, h), non-weighted VmmCD (c, i), weighted VmmCD (d, j), VCD (e, k), eVCD (f, l). The isotropic (a, b, c, d, e, f) and anisotropic (g, h, i, j, k, l) strain at the atomic level in the model are showed as the most significant deformation properties.

CCD and the non-weighted VmmCD methods gave results close to the true strain. The VCD and the weighted VmmCD methods are close, but the patterns are stretched and the absolute values are significantly different from the real ones. Moreover, if the local structure would be highly distorted or not fully coordinated, the CCD method would be unable to work. Also a non-weighted VmmCD would be affected by an incomplete coordination.

The weighted VmmCD, the VCD and the eVCD methods can always be used, either in the core of the defects or through the grain boundaries in a polycrystalline microstructure. The mismatch of the anisotropic strain computed by those methods is due to the underlying assumptions and to their capability to assess the distortion of the crystallographic symmetries (Figure (9)). The assumption of the equivalent inertia of the parallelepiped solid in place of the real VC, which is employed in VCD method, could be replaced by more sophisticated functions. Further improvements are needed to fully solve the deformation at the atomic level through the VCD method.

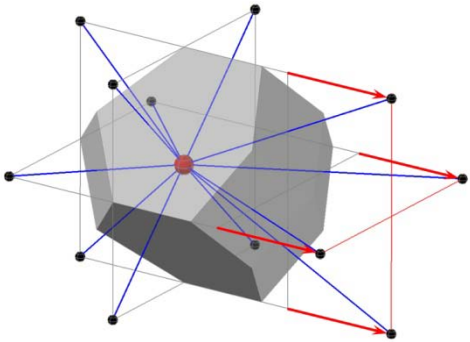

Figure III - 9. Voronoi tessellations of a deformed *fcc* structure made by displacing uniformly the positions of a wall side.

3.3.6 Potential energy and Stress at the atomic level

Atomistic simulations provide useful and reliable data about energetic properties, being based on potential functions and physical models of the material. As an example, the local potential energy can be directly computed from the atomic positions. In doing this, a specific character of the geometric interaction between pairs of atoms is chosen depending on the model employed.

The direct interaction of two isolated atoms can be described by the Lennard-Jones (LJ) potential model:

$$U_{ij} = \sum_{i \neq j} 4\varepsilon \left[\left(\frac{\sigma}{r^{ij}} \right)^{12} - \left(\frac{\sigma}{r^{ij}} \right)^{6} \right] = \varepsilon \left[\left(\frac{r_m}{r^{ij}} \right)^{12} - 2 \left(\frac{r_m}{r^{ij}} \right)^{6} \right] \qquad (6)$$

where r^{ij} is the distance between pair of atoms, ε is the depth of the potential well, σ is the finite distance at which the potential crosses the zero abscissa, and r_m is the distance at which the potential reaches its minimum.

Acting as a non-linear spring between neighbour positions, LJ works well in the case of liquid and gases. For bulk metals, a reliable alternative is given by the Embedded Atom Model, coupling the pair interaction potential with a term taking the bulk environment into account (Daw, et al., 1983):

$$U_{ij} = F_\alpha\left(\sum_{j\neq i}\rho_\beta(r^{ij})\right)+\frac{1}{2}\sum_{j\neq i}\phi_\beta(r^{ij}) \quad (7)$$

where ϕ is a pair potential function, ρ is the contribution to the electron charge density, and F is an embedding function.

The stress at the atomic level can be directly estimated from the sum of kinetic and positional contributes, decomposing the Virial stress (Egami, et al., 1980):

$$\sigma_{\alpha\beta}(i) = \frac{1}{\omega_i}\left[m_i v_\alpha^i v_\beta^i + \sum_{i<j}^{N}\left(-\frac{1}{r_{ij}}\frac{\partial U}{\partial r_{ij}}\right)r_\alpha^{ij} r_\beta^{ij}\right] \quad (8)$$

where α and β identify the Cartesian components, and v the atomic velocity.

Actually, the positional part is computed by deriving the pair potential function, thus involving the nature of the atoms interaction used. Principal stress components (σ_I, σ_{II}, σ_{III}) and directions can be computed by diagonalizing the stress tensor matrix. Moreover, the hydrostatic stress component is computed as a third of the sum of the principal stresses (Guo, et al., 2012).

3.4 Results and discussion

3.4.1 Strain at the atomic level in a nano-polycrystalline microstructure from MD

The strain at the atomic level was computed in the numerical model of the Cu nano-polycrystalline microstructure, using the discussed analysis methods and an *fcc* crystal structure as a reference (unit cell size of 3.6150Å).

The deformation field was characterized in the microstructure equilibrated using the Embedded Atom Method potential, respectively after 0.5, 1.1, 1.7, 2.3 and 2.4 ns from the start of the simulation (Figure (10)). No significant differences were detected in the strain fields computed at the different equilibration times (Van Swygenhoven, 2002), as well as for the two approaches employed in computing the averaged position (from a set of sampled frames, or from a set of sequential frames). Figure (11) shows the strain at the atomic level on a planar cross-section of the model at an equilibration time of 2.3 nano seconds.

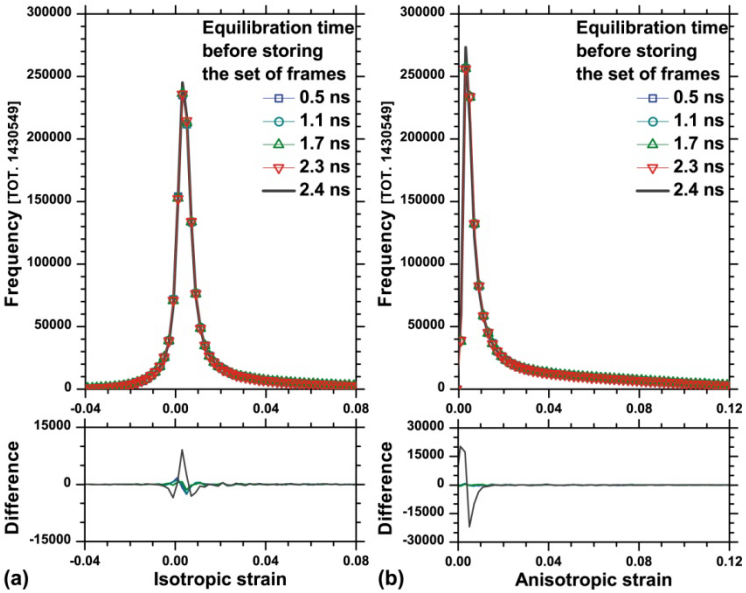

Figure III - 10. Frequency distributions of the local isotropic (a) and anisotropic (b) strain in the numerical model computed by the VCD method applied to the averaged atomic positions stored at equilibration time of 0.5 (square), 1.1 (circle), 1.7 (up triangle), 2.3 (down triangle), and 2.4 ns (line).Difference plots (below) are referred to the 2.3 ns equilibration time.

It is quite evident that the CCD, as well as any method based on the crystallographic geometry, can provide results only in regions where atoms are fully coordinated and the local structure is not too much distorted. This condition is commonly not satisfied at the grain boundary, and in the core of the defects. For this reason, we do not calculate the atomic strain right inside the grain boundaries. Hence, only a fraction of the strain field can be investigated by CCD and gaps in the strain maps appear (white regions in Figure (11)). The VCD method, being unaffected by the local crystallography, is able to provide a strain value associated to each and all atomic positions. A quick increase in local strain close to the boundaries is highlighted in Figure (12). The boundary region embodies several local distorted configurations, allowing the structures of neighbour grains to be joined together; here we can see the nearly regular alternating sequence of compressive and tensile strains.

After the system reached equilibrium (2.3 ns equilibration time), the local atomic strain was calculated with respect to the ideal *fcc* structure both for a Single Frame (SF) and for the system Averaged over 100 Frames (AF). A semi-stochastic fluctuation of the strain in the model, caused by the diffuse dynamic contribution, is clearly evident in the SF and tend to be cancelled out in the AF over a long time period (see Figure (11a), (11b), (13a), and (13b)).

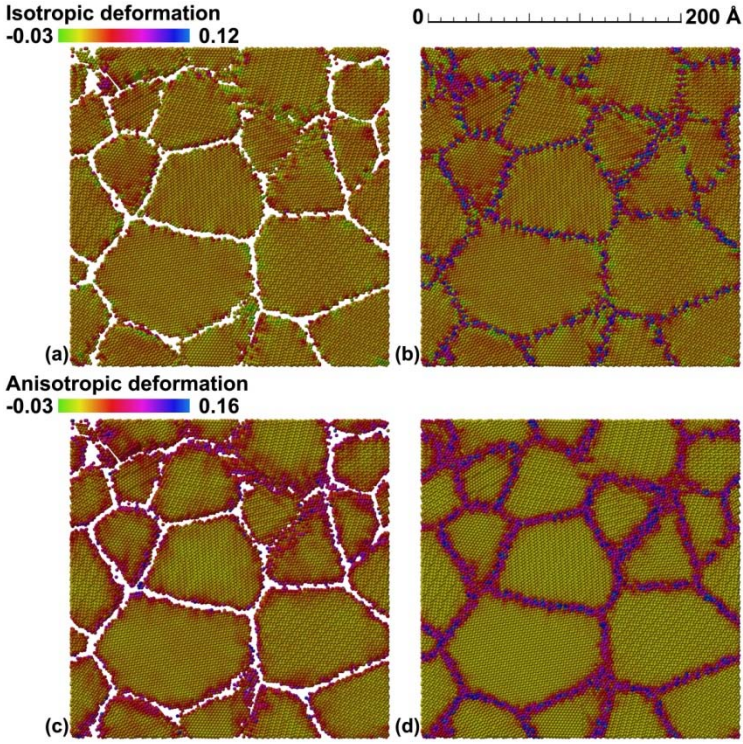

Figure III - 11. Isotropic (a, b) and anisotropic (c, d) strains at the atomic level in a cross-section of the numerical model computed by CCD (a, c) and VCD (b, d) methods for the Averaged Frame (AF) case.

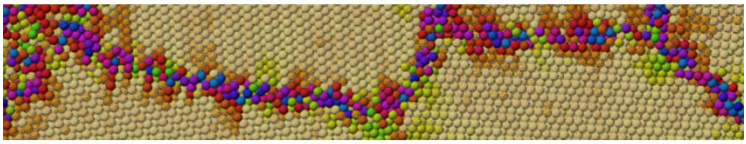

Figure III - 12. Isotropic strain at the atomic level in a cross-section of the numerical model computed by VCD method for the Averaged Frame (AF) case (detail of Figure (11b)).

Once again, one can see clearly from the comparison of the Figures ((11) and (13)), that thermal vibrations are absent in the strain field obtained from the averaging of positions over a large set of frames. Moreover, Figure (14) shows the isotropic strain distributions for the whole cluster computed using the CCD and VCD methods on the SF and on the AF.

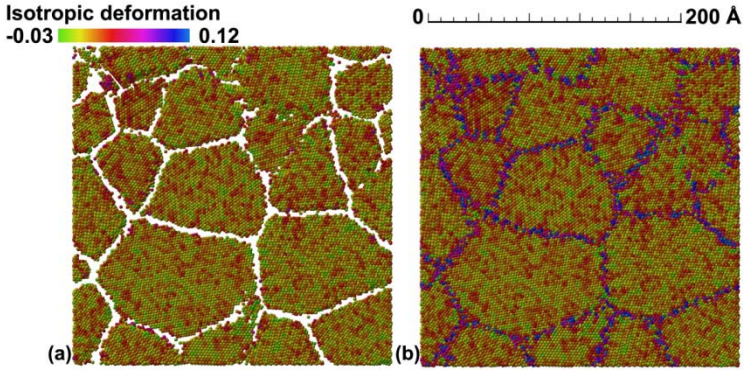

Figure III - 13. Isotropic strain at the atomic level in a cross-section of the numerical model computed by CCD (a) and VCD (b) methods for the Single Frame (SF) case.

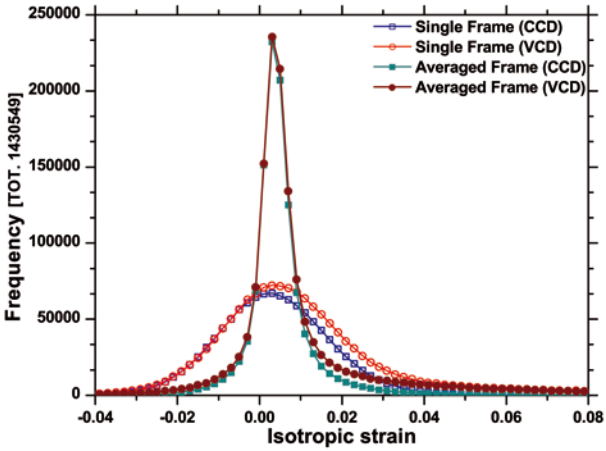

Figure III - 14. Frequency distributions of the local isotropic strain in the numerical model computed by CCD (blue dots) and VCD (red dots) methods for the Single Frame (open symbols) and Averaged Frame (full symbols) cases. In the case of the CCD distributions, the total count is lower than 1430549 because of the not available data for these positions at the grain boundary.

Accounting for the intense deformation at the grain boundary has a dramatic effect on the distribution of the local strain over the whole cluster. The asymmetry in the distributions is caused by the overlapping of the contributions from core and boundary regions. The time average (AF) leads to sharper distributions as the smearing effect of the dynamic contributions is removed. Again, the semi-stochastic nature of the local deformation due to the thermal movement leads to more symmetric distribution functions. A further proof can be obtained from the analysis of the diffraction patterns corresponding to the two cases.

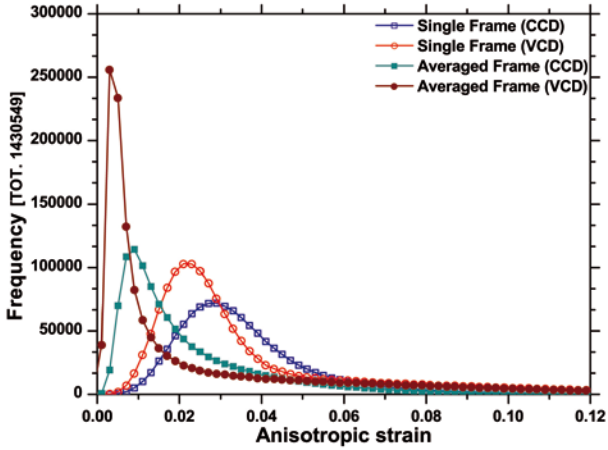

Figure III - 15. Frequency distributions of the local anisotropic strain in the numerical model computed by CCD (blue dots) and VCD (red dots) methods for the Single Frame (open symbols) and Averaged Frame (full symbols) cases. In the case of the CCD distributions, the total count is lower than 1430549 because of the not available data for these positions at the grain boundary.

The anisotropic strain is more deeply affected by the dynamic contribution than the isotropic strain (cf. Fig. (15)). In SF, the local structure is constantly distorted due to the thermal movement. The time dependent distortion is removed by the average of a suitable sequence of frames. The more uniform behaviour of the atoms in the core of the grains allows the averaged local structure to be less affected by a spread anisotropic deformation. Hence, a strong asymmetry in the distribution of the anisotropic strain can be linked to a difference in behaviour of core versus boundary. This pronounced difference allows us to clearly identify the boundary region.

Figure (16) shows the distribution of the isotropic and anisotropic strains at the atomic level associated to the local crystalline symmetry. The latter was defined as:

i. the number of missing neighbours in the case coordination is less than 12;
ii. the number of contiguous shells having fully coordinated neighbours in the case of fully coordinated position.

An inverse correlation is found between the local crystalline symmetry and the variance of the distributions, for both the isotropic and anisotropic components. A sharp discontinuity in the trends appears when crossing the condition of full coordination, finding widely larger values of both isotropic and anisotropic strain distributions. While the position of the isotropic strain distribution is weekly dependent on the local crystalline symmetry, the anisotropic distribution tends to shift to higher strains for decreasing coordination.

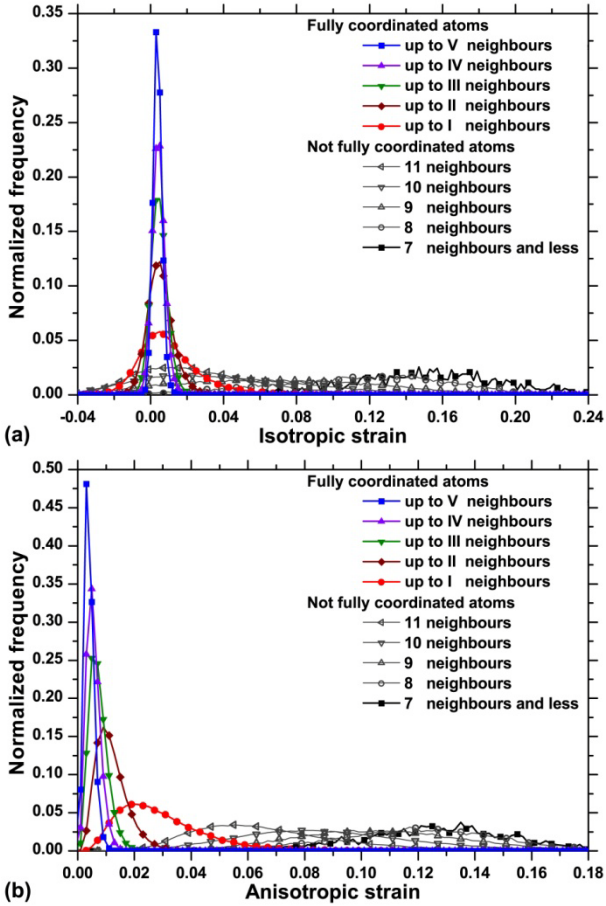

Figure III - 16. Normalized frequency distributions of the local isotropic (a) and anisotropic (b) strains in the numerical model computed by VCD for the Averaged Frame (AF) referred to the local crystalline symmetry (see text for details).

Such behaviour can be explained by taking into account the relation between distortion field and distance from the surface. Linking the distance from the grain surface to the atom layer indexed by progressively "peeling" each grain (removing layers), both strain components (isotropic and anisotropic) and their variances quickly decay (Figure (17)).

The bond between misoriented domains forces the outer layers of each grain to change the atomic arrangement, increasing the local deformation. As a matter of fact, the distortion field tends to disappear far from the core of the defects, and in that regime the deformation can be considered as isotropic. Indeed, figure (17a)

shows an inverse proportionality between grain size and isotropic strain (the lower limit of paths), balancing the expansion and contractions of the neighbouring grains to an equilibrium value over the whole microstructure.

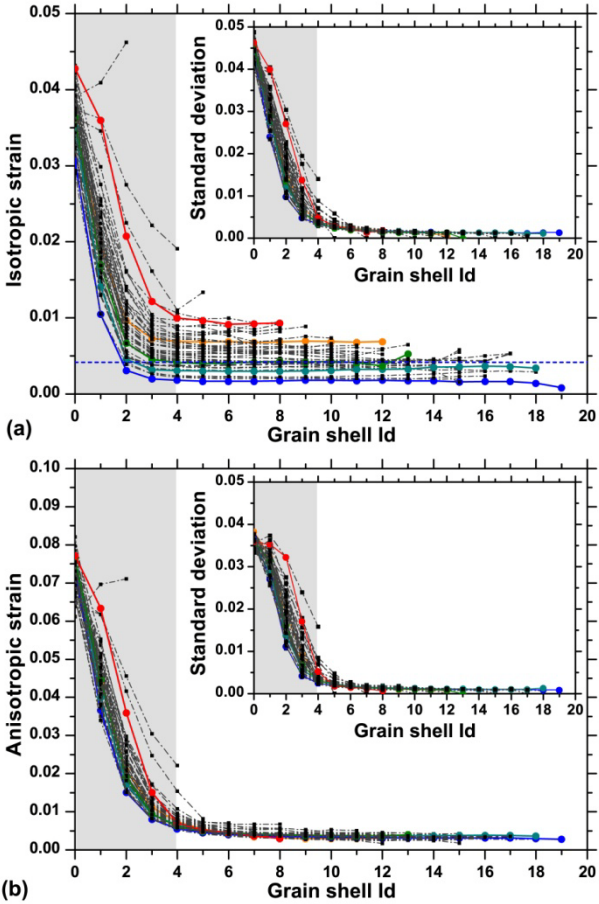

Figure III - 17. Local isotropic (a) and anisotropic (b) strains in the numerical model computed by VCD for the Averaged Frame (AF) referred to the distance from grain surface (expressed as shell id starting from the surface). The average isotropic strain is also provided (blue dash line). Values of each grain are drawn on an independent path (see text for details).

The three principal types of strain in the system (usually quoted when dealing with stress and diffraction (Withers, et al., 2001), vary continuonsly: over large distances (Ist type), over the grain scale (IInd type) or the atomic scale (IIIrd type)) can be clearly identified from the mean isotropic and anisotropic strain computed along a line section in the model (Figure (18)). An isotropic expansion of 0.013 and

anisotropic components of 0.026 are found as type I strain in AF model (computed as the mathematical average of the local strain in the model, as obtained with the reference unit cell parameter of 3.615 Å). Type II and type III of both the isotropic and the anisotropic strains are also visible. In the case of the SF model a significantly broader strain fluctuation appears.

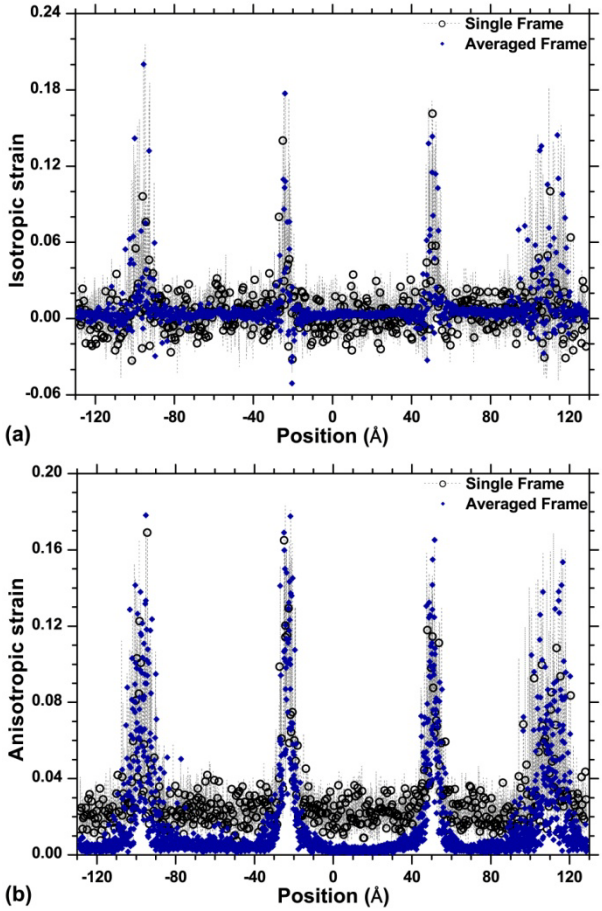

Figure III - 18. Isotropic (a) and anisotropic (b) strain at the atomic level along a line section through the cluster.

This feature hides the marked changes in the strain intensity close to the defects, rendering more difficult to correctly identify the boundary regions. In AF, however, the transition from the core to the boundary zones is clear and extremely sharp. The increasing local strain, especially the anisotropic type, at grain

boundaries agree with the results of Derlet et al. obtained using the physically less rigorous concept of local pressure (Derlet, et al., 2005). Moreover, the anisotropic strain in the SF model and in the AF model showed an evident gap due to the dynamic component. This behaviour further confirms the intrinsic isotropic deformation of the Crystallographic structures in the core of the grains. Hence, when a time average computation is employed, the anisotropic contribution in the grain cores tends to disappear.

3.4.2 Stress – Strain relation in polycrystalline microstructure

The stress at the atomic level and the corresponding potential energy were computed in the numerical model of the Cu nano-polycrystalline microstructure. The average values over all positions within each grain were collected for the AF equilibrated microstructure. The atomic potential energy and unit cell dimension of the Cu microstructure show a direct proportionality (Figure (19)). Nevertheless, this trend significantly deviates from the ideally pure thermal expansion path, as a consequence of local structure distortions near defects.

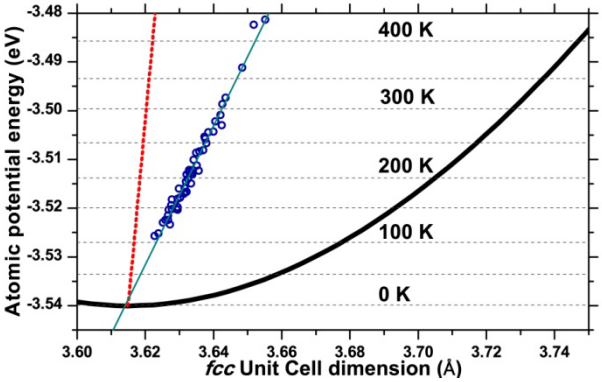

Figure III - 19. Pair potential energy of Cu structure vs. unit cell dimension: ideally infinite single crystal (black line), single grain of equilibrated microstructure (blue open dot) and corresponding linear fit (blue line). Equivalent temperature potential Energy is also provided for some temperature values. Ideal thermal expansion condition (red dot line).

The atomic-level stress, as the hydrostatic II type component, was compared with the corresponding local deformation and energy. Stress, strain and pair potential show an inverse relation with the average grain size (see Figure (20)).The opposite tendency observed for larger and smaller grains (contraction vs. expansion and compression vs. tension, respectively) is due to the equilibrium condition that must be verified by the microstructure as a whole. The topological properties of the tessellation (large grains are surrounded by smaller ones), coupled with this stress/strain trend, results in a steady state at the local level.

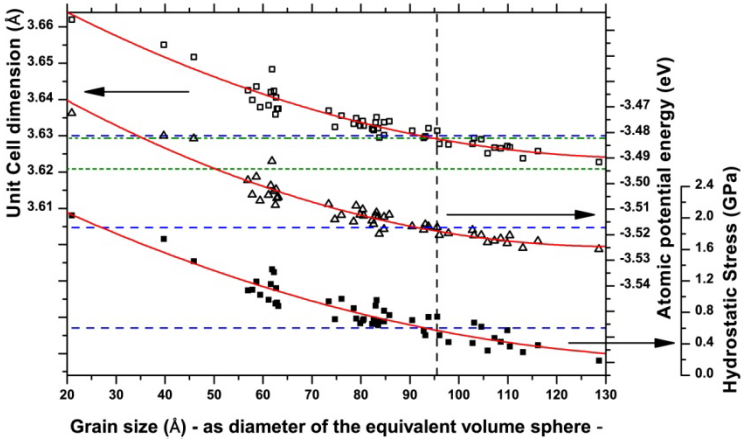

Figure III - 20. Average unit cell (void square), atomic potential Energy (open up-triangle), and hydrostatic stress (full square) vs. grain size as diameter of the equivalent volume sphere. Best fit (red line) and average values of those properties (blue dash line), and weighted average grain size (black dash line) are reported. Equivalent cell dimensions computed from atom density (green dash dot line, $\sqrt[3]{B_{boxside}/\left(N_{atoms}/4\right)}$) and from the average volume of the Voronoi Cell (green short dash, $uc_0\left(V^I_{cell}/V^0_{cell}\right)$) are also shown.

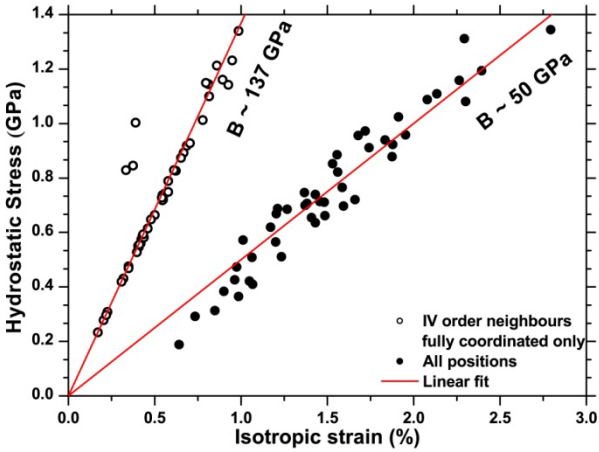

Figure III - 21. Stress - strain relation calculated from all positions (full circle) and from atoms that have fully coordinated neighbours up to the fourth (void circle).The bulk modulus B is the slope of the linear fit passing through the origin.

The bulk modulus was estimated as the slope of the linear fit of hydrostatic stress (pressure) vs. isotropic strain (expansion in volume), crossing the origin (Figure (21)). The tensile stress state at the grain boundaries modifies the local

structure, accommodating the lower atomic density of the misoriented crystal domains. The higher the neighbours distance and the dynamic fluctuation in space (Figures (4c), and (4d)), the higher the potential and the kinetic energy. Thus, computing the average value over each grain, a little variation of the average atom-level stress of each grain is given by the opposite sign of kinetic and positional stress components (see eq. 8). A bulk modulus of 137 GPa (close to the experimental value of 140 GPa) was estimated by including only those positions having fully coordinated neighbours up to the fourth (i.e. excluding grain boundaries). The same calculation made with all atomic positions gives a much lower bulk modulus of 50 GPa.

3.4.3 Preliminary X-ray Diffraction Line Profile analysis

X-ray powder diffraction patterns of the atom ensembles were simulated by the Debye scattering equation (the atomic scale factor from the international tables was employed (Ibers, et al., 1974)) via a fast and accurate code running on Graphic Processing Units (Gelisio, et al., 2010). Several configurations of the same nono-polycristalline microstructure were taken into account. A real X-ray diffraction measurement was simulated by summing a set of patterns simulated for a sequence of SFs (Time Average - TA). Negligible differences are found between the TA and the pattern of a randomly chosen SF (see Figure (22)). Due to this, the SF ensemble fully exploited both static and dynamic (time dependent) features of the atom arrangement in space from a XRD point of view.

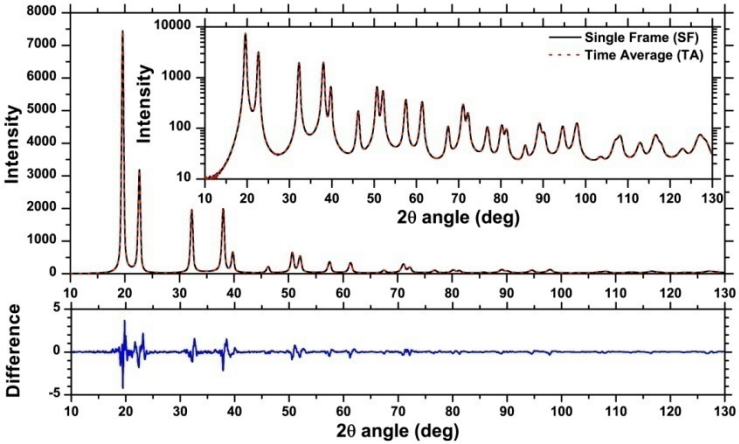

Figure III - 22. X-ray powder diffraction pattern simulated from the atomic positions taken at a single randomly chosen frame (Single Frame, SF) compared with the average of the patterns simulated from a set of randomly chosen frames (Time Average, TA). The Debye scattering equation with MoK_α radiation (wavelength 0.7107 Å) was used.

Differences in the patterns of Single Frame and Averaged Frame are mostly limited to the intensity of peaks and diffuse background: thermal effects are known to decrease the Bragg scattering contribution and to increase the diffuse scattering background, as clear in Figure (23). Moreover, the equivalence between the two Averaged Frame (AF) models (computed by using a set sampled at 1 ps, or a set of sequential snapshots) is supported by the negligible differences of the corresponding XRD patterns.

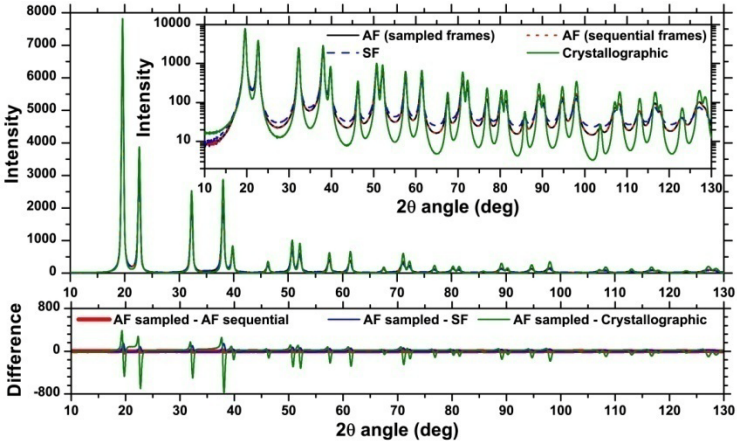

Figure III - 23. X-ray powder diffraction patterns simulated for the Crystallographic model (green line), from the atomic positions taken at a single randomly chosen frame (SF, blue dashed line)and from the time averaged coordinates of sampled and sequential frames(respectively: AF sampled, black line, and AF sequential, red dot line). Differences between the patterns are provided below (see text for details).

A preliminary line profile analysis, made by the Williamson-Hall (WH) method (Williamson, et al., 1953) on unique reflections (Figure (24)), further confirms that strain effects are similar in the single frame and in the averaged ensemble.

The slope in the WH plot is related to the so-called microstrain or root-mean-strain, a quantity that cannot be directly related to an average pressure or an average strain. The standard deviation of the volumetric strain distribution is a more realistic quantity to be compared with the slope (equal to $2\langle\varepsilon^2\rangle^{1/2}$ according to the WH formulation), and comparable values are indeed obtained (0.0288 / 0.0261 Figure (14) vs. 0.0080 / 0.0074 as slope in Figure (24) – for SF and AF respectively). However, no exact match is to be expected because (i) peak profiles were analysed with empirical line profile functions and (ii) hypotheses underlying the WH method are far from being fulfilled in this case (see discussion in (Scardi, et al., 2004(b))).

The use of the WH method in this case is limited to a qualitative assessment of the line broadening effects and order-of-magnitude estimates. The little difference in the slopes of the two fits in Figure (24) is likely due to the presence of a thermal

dynamic strain in the nano-crystalline sample at a short time (a single frame). The anisotropic broadening observed in the WH plot is not fully compatible with the elastic tensor, thus anisotropic strain broadening effects, if present at all, are not dominant. Last, relating the intercept of the WH plot with an average domain size, as commonly done in traditional Line Profile Analysis, can lead in this case to large errors due to the limited number of grains employed in the analysis and their non-ideal shape. The order of magnitude (linear fit: 11.2 nm for Crystallographic and 13.3 nm for the equilibrated models; parabolic fit: 10.8 nm for Crystallographic and 10.1 nm for the equilibrated models) is however compatible with the average size of the grains (9.6 nm for Crystallographic and 9.9 for the equilibrated models).

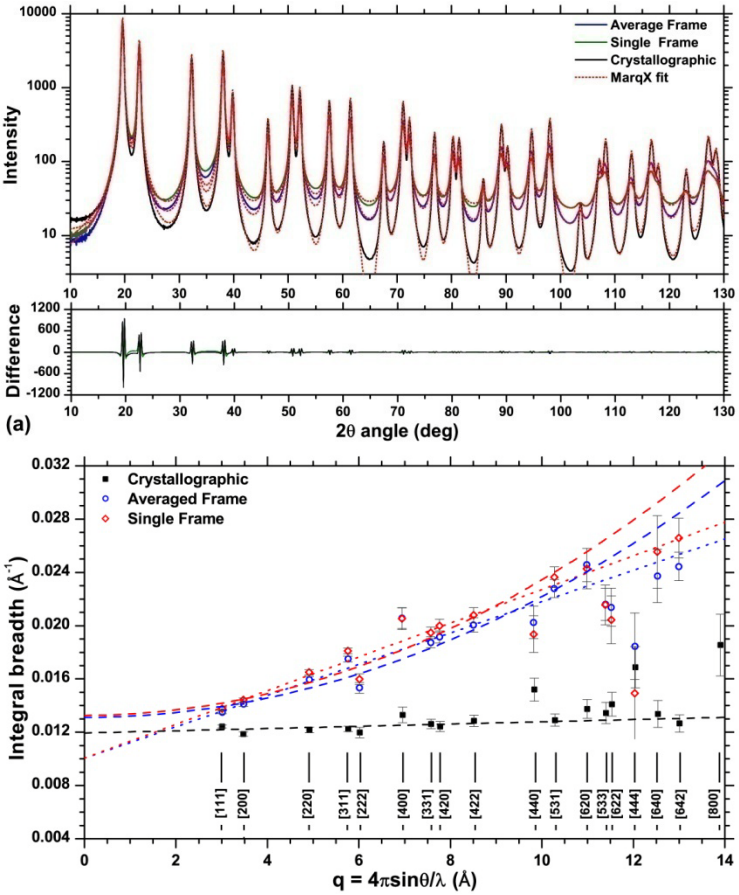

Figure III - 24. (24)Line Profile Analysis of the simulated pattern for SF, AF, and Crystallographic models done using the MarqX software (Dong, et al., 2000). Best patterns fit (a) and Williamson-Hall analysis (b) are provided.

3.5 Conclusion

A new method has been presented for computing the strain at the atomic level. Grouped under the name of Voronoi Cell Deformation (VCD), the different forms of the proposed algorithm are all based on a Voronoi Tessellation to identify the local atomic arrangement. The principal stretch ratios are computed from the differences of the inertia between the real and a reference configuration, also considering a uniform or a concentrated distribution of mass. The use of tessellation allows strains to be computed also in the grain boundary regions where traditional methods based on the local crystallography cannot be used.

VCD was compared with the known CCD method for the analysis of a simulated Cu nano-polycrystalline microstructure. Contrary to the CCD, which does not allow highly distorted regions to be considered, the VCD is able to provide information in any point in the cluster. A marked difference in behaviour is detected in the grains between core and boundary. A distribution of the strain with large changes at the interface between grains is shown by studying the strain along linear sections in the cluster. Differences between the results of CCD and VCD are as expected, as the latter considers all atoms, including those in highly deformed positions, as in the grain boundary regions.

The atom-level stress was computed on the base of EAM potential energy, involving the Voronoi cells associated to each atomic position. A linearly proportional relation between grain size and stress-strain components is found, agreeing with the same trend for potential energy. Moreover, the bulk modulus of the equilibrated microstructure computed from stress and strain at the atomic level (137 GPa) results almost the same to the experimental value (140 GPa).

Finally, a preliminary discussion about X-ray powder diffraction Line Profile Analysis from simulated nano-polycrystalline microstructure is provided, showing differences between patterns simulated via the Debye scattering equation for the same microstructure under several conditions. A qualitative estimation of microstrian in the Cu microstructure was evaluated by the Williamson-Hall analysis, finding discrepancy from values directly measured from the numerical model.

3.6 Appendix III.A: Deformation of convex polyhedron from volume properties

The deformation of a convex polyhedron is proportional to the change in the geometric properties such as the moments of volume. The latter are easily computed e.g. by the equations proposed by A. V. Tuzikov et al. (Tuzikov, et al., 2003). In particular, as the VCs are convex polyhedron (bound by polygonal faces), they can be decomposed into tetrahedron that divide the faces into triangles (Figure (25)).

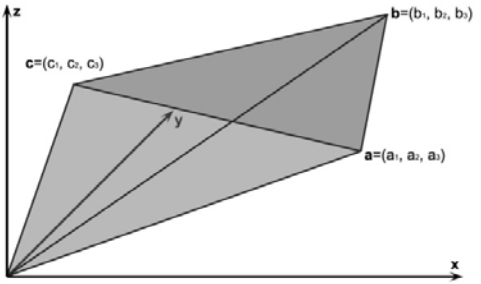

Figure III - 25. Geometric description of a tetrahedron in space.

If we define the matrix:

$$\mathbf{A} = \begin{pmatrix} a_1 & b_1 & c_1 \\ a_2 & b_2 & c_2 \\ a_3 & b_3 & c_3 \end{pmatrix} \tag{9}$$

we can calculate the moment of mass of the whole polyhedron P:

$$m_{P,str} = \sum\nolimits_T m_{T,str} \tag{10}$$

in terms of the moments of mass of the N composing tetrahedron T:

$$m_{T,str} = \int_T \left(x_i^s x_j^t x_k^r \right) dx_i \, dx_j dx_k \tag{11}$$
$$i, j, k = 1 \ldots 3 \quad i \neq j \neq k$$

Just three moments of mass for each tetrahedron:

$$m_{T,100} = \tfrac{1}{24} \left| \mathbf{A} \right| \left(a_1 + b_1 + c_1 \right) \tag{12}$$

$$m_{T,101} = \tfrac{1}{120} \left| \mathbf{A} \right| \left(2a_1a_3 + a_1b_3 + a_1c_3 + a_3b + 2b_1b_3 + b_1c_3 + c_1a_3 + c_1b_3 + 2c_1c_3 \right) \tag{13}$$

$$m_{T,200} = \tfrac{1}{60} \left| \mathbf{A} \right| \left(a_1^2 + b_1^2 + c_1^2 + a_1b_1 + a_1c_1 + b_1c_1 \right) \tag{14}$$

suffice to calculate the whole moment of inertia tensor I_P:

$$\mathbf{I}_P = \begin{pmatrix} m_{P,020} + m_{P,002} & -m_{P,110} & -m_{P,101} \\ -m_{P,110} & m_{P,200} + m_{P,002} & -m_{P,110} \\ -m_{P,101} & -m_{P,110} & m_{P,200} + m_{P,020} \end{pmatrix} \tag{15}$$

The principal moments and directions of inertia can be then computed as the eigenvalues and eigenvectors of I_P:

$$\mathbf{I}_P^0 = \begin{pmatrix} I_{ii} & 0 & 0 \\ 0 & I_{jj} & 0 \\ 0 & 0 & I_{kk} \end{pmatrix} \tag{16}$$

Linking the inertia values of the VCs to the equivalent parallelepiped solids, the three positive stretch ratios are fully defined by the equations:

$$\lambda_n = \frac{L_{F,n}}{L_{0,n}} \qquad \Leftrightarrow \qquad x_{F,n} = \lambda_n x_{0,n} \qquad\qquad n = i, j, k \tag{17}$$

$$J_{kk} = (I_{ii} + I_{jj} - I_{kk})/2 = \frac{x_i x_j x_k^3}{12} \tag{18}$$

$$\frac{J_{F,kk}}{J_{0,kk}} = \frac{x_{F,i} x_{F,j} x_{F,k}^3}{12} \frac{12}{x_{0,i} x_{0,j} x_{0,k}^3} = \frac{\left(x_{0,i} x_{0,j} x_{0,k}^3\right) \lambda_i \lambda_j \lambda_k^3}{\left(x_{0,i} x_{0,j} x_{0,k}^3\right)} = \lambda_i \lambda_j \lambda_k^3 \tag{19}$$

$$\lambda_k = \left[\left(\frac{J_{F,kk}}{J_{0,kk}} \right)^4 \Bigg/ \left(\frac{J_{F,ii} J_{F,jj}}{J_{0,ii} J_{0,jj}} \right) \right]^{1/10} \tag{20}$$

where L_F and L_0 are the final (F) and initial (0) lengths, respectively.

3.7 Appendix III.B: Deformation of convex polyhedron from mass properties

When concentrated masses are considered, equation (10) is replaced by:

$$m_{P,str} = \sum_T w_T x_i^s x_j^t x_k^r \tag{21}$$

where $w_T = S_T / S_P$ or $w_T = 1$ for the weighted and non-weighted VmmCD, respectively. The term S_T is the surface area of the face of tetrahedron T shared with the polyhedron P, whereas S_P is the total surface area of the polyhedron.

The stretch ratios along the principal directions can be directly computed without any additional assumption from the principal inertia of the deformed and reference structures:

$$\lambda_k = \left[\frac{I_{F,ii} + I_{F,jj} - I_{F,kk}}{I_{0,ii} + I_{0,jj} - I_{0,kk}} \right]^{1/2} \tag{22}$$

Chapter IV

Interference Effects in Nano-crystalline Systems

Part of this chapter has been published in:

Alberto Leonardi, Matteo Leoni, Paolo Scardi,

"Interference Effects in Nanocrystalline Systems",
Metallurgical and MaterialsTransactions A,(2012) in press.

4.1 Abstract

Interference (inter-grain cross-correlation) effects can be present in the X-ray powder diffraction pattern of a polycrystalline aggregate. In an experimental diffraction pattern, however, the information is highly overlapped and can be confused with other effects. It is here shown that the analysis of the patterns calculated from a cluster equilibrated via molecular dynamics simulation allows those effects to be separated. Extra intensity is observed due to the presence of the grain boundaries whose contribution is unexpectedly not that of an amorphous phase.

4.2 Introduction

Recent work has shown how inter-grain interference effects can be observed in the diffraction from polycrystalline systems when scattering domains are sufficiently small and textured ((Rafaja, et al., 2000), (Rafaja, et al., 2004), (Rafaja, et al., 2006), (Rafaja, et al., 2007), and (Förster, et al., 2007)). Besides loose nano-crystalline powders, where the above conditions can arise from special growth or coalescence phenomena ((Link, et al., 1999), (Scardi, et al., 2010)), these effects are important also in polycrystalline aggregates as they can influence the overall properties of the system (Rafaja, et al., 2006).

Models have been proposed to describe the special condition when the diffracted intensity distributions from small and closely oriented domains overlap in Reciprocal Space (RS), thus affecting the observed powder patterns in different ways ((Rafaja, et al., 2000), (Rafaja, et al., 2004), (Rafaja, et al., 2006), (Rafaja, et al., 2007), and (Förster, et al., 2007)). This is especially visible for low Miller indices peak profiles, whose corresponding RS points are closer to the origin. Further insights have been provided by a recent work, where interference effects among man-sized metallic domains where simulated using atomistic models and the Debye scattering equation (DSE) ((Debye, 1915), (Gelisio, et al., 2012)) to generate the corresponding powder patterns ((Beyerlein, et al., 2010), (Gelisio, et al., 2012)).

In all of these cases, however, interference was related to the size and orientation of the domains with no consideration of the role of grain boundaries, which indeed contribute a considerable fraction to nano-scale materials (see e.g. (Krivoglaz, 1996), (Barabash, et al., 1999), (Levine, et al., 2011)). Models and simulations so far have treated nano-crystals as small (perfect) single crystals, without accounting for the boundary region and of the natural tendency of the system to achieve a minimum of energy. Here we provide a preliminary understanding of the possible effects of the grain boundary (GB) on the diffraction patterns from systems made of small crystalline domains. In particular it is shown that the signal from the GB region can be partly coherent with the bulk of the neighbouring crystalline domains.

4.3 Generation of the nano-polycrystalline model

A nano-polycrystalline cluster made of 50 grains of Cu was built via Constrained Voronoi Tessellation (CVT (Gross, et al., 2002)) in a cubic box of 260.28 Å with PBCs (1). Using this technique, the size and shape of the grains was tuned to obtain a lognormal dispersion of normalised volumes (mean volume 352657 Å3, standard deviation = 0.35; the diameter of a sphere having the mean volume is ca. 70 Å). The distribution character was confirmed by the Kolmogorov-Smirnov test at 5% significance level. An *fcc* copper structure (cell parameter a = 3.615 Å) was placed in

the grains, eliminating those atoms on the boundary whose distances are below 85% of the minimum ideal value $(3.615/\sqrt{8})$ (Xu, et al., 2010). The distribution of misorientation angles agrees with the MacKenzie result (Mackenzie, 1958) associated to a randomly textured material.

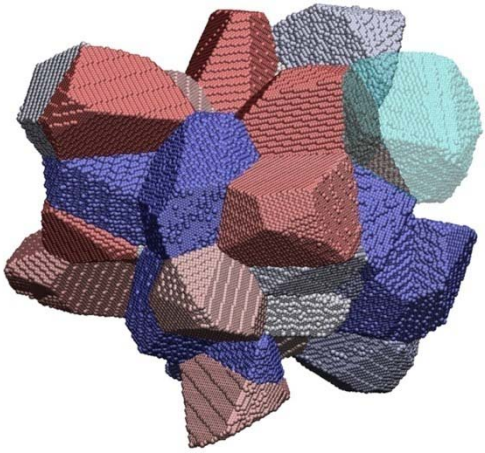

Figure IV - 1. Cluster employed for the MD simulation (Copper nano-polycrystalline microstructure of 50 grains).

The system was equilibrated at 100 K under NPT conditions using molecular dynamics and the Embedded Atom Method potential for Cu ((Daw, et al., 1983), (Foiles, et al., 1986)). The LAMMPS code (Plimpton, 1995) was employed.

Once stationary conditions were reached, a sequence of 100 independent frames was collected each 1 ps. The position of each atom (labelled with the grain ID) was averaged over the collected dataset in order to remove any dynamic (thermal) component (Leonardi, et al., 2011). A powder diffraction pattern was computed via DSE for each of those averaged datasets; the PowDOG (Gelisio, et al., 2010) code running on a cluster of NVIDIA GPUs was employed. Because of the averaging, these diffraction patterns contain only information on size and static displacements: local distortion, non crystalline features and defects contributions to line profile broadening can therefore be more easily separated.

4.4 Results and Discussion

When the DSE is used for the cluster as a whole, the resulting powder pattern includes correlation effects between all atoms, whether they belong to same or different grains, to the core or to GB regions. The range of the powder pattern comprising the (111) and (200) copper peaks is shown in Figure (2) for the

equilibrated cluster, together with the corresponding pattern obtained by summing up all DSE patterns for each separate grain. A detail of the process is shown in the inset.

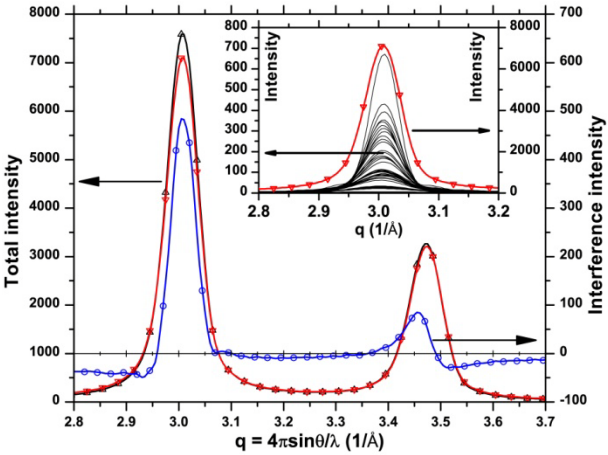

Figure IV - 2. Portion of the X-ray powder diffraction pattern of the cluster (black, up triangles) compared with the corresponding sum of the patterns from the component grains (red, down triangles): the difference coming from the grain-grain interference is evidenced (IEP - blue, circles). As an example, the inset shows the (111) peaks from the various grains (black lines) and their sum (red, down triangles).

To study the interference effects we can use a plot of the difference between those contributions i.e. between the pattern of the cluster and the sum of the patterns of the contributing grains (Interference Effects Plot, IEP).The IEP can is directly provided by the DSE using the cross-corelation pairs of atoms owned by different grains of the polycrystalline microstructure (see eq. (1)).

$$IEP(q) \propto \sum_{p=1}^{M} \sum_{\substack{t=1 \\ t \neq p}}^{M} \left\{ \sum_{i=1}^{n_p} \sum_{j=1}^{n_t} f_i(\mathbf{q}) f_j(\mathbf{q}) \frac{\sin(\mathbf{r}_{ij} \cdot \mathbf{q})}{\mathbf{r}_{ij} \cdot \mathbf{q}} \right\} \qquad (1)$$

where M is the number of grains, n_p and n_t are the number of atoms within the grains p and t respectively, $\mathbf{r}_{ij}$ is the pair vector, and $\mathbf{q}$ is the scattering vector. As shown in this and in the following figures, the effect is clearly visible and is peaked around the Bragg positions.To further understand the origin of the interference component it is useful to compare the DSE pattern for whole cluster and sum of separate grains in three distinct cases (cf. Figure (3)): (i) for the starting microstructure, just after the atom filling step, which is then made of “perfect” crystals; (ii) after the energy minimization step and (iii) after a MD trajectory sufficiently long to equilibrate the microstructure (same as in Figure (2)). The main effect of the energy minimization is a shift of Bragg peaks with respect to case (i),

caused by the expansion of the cells that better fill the intergranular regions. The MD equilibration has a more complex effect (still driven by energy minimization), leading to a reorganization of the atoms in the GB region. A diffuse scattering component – especially visible in the region between the Bragg peaks – arises at the expenses of the Bragg component, as an effect of the disordered structure of the GB region in the equilibrated model (iii).

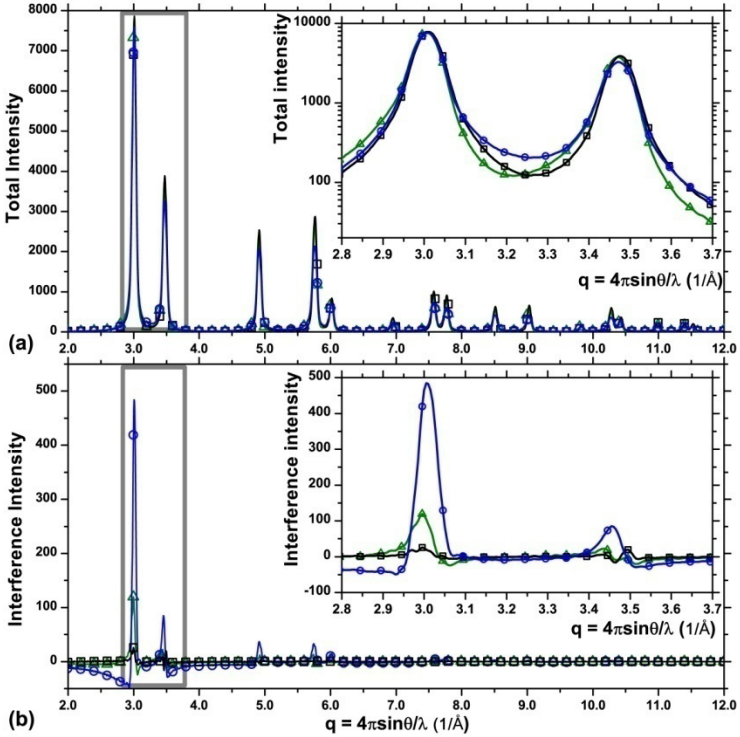

Figure IV - 3. In the upper plot (a), X-ray powder diffraction pattern for the cluster calculated for the starting microstructure (black squares), after energy minimization (green upper triangles) and after a long equilibration (blue, circles). The rectangle indicates the portion of the pattern considered in Figure (2). In the lower plot (b), IEPs corresponding to the three cases presented in the upper part. See text for details.

The IEPs in the lower part of Figure (3) show that interference effects are quite small for (i), in agreement with the recent study by Gelisio and Scardi (Gelisio, et al., 2012). Quite surprising the interference component increases with energy minimization (ii) and even further after MD equilibration (iii). As already pointed out, the latter step mostly rearranges atoms in the GB region, with negligible grain

rotations; it is therefore clear that the main contribution to interference comes from the grain boundary.

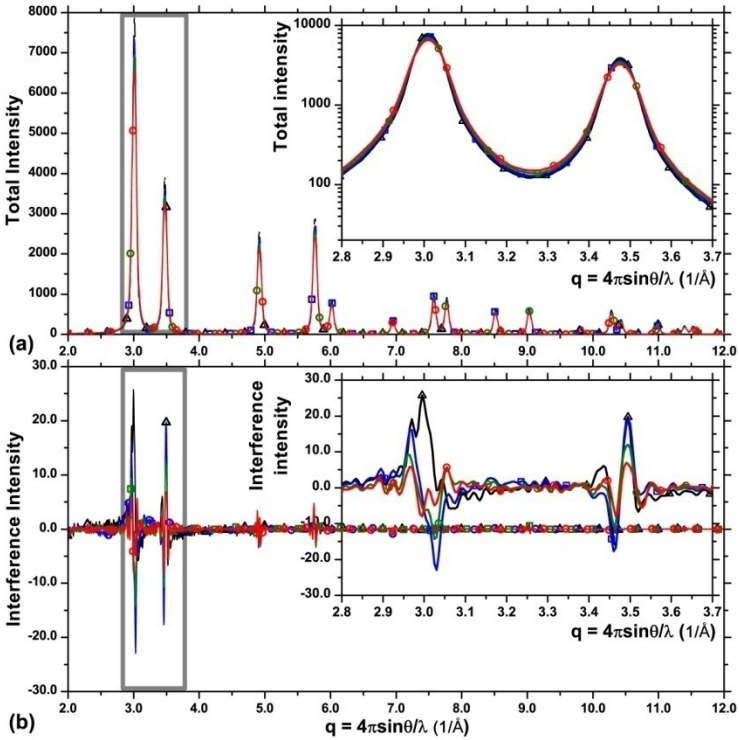

Figure IV - 4. Grain boundary contribution. In the upper part (a), the pattern of the "perfect" cluster (black squares) together with those obtained by removing 1 layer (CL1 - blue upper triangles), 2 layers (CL2 - green, down triangles) and 3 layers (CL3 - red, circles). The rectangle indicates the portion of the pattern considered in Figure (2). In the lower plot (b), IEPs corresponding to the three cases presented in the upper part. See text for details.

The contribution of the GB is made evident by the following analysis. The powder pattern of the "perfect" crystalline cluster (case (i) above) can be compared with that of the same cluster after removing all atoms with a coordination lower than 12 (CL1), or after removing all atoms whose first (CL2) or second (CL3) neighbours have coordination lower than 12. This corresponds to progressively remove (peel off) the atoms from each grain layer-by-layer, thus removing the grain boundary region. This is shown in Figure (4) for the starting perfect crystal microstructure (i). In this case, as already discussed, the interference effect is small; the further decrease observed in CL1, CL2, CL3 is mostly due to the volume decrease, which is also the reason for the broadening of the Bragg peaks (easily visible in the top right inset).

The same analysis is shown in Figure (5) for the MD equilibrated cluster (iii). In this case we can see that the first removal step (CL1), contrary to what just observed for (i), gives a sharpening of the Bragg peaks, as a consequence of the removal of the diffuse scattering component caused by the GB. It is also apparent (bottom right inset) that interference effects are strongly reduced in CL1 and comparable to (i) for CL2 and CL3. This further validates the results on the role of the GB in the interference phenomenon. Finally, Figure (6) shows the DSE calculation obtained by considering just: (a) CORE-CORE: correlations between atoms in the core of the grains only (i.e. all GB atoms are excluded); (b) BOUNDARY-BOUNDARY: correlations between GB atoms only; (c) CORE-BOUNDARY: correlations between GB atoms and atoms of the grains. The analysis is then repeated for the CL1, CL2 and CL3 clusters, so that the sum of (a), (b) and (c) gives the corresponding CL1, CL2 and CL3 patterns in Figure (5).

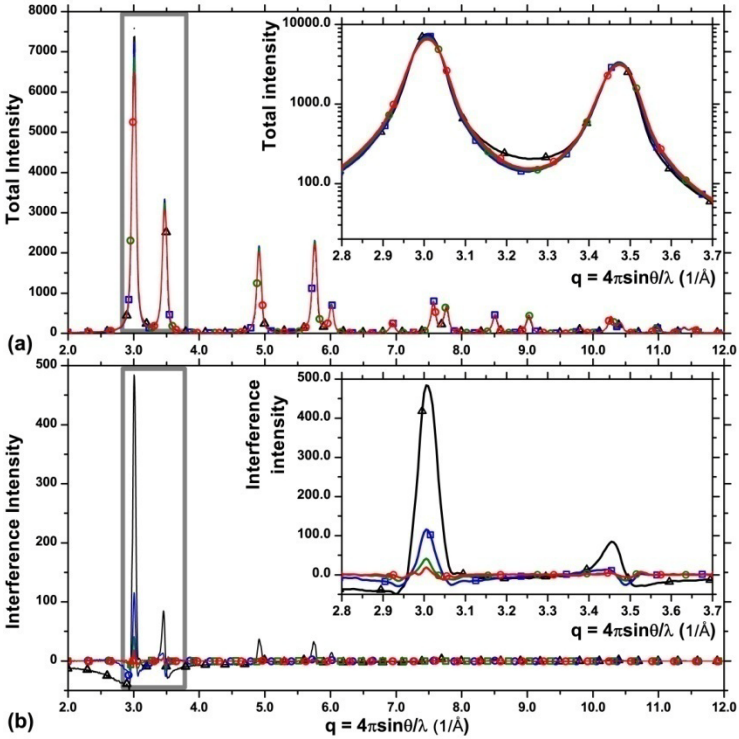

Figure IV - 5. Grain boundary contribution. In the upper part (a), the pattern of the equilibrated cluster (black squares) together with those obtained by removing 1 layer (CL1 - blue upper triangles), 2 layers (CL2 - green, down triangles) and 3 layers (CL3 - red, circles). The rectangle indicates the portion of the pattern considered in Figure (2). In the lower plot (b), IEPs corresponding to the three cases presented in the upper part. See text for details.

The first group (a) gives powder patterns typical of *fcc* structures, with a progressive broadening of the Bragg peaks caused by the decrease in grain size, from CL1 to CL3. The pattern produced by GB atoms (b) gives a main diffuse scattering component with a Bragg component which is only visible for low Miller indices; the latter effect is due to the high disorder in the GB that enhances line broadening with the scattering vector until it cannot be distinguished from the diffuse scattering component anymore. For increasing layer removal, the Bragg component sharpens as it includes more correlations between distant atom couples. The last group (c) shows that the correlation between GB atoms and grain cores also consists of a diffuse scattering component, but the Bragg signal is stronger than in (b).

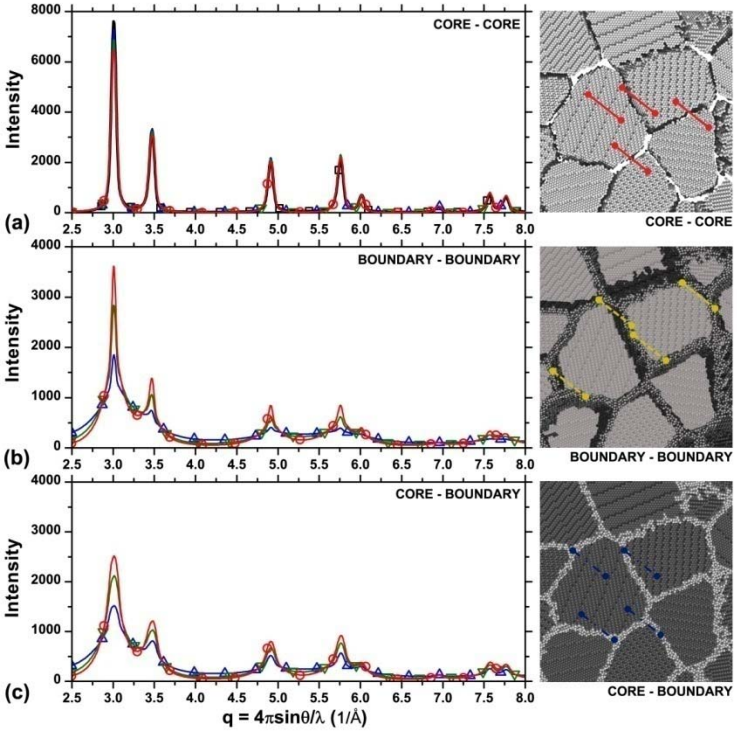

Figure IV - 6. DSE calculations obtained by considering just: (a) CORE-CORE, correlations between atoms in the core of the grains, (b) BOUNDARY-BOUNDARY, correlations between GB atoms only; (c) CORE-BOUNDARY, correlations between GB atoms and atoms of the grains. In the three cases, plots represent the CL1 (blue upper triangles), CL2 (green, lower triangles) and CL3 (red circles) clusters.

An experimental validation of the arguments presented here is difficult in practice, as it is impossible to separate in this easy way the constituents of an

experimental diffraction pattern. The results are therefore tightly bound to the performance of the MD (thus to the choice of microstructure and potentials) and to its appropriateness in representing the microstructure of the cluster analysed here. MD is known to provide a realistic representation of a material when limited to equilibration effects like those shown here. Moreover, the use of a particular MD model does not change the fact that GB is clearly different from the core: it is therefore likely that interference effects due to the presence of the GB are present in a real microstructure as well.

4.5 Conclusions

Molecular dynamics applied to a nano-polycrystalline cluster allowed the various contributions to the diffraction pattern (static, thermal, defects, grain boundaries) to be singled out. In particular, it was here shown that the diffraction pattern of a cluster is not the mere sum of the contributions from all grains, but additional diffuse and broadening effects are present. These effects are due to the interference of the grains in the cluster, and in particular they are mainly caused by the particular structure of grain boundaries.

Chapter V

Common Volume Function & Diffraction Line Profiles

Part of this chapter has been published in:

Alberto Leonardi, Matteo Leoni, Stefano Siboni, Paolo Scardi,

"Common Volume Function and diffraction line profiles from polyhedral domains",
Journal of Applied Crystallography,45-6 (2012) 1162-1172.

5.1 Abstract

A general numerical algorithm is proposed for the fast computing of the Common Volume Function (CVF) of any polyhedral object, from which the diffraction pattern of a corresponding powder can be obtained. The theoretical description of the algorithm is supported by examples ranging from simple equilibrium shapes in cubic materials (Wulff polyhedra) to more exotic non-convex shapes such as e.g. tripods or hollow cubes. An excellent agreement is shown between the patterns simulated using the CVF and the corresponding ones calculated from the atomic positions *via* the Debye scattering equation.

5.2 Introduction

The inverse proportionality between peak width and size of crystalline domains is one of the best-known and exploited properties of X-ray diffraction: first formalized in 1918 by P. Scherrer (Scherrer, 1918) for a powder of small crystals, it has since been discussed within more complex and general theories on peak profiles in diffraction (see, e.g., (Wilson, 1962), (James, 1962), (Guinier, 1963), (Warren, 1969)).

The finite size and the shape of coherently scattering domains (or crystallites) – typically in a range from a few to several hundreds of nanometres – is just one of the possible imperfections affecting the diffraction peaks. Besides domain size effects, detailed models exist to study e.g., several lattice defects, inhomogeneous strains and compositional variations, forming a large body of knowledge and methods usually referred to as (diffraction) Line Profile Analysis (LPA).

Despite the popularity of LPA, whether using the simple Scherrer formula or more advanced full pattern modelling methods, few domain shapes have been considered so far. Models providing the powder diffraction line profile and related properties like the Scherrer constant (Langford, et al., 1978) are available for just a few regular shapes, including sphere, cube, tetrahedron, octahedron, cylinder, hexagonal prism, and some derived shapes, like ellipsoids and parallelepipeds ((Langford, et al., 1978), (Allegra, et al., 1983), (Scardi, et al., 2004(a)), (Ungàr, et al., 2005)).

The basic property to study domain size and shape effects in powder diffraction is the Common Volume Function (CVF). Following Stokes and Wilson ((Stokes, et al., 1942), (Wilson, 1962)), the CVF is the intersection volume $V_{\Omega,hkl}(L)$ between a crystalline domain Ω of volume V_{grain} and its "ghost" (T(Ω)), i.e., the same domain shifted by L along the scattering vector direction $\hat{\mathbf{d}}_{[hkl]}$ (Figure 1). As shown in textbooks ((Wilson, 1962), (Guinier, 1963), (Warren, 1969)), the line profile $I_{\Omega,hkl}(q)$ of the hkl reflection, can be obtained as the cosine Fourier Transform (FT) of the normalised CVF $A^S_{\Omega,hkl}(L) = V_{\Omega,hkl}(L)/V_{\Omega,hkl}(0)$ where $V_{\Omega,hkl}(0)$ is the volume of the grain:

$$I_{\Omega,hkl}(q) \propto \int_0^\infty A^S_{\Omega,hkl}(L)\cos(qL)\,dL \qquad (1)$$

where $q = 2\pi s = 4\pi \sin\theta/\lambda$ (where θ is half of the scattering angle, and λ is the wavelength of the incident radiation beam). Terms adsorbed in the proportionality symbol include several constants, known trigonometric functions, the square modulus of the structure factor and the multiplicity of the hkl reflection (Warren, 1969). It can be noted that eq. (1) does not contain the sine FT term, as the CVF is

always a real and even function in L (i.e. $A^S_{\Omega,hkl}(L) = A^S_{\Omega,hkl}(-L)$). The integration is extended to infinity, but is actually limited by the longest dimension along [hkl], beyond which the CVF is null: the upper limit is therefore a direction-dependent quantity. Furthermore, eq. (1) is valid within the limit of the so-called Tangent Plane Approximation (TPA), which is usually appropriate for not too small crystallites. The CVF concept, however, can be equally used in more rigorous expressions of the line profile (Beyerlein, et al., 2011).

Besides line profiles, the CVF provides direct information on the average thickness of the crystallite along [hkl] ((Wilson, 1962), (Scardi, et al., 2004(a))). In fact, we can define:

$$< L >_{V,hkl} = \frac{1}{\beta_{hkl}(s)} = 2\int_0^\infty A^S_{\Omega,hkl}(L)\,dL \tag{2}$$

$$< L >_{S,hkl} = -\left[\left.\frac{dA^S_{\Omega,hkl}(L)}{dL}\right|_{L=0}\right]^{-1} \tag{3}$$

as, respectively, volume and surface weighted sizes of the crystallite Ω along [hkl] (also known as apparent or effective crystallite sizes, or as mean column length; see (Scardi, et al., 2004(a)) and references therein). Equation (2) also provides the integral breadth β_{hkl} (peak area over peak maximum), and can be considered as a generalization of the Scherrer equation.

When applied to simple domain shapes with just one length parameter D (e.g., diameter for the sphere, edge for the cube, etc.), eq. (2) gives:

$$< L >_{V,hkl} = \frac{1}{\beta_{hkl}(s)} = \frac{\lambda}{\cos\theta\cdot\beta_{hkl}(2\theta)} = \frac{D}{K_\beta} \tag{4}$$

where the Scherrer constant K_β in the denominator (of the order of magnitude of unity) generally depends on the shape of Ω and on [hkl] ($K_\beta(hkl)$), except for spherical crystallites where $K_\beta = 4/3$ for any [hkl] ((Langford, et al., 1978), (Scardi, et al., 2004(a))).

Equation (4) is probably the most popular form of Scherrer equation, written for the integral breadth in the usual (2θ) measurement space. However, as shown e.g. in (Scardi, et al., 2004(b)) and (Scardi, et al., 2006), the practical use of Scherrer equation is quite limited, as the formula does not include all possible sources of broadening and does not consider e.g. the size polydispersity typical of real systems. The CVF can however be used beyond Scherrer equation e.g. within the frame of the Whole Powder Pattern Modelling (WPPM, (Scardi, et al., 2002)), the state-of-art convolutive method for microstructure analysis based on powder diffraction. In particular, as the size distribution and shape effects can be separated (as shown in (Scardi, et al., 2004(a))), the knowledge of the CVF allows the analysis of

polydispersed powders. From the above it is quite evident that the CVF is the most relevant information needed for application of LPA to powders or polycrystalline materials with crystallites of any desired shapes. The present chapter shows how the CVF can be easily calculated and used to generate the diffraction line profiles for any polyhedral shape. This choice seems sufficiently general and flexible, as nearly any possible domain shape can be at least approximated by a polyhedron with an appropriate number of faces. The new algorithm is briefly described and its application illustrated by several examples.

5.3 Common Volume Function of polyhedral crystallites

A notable property of polyhedra is convexity: in a convex polyhedron, the faces do not intersect and any segment joining two points is entirely contained within the body. As shown in the following, this property plays a key role in the calculation of the CVF, which is first discussed for domains of convex shape.

5.3.1 Convex polyhedra

Choosing an orthogonal reference system with origin O anywhere in the space, a generic convex polyhedron Ω with *N* faces (see Figure (1)) can be mathematically described by the set of all points $\mathbf{P}_k$ satisfying the following system of *N* inequalities (half-space representation):

$$\Omega = \begin{cases} \hat{a}_{1,x} \cdot P_{k,x} + \hat{a}_{1,y} \cdot P_{k,x} + \hat{a}_{1,z} \cdot P_{k,z} \le r_{a,1} \\ \qquad\qquad \ldots \\ \hat{a}_{N,x} \cdot P_{k,x} + \hat{a}_{N,y} \cdot P_{k,y} + \hat{a}_{N,z} \cdot P_{k,z} \le r_{a,N} \end{cases} \qquad (5)$$

$$\Updownarrow$$

$$\Omega = \begin{cases} \hat{\mathbf{a}}_1 \cdot \mathbf{P}_k \le r_{a,1} \\ \qquad \ldots \\ \hat{\mathbf{a}}_N \cdot \mathbf{P}_k \le r_{a,N} \end{cases}$$

where $\hat{\mathbf{a}}_i$ is unit normal from inside to the outside to the *i*-th face, $r_{a,i} = \mathbf{R}_{a,i} \cdot \hat{\mathbf{a}}_i$ and $\mathbf{R}_{a,i}$ is the distance vector of the *i*-th face. It must be noted that following this convention, the values of $r_{a,i}$ are not necessarily positive.

To translate the polyhedron by a quantity *L* along the direction $\hat{\mathbf{d}}_{[hkl]}$, we can apply the transformation:

$$r_{b,i} = r_{a,i} + L \cdot \left(\hat{\mathbf{d}}_{[hkl]} \cdot \hat{\mathbf{b}}_i \right) = r_{a,i} + L \cdot \left(\hat{\mathbf{d}}_{[hkl]} \cdot \hat{\mathbf{a}}_i \right) \qquad (6)$$

with $\hat{\mathbf{b}} \equiv \hat{\mathbf{a}}$.

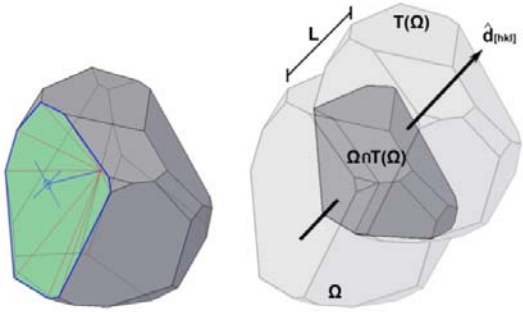

Figure V - 1. Generic polyhedral crystal (left) and its "ghost", i.e., the same crystal shifted by a quantity *L* along $\hat{\mathbf{d}}_{[hkl]}$. The intersection volume (CVF) is highlighted (right).

The translated polyhedral (aka "ghost" (Wilson, 1962)) (cf. Figure (1)) obtained by this translation can be described as:

$$T(\Omega) = \begin{cases} \hat{\mathbf{b}}_1 \cdot \mathbf{P}_k \le r_{b,1} \\ \quad \ldots \\ \hat{\mathbf{b}}_N \cdot \mathbf{P}_k \le r_{b,N} \end{cases} \tag{7}$$

The intersection polyhedron Ψ between Ω and T(Ω) satisfies both systems of inequalities (eq. (5) and (7)):

$$\Psi = \Omega \cap T(\Omega) = \begin{cases} \hat{\mathbf{a}}_1 \cdot \mathbf{P}_k \le r_{a,1} \\ \hat{\mathbf{b}}_1 \cdot \mathbf{P}_k \le r_{b,1} \\ \quad \ldots \\ \hat{\mathbf{a}}_N \cdot \mathbf{P}_k \le r_{a,N} \\ \hat{\mathbf{b}}_N \cdot \mathbf{P}_k \le r_{b,N} \end{cases} \Leftrightarrow \Psi = \begin{cases} \hat{\mathbf{c}}_1 \cdot \mathbf{P}_k \le r_{c,1} \\ \quad \ldots \\ \hat{\mathbf{c}}_{2N} \cdot \mathbf{P}_k \le r_{c,2N} \end{cases} \tag{8}$$

The number of inequalities in eq. (8) can be reduced by excluding those planes parallel or equivalent to each other (redundant inequalities), i.e. by eliminating a plane *i* if it exists already a plane *j* for which $\left(\hat{\mathbf{c}}_i \equiv \hat{\mathbf{c}}_j\right) \wedge \left(r_{c,i} \ge r_{c,j}\right), i \ne j$. This results in the reduced set of $M \le 2N$ inequalities:

$$\Psi = \begin{cases} \hat{\mathbf{f}}_1 \cdot \mathbf{P}_k \le r_{f,1} \\ \quad \ldots \\ \hat{\mathbf{f}}_M \cdot \mathbf{P}_k \le r_{f,M} \end{cases} \tag{9}$$

with *M* being the number of faces of the solid of intersection and $\mathbf{f}_i$ being the normal to the *i*-th face relative to the chosen origin of the reference system. The set of vertices $\mathbf{W}_\Psi$ of this solid is obtained by solving a system of equations for each triplet of planes α, β, γ,

$$\mathbf{W}_{\Psi} = \begin{cases} \hat{\mathbf{f}}_{\alpha} \cdot \mathbf{P}_k = r_{f,\alpha} \\ \hat{\mathbf{f}}_{\beta} \cdot \mathbf{P}_k = r_{f,\beta} \\ \hat{\mathbf{f}}_{\gamma} \cdot \mathbf{P}_k = r_{f,\gamma} \end{cases} \quad \forall \alpha \neq \beta \neq \gamma \tag{10}$$

and by excluding those solutions that do not simultaneously satisfy eq. (8), as they represent points laying outside the common volume. Each triplet of adjacent planes is associated with a corresponding solution of eq. (10): while solving the equations, all planes are recognized and labelled as sides of the intersection polyhedron.

Each face π of Ψ is completely defined by its N_{π} vertices $\mathbf{W}_{\Psi\pi}$. Each of those vertices can be conveniently referred either to the centroid of the solid G or to the centroid of the face $\mathbf{G}_{\pi}$ leading, respectively, to the two representations $\tilde{\mathbf{W}}_{\Psi\pi,k} = \mathbf{W}_{\Psi\pi,k} - \mathbf{G}$ and $\tilde{\mathbf{w}}_{\Psi\pi,k} = \mathbf{W}_{\Psi\pi,k} - \mathbf{G}_{\pi}$ (cf. Figure (1)). The use of those two references allows for a unique ordering of the vertices (e.g. clockwise) with respect to two orthogonal unit vectors $\hat{\mathbf{i}}, \hat{\mathbf{j}}$ in the face π selected as $\hat{\mathbf{i}} \perp \hat{\mathbf{j}}, \hat{\mathbf{i}} \perp \hat{\mathbf{f}}_{\pi}, \hat{\mathbf{j}} \perp \hat{\mathbf{f}}_{\pi}$. In doing that, a factor ϑ is employed to describe the angular position as:

$$\vartheta = \begin{cases} 0 & if \quad \varphi = 0 \quad , \quad \psi > 0 \\ 2 & if \quad \varphi = 0 \quad , \quad \psi < 0 \\ 1 & if \quad \varphi = 0 \quad , \quad \psi = 0 \\ 3 & if \quad \varphi < 0 \quad , \quad \psi = 0 \\ 0 + \varphi / (\varphi + \psi) & if \quad \varphi > 0 \quad , \quad \psi > 0 \\ 2 - \varphi / (\varphi - \psi) & if \quad \varphi > 0 \quad , \quad \psi < 0 \\ 4 - \varphi / (\varphi - \psi) & if \quad \varphi < 0 \quad , \quad \psi > 0 \\ 2 + \varphi / (\varphi + \psi) & if \quad \varphi < 0 \quad , \quad \psi < 0 \end{cases} \tag{11}$$

in terms of the components $\varphi = \hat{\mathbf{i}} \cdot \tilde{\mathbf{w}}_{\Psi\pi,k}$ and $\psi = \hat{\mathbf{j}} \cdot \tilde{\mathbf{w}}_{\Psi\pi,k}$.

The intersection solid Ψ is finally described as the sum of the tetrahedra $\Theta_{\pi,k}$:

$$\Theta_{\pi,k} = \begin{pmatrix} \tilde{W}_{\Psi\pi,k,x} & \tilde{W}_{\Psi\pi,k+1,x} & \tilde{W}_{\Psi\pi,k+2,x} \\ \tilde{W}_{\Psi\pi,k,y} & \tilde{W}_{\Psi\pi,k+1,y} & \tilde{W}_{\Psi\pi,k+2,y} \\ \tilde{W}_{\Psi\pi,k,z} & \tilde{W}_{\Psi\pi,k+1,z} & \tilde{W}_{\Psi\pi,k+2,z} \end{pmatrix} \quad k \in [0 \ldots N_{\pi} - 2] \tag{12}$$

from which the common volume (volume moment m_{000}, (Tuzikov, et al., 2003)) can be obtained as:

$$V_{\Omega,hkl}(L) = \sum\nolimits_{\pi} \sum_{k=1}^{N_{\pi}-2} \frac{\left|\Theta_{\pi,k}\right|}{6} \tag{13}$$

5.3.2 Non-convex polyhedra

Non-convex polyhedra can be suitably represented as the union of convex polyhedra (C_i). The corresponding CVF is obtained by considering all possible intersection volumes between pairs.

The volume of the intersection between C_i and the translated C_j will be identified as $V_{hkl}\left(C_i;C_j,L\right)$; in this way, $V_{hkl}\left(C_i,L\right)=V_{hkl}\left(C_i;C_i,L\right)$ For i≠j, two intersections need to be calculated, as either C_i or C_j can be translated by the given quantity L along $\hat{\mathbf{d}}_{[hkl]}$ while the other one remain fixed (see Figure 2).

A special class of non-convex polyhedra are those presenting internal holes. Hollow shapes are described as the union of full regions (given a weight +1) with empty ones (given a weight -1). When computing the intersection volumes as described before, weights are arithmetically multiplied, so that the intersection between two empty regions gives a positive contribution to the overall CVF. Formal definitions are reported in Appendix V.A, whereas Figure (2) illustrates the concept with an example.

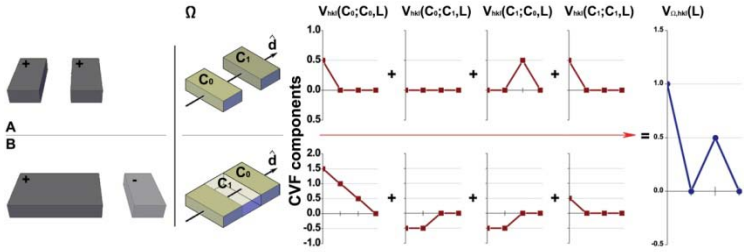

Figure V - 2. CVF for non-convex hollow shapes. The same object can be imagined as either the sum of convex objects (A) or as the difference between convex objects and convex holes (B). See text and Appendix V.A for details.

5.4 Examples of application

The proposed algorithm is completely general and can be used to calculate the CVF and the corresponding peak profile for materials of any crystal symmetry and for domains of any shape, irrespective of geometrical complexity and number of faces. In the following, the application to some significant cases of study is illustrated, considering the two broad categories of convex and non-convex bodies. For simplicity, all examples will refer to the ideal face-centred cubic (*fcc*) structure of gold, so that the CVF and the corresponding powder pattern peak profiles are the sum of the CVFs for all crystallographically-equivalent directions.

5.4.1 Convex shapes

5.4.1.1 Truncated and bitruncated cube

Cube and octahedron, for which an analytical expression of the CVF is available ((Stokes, et al., 1942), (Scardi, et al., 2004(a))), are end members of a family of polyhedra that can be obtained by applying the truncation and bitruncation operations to the cube. The family includes the cuboctahedron as rectified intermediate (when truncation is such that the edges of the cube collapse into points).

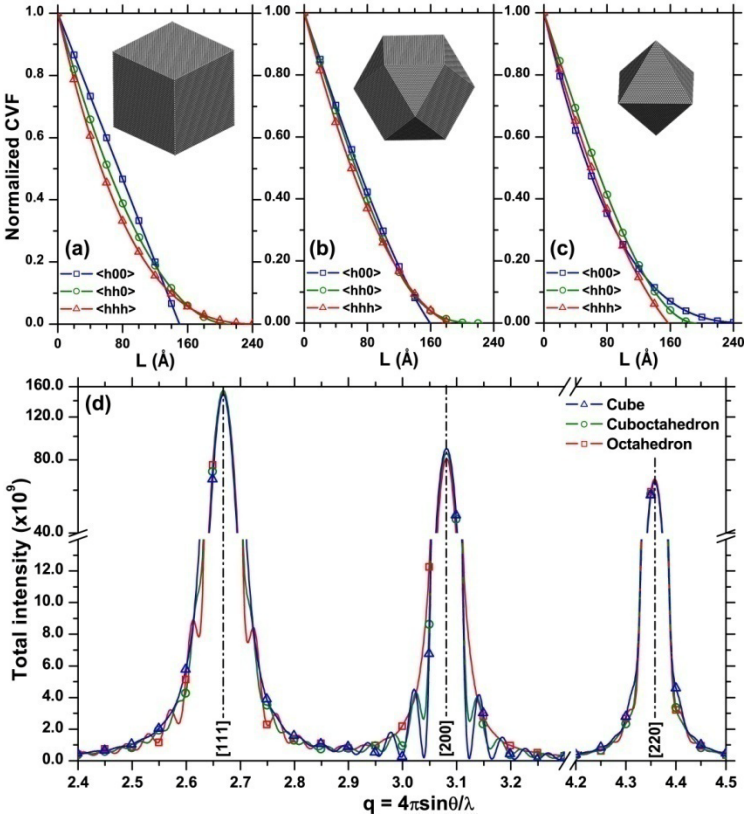

Figure V - 3. Examples of CVF for cube (a), cuboctahedron (b), octahedron (c). The corresponding powder patterns obtained from eq. (1) are shown (c).

Beyond the mathematical description, those polyhedra are similar to particular cases of the Equilibrium Crystal Shape (ECS) obtained with the Wulff construction

(Groth, 1901), frequently observed e.g. in cubic-lattice nano-crystals grown under thermodynamic control (see e.g. (Vitos, et al., 1998), (Xia, et al., 2008), (Wang, et al., 2003) and references therein). For this reason, in the literature they are frequently called Wulff polyhedral (Baletto, et al., 2000).

From a crystallographic point of view, the actual polyhedra can be obtained by progressively cutting the corners of a cube (bounded by {100} faces) with {111} planes that ultimately become the faces of the octahedra.

The normalized CVF (i.e. $A_{hkl}^{S}(L)$) for three crystallographic directions of cube, octahedron and cuboctahedron are shown as an example in Figure (3) together with a set of corresponding powder diffraction peak profiles. For a more convenient comparison, nano-crystals of equal volume were chosen.

The peak profiles show quite distinctive differences. Most notably, interference fringes appear on the {200} peak for cubic crystallites and on the {111} peak for octahedral ones, as a result of the different sets of parallel planes bounding the crystalline domains. The results for cube and octahedron are identical (within the limits of numerical precision) with those obtained from the corresponding analytical CVF expressions provided by (Stokes, et al., 1942).

5.4.1.2 Irregular domain shapes: 3D Voronoi cell

The proposed algorithm is particularly useful to calculate CVF and peak profiles for crystals with irregular shapes, like the crystalline domains usually observed in polycrystalline aggregates. One such crystallite can be obtained e.g. by filling with atoms a 3D Voronoi cell (Figure (4)). In this case the orientation of the crystal lattice with respect to the nano-crystal must be specified, and crystallographically equivalent [hkl]s do not generally give the same CVF. This is shown in Figure (4) for the [h00] directions, whose normalized CVFs are compared with that for the equivalent-volume sphere, to emphasize the effect of an irregular shape (sphericity (Wadell, 1935) $\Psi = 0.87$).

In this case, as there is no analytical expression for the CVF to compare with, it is interesting to study the difference between the pattern obtained with the proposed Fourier method and that obtained using the Debye scattering equation ((Debye, 1915), (Warren, 1969), (Gelisio, et al., 2010)):

$$I(q) \propto \sum_{i}^{N} \sum_{j}^{N} \frac{\sin\left(\mathbf{r}_{ij} \cdot \mathbf{q}\right)}{\mathbf{r}_{ij} \cdot \mathbf{q}} \tag{14}$$

where r_{ij} is the distance between the pair of atoms *i* and *j*.

The small but visible differences are due to two basic reasons: the first one is that the Debye scattering equation refers to an atomistic model of the nano-crystal, which is different from a purely geometrical polyhedron. As shown by Ino and Minami (Ino, et al., 1979), eq. (1) provides an average peak profile obtained from all possible

ways to fill the same volume with the lattice, whereas the Debye scattering equation is obtained for just one of such atomistic models. The second difference is to be attributed to the use in eq. (1) of the already mentioned TPA. The smaller the crystallite size, the more the TPA approach becomes an approximation for the real case; here (diameter of the equivalent-volume sphere of 13.2 nm) the introduction of the TPA should give just a minor discrepancy. As already pointed out, if a higher precision is necessary, the approximation can be avoided by replacing eq. (1) with a more rigorous expression (see e.g. (Ino, et al., 1979), (Beyerlein, et al., 2011) for details).

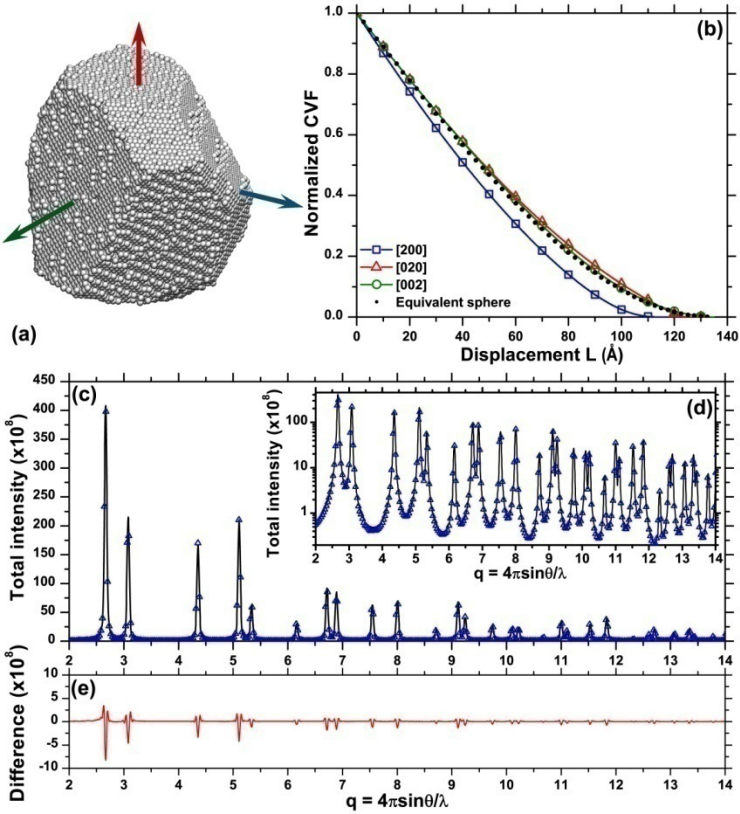

Figure V - 4. Irregular nano-crystal shape from a 3D Voronoi cell (a). The CVF is shown for the [h00] directions and for the equivalent-volume sphere (b). The powder pattern obtained from eq. (1) (dot) is compared with that calculated by the Debye equation (line) (c, d). The difference is shown below (e).

5.4.1.3 *Polycrystalline microstructure: 3D Poisson-Voronoi microstructure*

It is interesting to extend the previous analysis to a polycrystalline microstructure, e.g., to a cluster of irregularly-shaped crystallites made by Poisson-Voronoi space tessellation, from which the grain of the previous example was taken. The powder pattern is obtained by adding up the peak profiles corresponding to each and all grains in the cluster, as schematically shown for two reflections in Figure (5).

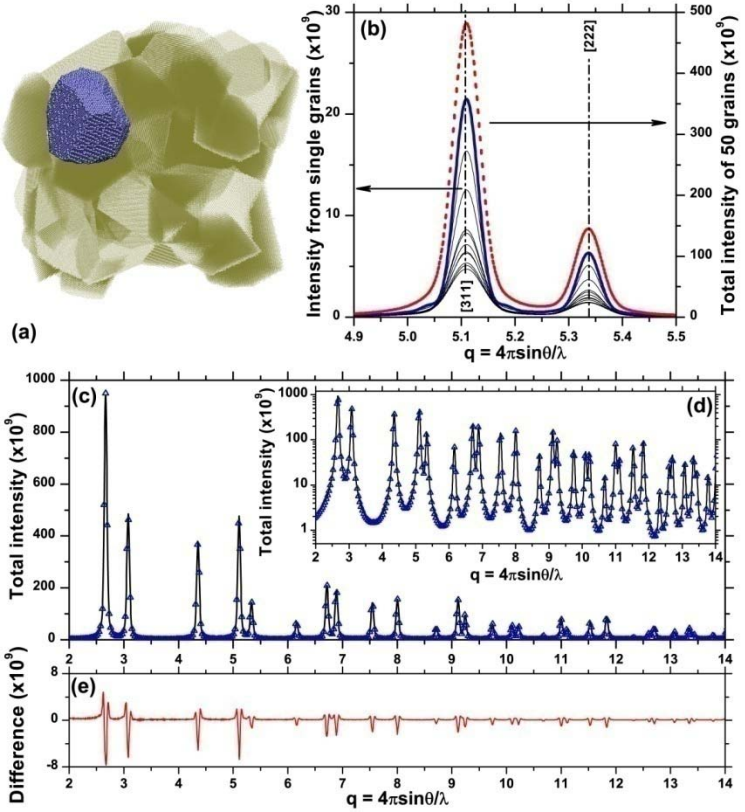

Figure V - 5. Nano-polycrystalline microstructure obtained by 3D Poisson-Voronoi tessellation (a), with detail of the (311) and (222) line profiles: thick line refers to the grain of Figure (4), thin lines to all other grains and dots to the whole cluster (b). A comparison between the powder pattern from the CVF approach (dot) and from the Debye scattering equation (line) is proposed in (c, d); the difference is shown below (e).

Also in this case, it is possible to compare the resulting powder pattern with the corresponding one obtained by means of Debye scattering equation (cf. Figure

(5c)). Differences are much smaller (by about one order of magnitude) than those observed for the single grain of Figure (4). This is not so obvious as the differences discussed before are also present here, and even more so considering that the Debye equation, when applied to the entire cluster, includes interference effects between all different grains, an effect clearly not considered by the CVF approach. However, this "cross-correltion" contribution is negligible as the crystalline domains are randomly oriented and spaced. Reason for the better match between the Fourier-based CVF approach (eq. (1)) and the Debye scattering equation (eq. (14)) is the Ino-Minami average (Ino, et al., 1979). Even if the grains in the cluster have different shapes, adding up all patterns has a similar effect as considering different space fillings with atoms. This feature should be more and more evident the larger the cluster size, so we can safely conclude that the CVF approach is appropriate to describe real materials even if made of relatively small domains. Further differences between an atomistic description of crystalline domains and the CVF approach are discussed by (Beyerlein, et al., 2011).

Modelling of the pattern using spheres, albeit being clearly incompatible with the *a priori* information, does not lead to a satisfactory fit. Computational materials science is a field where the accurate knowledge of the microstructure and the possibility of performing virtual experiments is the key for a real scientific advancement. The possibility of calculating the diffraction pattern for a given domain in a cluster, following a Bragg-type approach (peak by peak), paves the way to testing microstructural models and analysing the microstructure evolution. To understand e.g. the strain broadening contribution (which is the key to several of the enhanced properties of a nano-structured material), we can equilibrate the cluster proposed here at a given temperature and simulate the corresponding pattern using the Debye scattering equation. The analysis of the corresponding pattern can be easily done using the WPPM; considering an average shape, we can easily miss the subtle differences in the strain broadening contribution.

5.4.2 Non-convex shapes

5.4.2.1 Planar tripods and tetrapods

A remarkable example of non-convex shapes is provided by branched metallic nano-crystals (Chen, et al., 2003). Single-crystal planar tripod- and tetrapod-shaped Au nano-crystals with specific directions for the protruding "legs" (pods) can be synthesised via soft chemistry (Chen, et al., 2003): tripods lie flat on a (111) plane with three pods along $[1\bar{1}0]$, $[\bar{1}01]$ and $[0\bar{1}1]$, whereas tetrapods show four pods extending along the $[1\bar{1}0]$, $[\bar{1}\bar{1}0]$, $[\bar{1}10]$, $[110]$ directions from a [001] oriented body. CVFs and powder patterns were produced according to the procedure described above for non-convex shapes: the results are shown in Figure (6). The

differences between the powder patterns of tripods and tetrapods (i.e., between three and four legs), are not as large as those given by a different length of the legs. Especially for the tripods, longer pods give increasingly sharper {110} peak profiles.

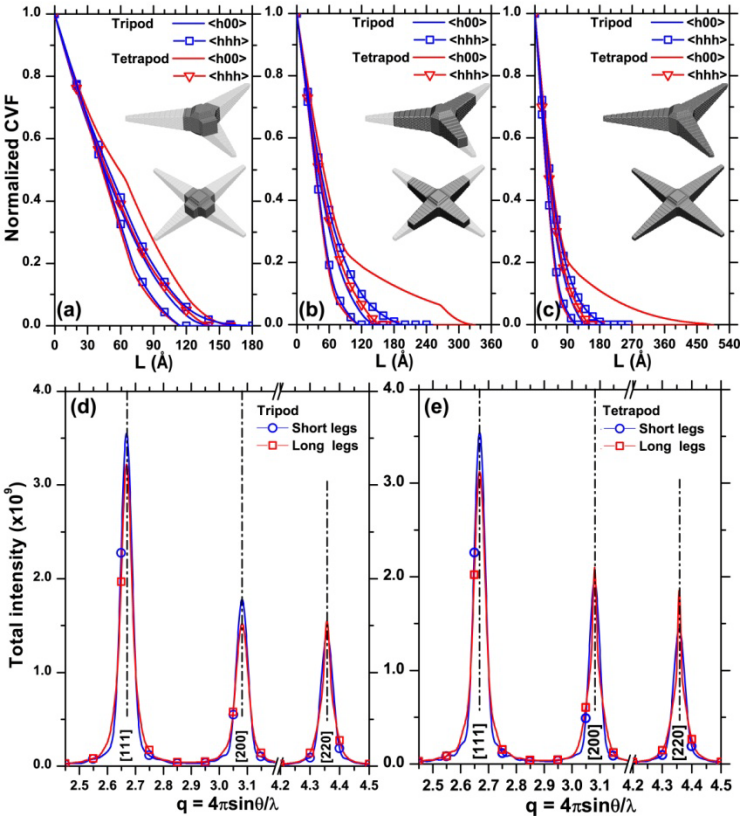

Figure V - 6. Normalized CVF (a, b, c) and powder diffraction patterns for gold tripod (d) and tetrapods (e) along three crystallographic directions. Both short and long legged nano-particles are considered.

As a general consideration, particularly appropriate in the context of the present example, it is worth considering that powder diffraction's forte is not so much in the predictive power (e.g., guessing the shape of nano-particles) but in the statistical reliability of the result, guaranteed by the large number of scattering domains in a typical specimen. Only a combination of independent information can give qualitatively and quantitatively reliable results. Therefore LPA performs at his best when complemented with additional independent information gathered by other techniques (for instance electron microscopy), providing e.g. evidence on the most

frequent shape and thus supporting the modelling and interpretation of the powder patterns.

5.4.2.2 Hollow cubes

Hollow crystallites are a further example of non-convex shapes: hollow nano-spheres and “nano-boxes” (i.e., hollow cubes) are rather common, but many other shapes broadly termed “nano-cages” are nowadays produced (Lou, et al., 2008). As an example (see Figure (7)), we consider here the effect of creating, respectively, a cubic, a cuboctahedral and an octahedral void of the same volume inside a cubic crystallite. In Figure (7), normalized CVFs are shown for the same three crystallographic directions as in Figure (3) together with the corresponding powder diffraction peak profiles.

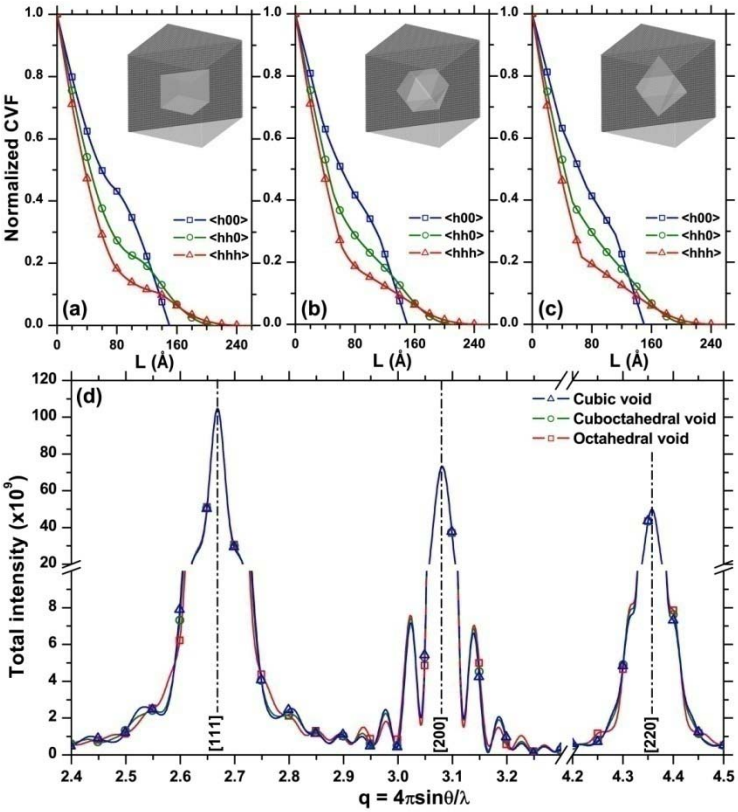

Figure V - 7. Normalized CVF (a, b, c) and selected peak profiles (d) for cubic crystals with voids of equal volume but different shape. See text for details.

As the crystalline part is relatively thick, differences are not so remarkable. A much more visible effect is produced by changing the size of the void. This is shown in Figure (8), where a cube-shaped void of increasing size is produced inside the same cube-shaped nano-crystal. The normalized CVF for the three directions (<h00>, <hh0>, <hhh>) is now clearly different, and depends on the wall thickness of the hollow shape. The effect is so remarkable that the CVF along <h00> has a non-monotonous decay for a thickness $\tau > \frac{D_{cube}}{2} - \frac{D_{cube}}{2\sqrt{2}}$. The corresponding powder diffraction peak profiles (Figure (8)) show quite visible differences, thus confirming that the line profile is rather sensitive to the thickness of the walls (i.e., the size of the void region) more than to the shape of the empty volume.

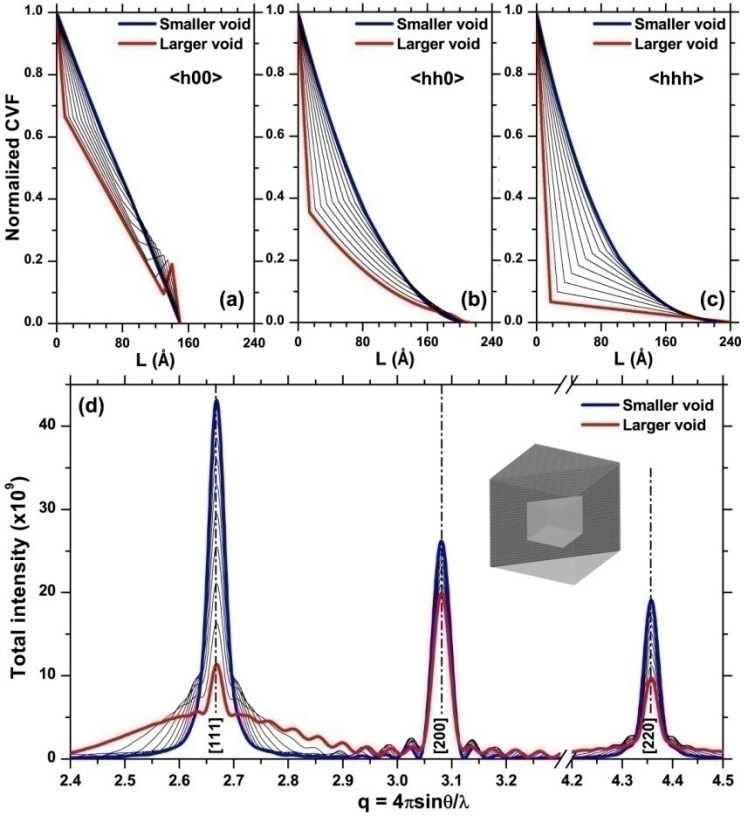

Figure V - 8. Normalized CVF for a hollow cube with a cube-shape void of increasing size (a, b, c). Data and corresponding profiles are presented for three crystallographic directions (<h00>, <hh0>, <hhh>). The profiles are proposed for cubes with increasingly large size of the void (d).

5.4.3 Non-polyhedral shapes

Non-polyhedral shapes (e.g. shapes presenting curved surfaces) can be approximated by polyhedra with a suitably large number of (planar) faces. The sphere, showing no planar faces, represents perhaps a limiting case here. Moreover, the effects of the non-planarity are enhanced in the case of hollow nano-particles. From a physical point of view, this polyhedral description can appear more suitable than the continuous one for the description of a real object, as it better deals with the atomistic nature of the domains.

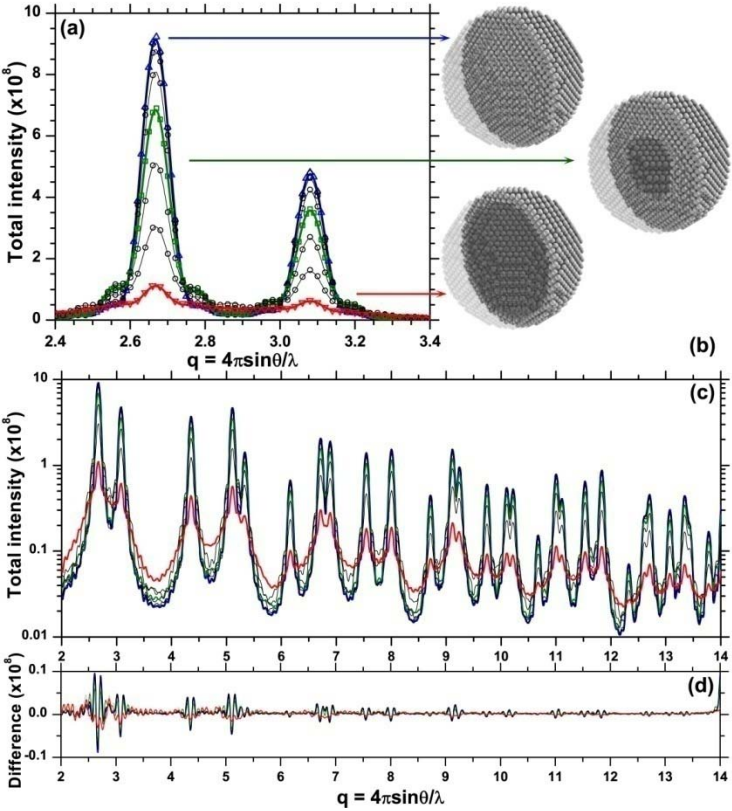

Figure V - 9. The X-ray powder diffraction patterns of a set of hollow spheres (b) from approximated CVF (dot) and from the Debye scattering equation (line) are compared (a); the solid wide angle patterns (c) and the corresponding differences (d) are provided below.

To compute the CVFs for a hollow spherical domain, the shape of the particles was approximated by a polyhedron with 74 faces, uniformly oriented in space. The CVF along the [100] direction was employed to model the pattern via FT. In Figure

(9), the X-ray powder diffraction patterns of a set of hollow spheres simulated by the Debye scattering equation and modelled by the cosine FT are compared. The goodness of the suggested approximation is supported by the agreement of the pattern modelled by FT with the “true” pattern simulated via Debye scattering equation. Finally, the evolution of the powder patterns from solid sphere to hollow sphere with thin wall confirms the results of hollow cubic particles.

5.5 Conclusions

A new numerical algorithm has been presented for the fast computing of the Common Volume Function of any given convex or non-convex polyhedron. This allows the calculation and/or interpretation of the diffraction pattern for the corresponding powder both directly or within the wider frame of the Whole Powder Pattern Modelling. The patterns agree with those obtained by means of the Debye scattering equation.

It might be underlined that non-crystallographic shapes such as, e.g. decahedra or icosahedra, were not considered here: in fact, beyond the geometric description (in principle always possible), non-crystallographic nano-particles violate the translational symmetry. Moreover, those particles are usually affected by strong strains like the ones due to twins in decahedra/icosahedra. These specific conditions limit the applicability of the CVF concept, unless due consideration is given to the real equilibrium shape and atomic positions.

5.6 Appendix V.A: Common Volume Function in the frame of set theory

Any portion of space Ω in $\mathbb{R}^3$ can be described by set theory using the Dirac measure (cf. Figure (1) for an example in $\mathbb{R}^3$):

$$\delta_{\Omega}(\mathbf{P}_k)=\begin{cases}1 & \mathbf{P}_k \in \Omega \\ 0 & \mathbf{P}_k \notin \Omega\end{cases} \qquad (15)$$

$$\delta_{T(\Omega)}(\mathbf{P}_k)=\begin{cases}1 & \mathbf{P}_k \in T(\Omega) \\ 0 & \mathbf{P}_k \notin T(\Omega)\end{cases}$$

where T(Ω) is the portion of space equivalent to Ω after a finite translation along the direction $\hat{\mathbf{d}}_{[hkl]}$.

The portion of space common to Ω and T(Ω) (intersection polytope) is then described by the following relation:

$$\delta_{\Omega\cap T(\Omega)}(\mathbf{P}_k)=\delta_{\Omega}(\mathbf{P}_k)\cdot\delta_{T(\Omega)}(\mathbf{P}_k) \qquad (16)$$

Beyond convex geometry, any set Ω can be described as the union of one or more subsets (cf. Figure (2), upper part, for an example in $\mathbb{R}^3$):

$$\delta_{\Omega}(\mathbf{P}_k)=\delta_{C_0\cup C_1}(\mathbf{P}_k)=\delta_{C_0}(\mathbf{P}_k)+\delta_{C_1}(\mathbf{P}_k) \qquad (17)$$

Without losing in generality, we can consider the case where the subsets composing Ω are non intersecting (i.e. $C_0\cap C_1=\varnothing$). Under those hypotheses, the intersection between object and ghost (eq. (A2)) can be calculated as:

$$\begin{aligned}\delta_{\Omega\cap T(\Omega)}(\mathbf{P}_k)&=\left[\delta_{C_0}(\mathbf{P}_k)+\delta_{C_1}(\mathbf{P}_k)\right]\cdot\left[\delta_{T(C_0)}(\mathbf{P}_k)+\delta_{T(C_1)}(\mathbf{P}_k)\right]\\&=\left[\delta_{C_0}(\mathbf{P}_k)\cdot\delta_{T(C_0)}(\mathbf{P}_k)\right]+\left[\delta_{C_0}(\mathbf{P}_k)\cdot\delta_{T(C_1)}(\mathbf{P}_k)\right]\\&\quad+\left[\delta_{C_1}(\mathbf{P}_k)\cdot\delta_{T(C_0)}(\mathbf{P}_k)\right]+\left[\delta_{C_1}(\mathbf{P}_k)\cdot\delta_{T(C_1)}(\mathbf{P}_k)\right]\end{aligned} \qquad (18)$$

Hollow shapes are better described using a difference of subsets (cf. Figure (2), lower part, for an example in $\mathbb{R}^3$):

$$\delta_{\Omega}(\mathbf{P}_k)=\delta_{C_0\setminus C_1}(\mathbf{P}_k)=\delta_{C_0}(\mathbf{P}_k)-\delta_{C_1}(\mathbf{P}_k) \quad \text{where} \quad C_0\supseteq C_1 \qquad (19)$$

Once again, eq. (16) can be expanded as follows:

$$\begin{aligned}\delta_{\Omega\cap T(\Omega)}(\mathbf{P}_k)&=+\left[\delta_{C_0}(\mathbf{P}_k)-\delta_{C_1}(\mathbf{P}_k)\right]\cdot\left[\delta_{T(C_0)}(\mathbf{P}_k)-\delta_{T(C_1)}(\mathbf{P}_k)\right]\\&=+\left[\delta_{C_0}(\mathbf{P}_k)\cdot\delta_{T(C_0)}(\mathbf{P}_k)\right]+\left[\delta_{C_0}(\mathbf{P}_k)\cdot\left(-\delta_{T(C_1)}(\mathbf{P}_k)\right)\right]\\&\quad+\left[\left(-\delta_{C_1}(\mathbf{P}_k)\right)\cdot\delta_{T(C_0)}(\mathbf{P}_k)\right]+\left[\delta_{C_1}(\mathbf{P}_k)\cdot\delta_{T(C_1)}(\mathbf{P}_k)\right]\end{aligned} \qquad (20)$$

The CVF is the volume of the intersection. Due to the convention introduced in section 5.3.2 that assigns a negative weight to the voids, eq. (18) and (19) assume the same functional form and the CVF can be always calculated as:

$$\begin{aligned} V_{\Omega,hkl}(L) &= \int_{\mathbb{R}^n} \delta_{\Omega \cap T(\Omega)}(\mathbf{P}_k) \\ &= V_{hkl}(C_0;C_0,L) + V_{hkl}(C_0;C_1,L) + V_{hkl}(C_1;C_0,L) + V_{hkl}(C_1;C_1,L) \\ &= V_{C_0,hkl}(L) + V_{hkl}(C_0;C_1,L) + V_{hkl}(C_1;C_0,L) + V_{C_1,hkl}(L) \end{aligned} \tag{21}$$

where $V_{hkl}(C_i;C_j,L)$ is the volume of the intersection between C_i and $T(C_j)$. From this definition, it follows e.g. that $V_{\Omega,hkl}(L) = V_{hkl}(\Omega;\Omega,L)$.

Chapter VI

Directional - Pair Distribution Function

Part of this chapter has been published in:

Alberto Leonardi, Matteo Leoni, Paolo Scardi,

"Atomistic interpretation of microstrain in diffraction line profile analysis",
Thin Solid Films,(2012) in press.

Alberto Leonardi, Matteo Leoni, Paolo Scardi,

"Directional Pair Distribution Function for diffraction Line Profile Analysis of atomistic models",
Journal of applied Crystallography, (2012) submitted.

6.1 Abstract

The concept of Directional - Pair Distribution Function is proposed to describe line broadening effects in powder patterns from atomistic models of nano-polycrystalline microstructures. The approach provides at the same time a description of the size effect for domains of any shape, and a detailed explanation of the strain effect caused by the local atomic displacements. The latter is discussed in terms of different strain types, also accounting for the anisotropy of the strain field and the effects of the grain boundary. Results can also be directly read in terms of traditional Line Profile Analysis, like that based on the Warren-Averbach method.

6.2 Introduction

Considerable efforts in the study of nano-materials focus on the visualization of strain at the atomic level, but even the most advanced experimental methods based on coherent diffraction confine to single, isolated nanoparticles and relatively weak strain fields ((Thomas, 2008), (Robinson, et al., 2009), (Watari, et al., 2011)). Strains in nano-polycrystalline microstructures are still a challenge to direct visualization techniques, for the variety of strain sources, level and complexity of their distribution. In this context diffraction Line Profile Analysis (LPA), although indirect and much less detailed than coherent diffraction and other microscopies, is still one of the most convenient and used experimental techniques. Further insights in the mechanisms and distribution of strains can be produced by atomistic models, in particular by Molecular Dynamics (MD) simulations ((Van Swygenhoven, et al., 2000), (Van Swygenhoven, 2002), (Derlet, et al., 2005), (Derlet, et al., 2006), (Cao, et al., 2008), (Stukowski, et al., 2009)). This has been shown by a number of recent papers, but so far the connection with diffraction LPA was discussed in terms of simplified integral breadth methods only ((Derlet, et al., 2005), (Leonardi, et al., 2011)): the potential of joining MD simulations and state of the art LPA is still largely unexplored.

In the past decade LPA evolved in the direction of Fourier methods based on physical models of the microstructure (Mittemeijer, et al., 2004). Despite the success in many applications, even the most advanced methods of Whole Powder Pattern Modelling (WPPM) ((Scardi, et al., 2004(a)), (Scardi, et al., 2002)) still rely on simplified descriptions of the lattice defects, and cannot be proved to be univocal in the identification and quantification of the different effects contributing to the line profiles. For example, the uniqueness of the anisotropic line broadening caused by the strain field of dislocations is an open question, as well as the effects of grain to grain deformation fields and the role of grain boundaries. It is not clear to what extent these different sources of lattice deformation can be distinguished by even the most advanced LPA methods.

MD simulations of nano-polycrystalline microstructures can give useful insights in these problems, provided that the usual concept of strain is reconsidered, to be related in a more direct way to diffraction LPA. Inhomogeneous strains have a peculiar effect on diffraction, which is sensitive to the distribution of the strain component projected along the scattering vector direction; such strain component needs then to be considered as a function of the separation distance between all possible couples of atoms (or unit cells, on a coarser size scale) in each given crystalline domain (Warren, 1990).

As shown by several MD works, the Debye Scattering Equation (DSE) is the most direct way to simulate the powder diffraction pattern from a given atomistic model of nano-polycrystalline microstructure ((Derlet, et al., 2005), (Cervellino, et al., 2003), (Cervellino, et al., 2010), (Gelisio, et al., 2010), (Gelisio, et al., 2011)), as

it just requires atomic positions (strictly speaking, distances between all possible couples of atoms), with no assumption on the crystal structure or on the presence of lattice defects. While the DSE is so rigorous and appealing for simulating the powder pattern, it is not so useful to analyse the effects of atomic level strain, to separate different sources of line broadening and to study anisotropy effects which make line broadening different for line profiles with different Miller indices (hkl).

In the present work we introduce the concept of Directional - Pair Distribution Function (D-PDF) to represent the finite size and shape of coherently scattering domains (crystallites) and the local atomic displacement in a way directly readable in terms of diffraction effects. The D-PDF allows a separation of all contributing (hkl) line profiles in the powder diffraction pattern from an atomistic simulation of single crystals as well as of nano-polycrystalline microstructures. Each line profile can be described in terms of the crystallite size and strain contributions, in a quite similar way as traditional LPA based on Fourier analysis (e.g., the Warren-Averbach (WA) method ((Warren, et al., 1950), (Warren, et al., 1952), (Warren, 1990))). The proposed approach has at least two valuable applications: (i) to validate different LPA methods and better understand their results; (ii) to study MD simulations and their relation with real microstructures in terms of a well-known, easy to perform experimental technique like diffraction.

The case of study presented in this work concerns a metallic nano-polycrystalline system made of randomly oriented grains with irregular, though not far from equiaxed, shapes. The system was equilibrated (energy minimized and thermalized) by conventional MD based on the Embedded Atom Method (EAM) (Daw, et al., 1983), so that no lattice defects other than the grain boundaries are present. Under these conditions, besides the effect of the finite size (and shape) of the grains, inter-granular strains due to the equilibration process should be the only microstructural effects affecting the line profiles. Detailed information on the direction-dependent strain field and its effect on the simulated powder diffraction pattern can be obtained by means of the D-PDF concept. The role of the grain boundaries is also discussed.

6.3 Copper nano-polycrystalline microstructure: generation and strain distribution

A cubic box (side length 260.28 Å) was divided into 50 cells by a recently developed algorithm of Constrained Modified Voronoi Tessellation (CMVT) ((Gross, et al., 2002), (Xu, et al., 2009), (Suzudo, et al., 2009), (Leonardi, et al., 2012(d)), (Leonardi, et al., 2013)). The CMVT allows control of different properties during the generation of the cells. In the present case, CMVT parameters were set to produce high sphericity (arithmetic mean $\psi = 0.800122$) and a lognormal distribution of grain sizes

(arithmetic mean 82.6 Å, standard deviation 21.4 Å); grains were then filled with about 1.5 million Cu atoms, using a unit cell parameter of 3.615 Å (Figure (1)).

Equilibration of the starting ("crystallographic") system was made by EAM, using the Cu potential by Foiles, Baskes and Daw (Foiles, et al., 1986). After the energy minimization, an isothermal-isobaric time integration process (NPT) at 100K was performed by the LAMMPS software (Plimpton, 1995), reaching equilibrium conditions. The latter were assessed by comparing the deformation field after 1.2 and 2.4 ns of equilibration times, in terms of both isotropic (volumetric) and anisotropic (deviatoric) strain components (Figure (2)). The zero strain is referred to an equivalent unit cell of $\sqrt[3]{B_{boxside}^3 / \left(N_{atoms} / 4 \right)}$, where $B_{boxside}$ is the equilibrated box side length.

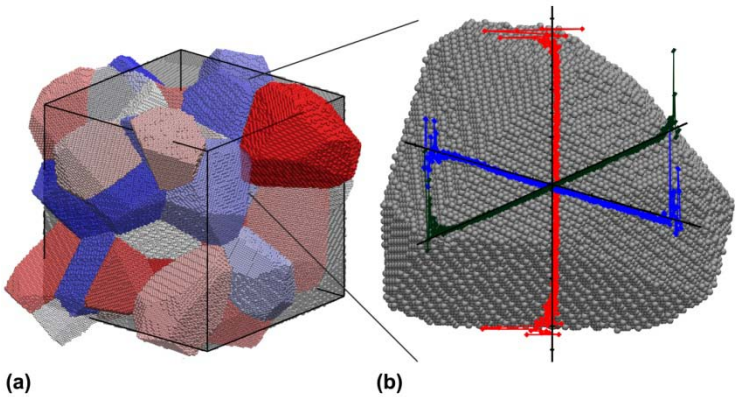

Figure VI - 1. Copper nano-polycrystalline microstructure after reconstruction of grains cut across by the PBCs (a). Example of volumetric strain along the <h00> directions in a grain (b).

While the Molecular Dynamics was made on a box with Periodic Boundary Conditions (PBCs), grains cut across by the cube faces were joined, so to create a more plausible system (Figure (1a)) for the simulation of the powder diffraction pattern by the DSE.

As shown schematically in Figure (1b), strain is not constant across the grains: a steep gradient is observed in the outer layers, extending from the grain boundary region inward for about 10 Å. This trend, qualitatively the same for all grains in the cluster, is shown in Figure (2): here the mean isotropic strain in each grain is plotted against the distance from the grain boundary.

While the strain decreases to a small constant value in the core region, the value reached by the isotropic component inside grains depends on the grain size. This feature is visible in Figure (2), but it can more clearly be seen in the inset, where the average of the type II strain of each grain is plotted as a function of the diameter of the equivalent-volume sphere. Larger grains put in tension the smaller ones, with

an apparently non-linear trend. A wider discussion on such features is provided in chapter III (Leonardi, et al., 2012(c)). In Figure (3) it is also possible to see the anisotropy of this deformation, which is higher along [h00] than along [hhh], respectively corresponding to the elastically softer and stiffer directions in copper.

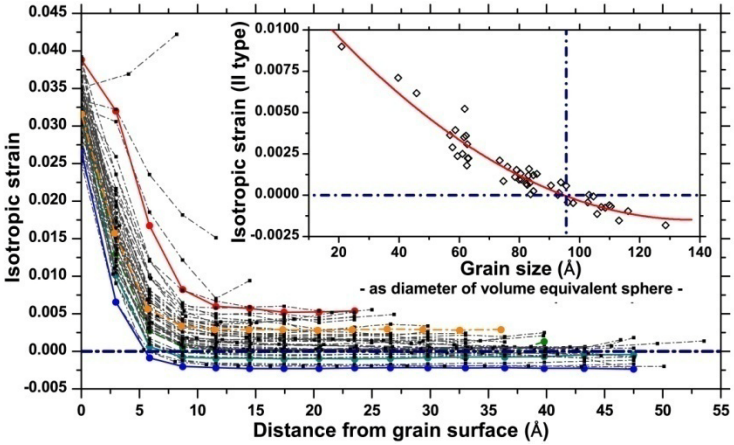

Figure VI - 2. Average isotropic strain as a function of the position from the grain surface for the different grains in the cluster. The inset shows the II type isotropic strain as a function of the diameter of the equivalent volume sphere (see text for details).

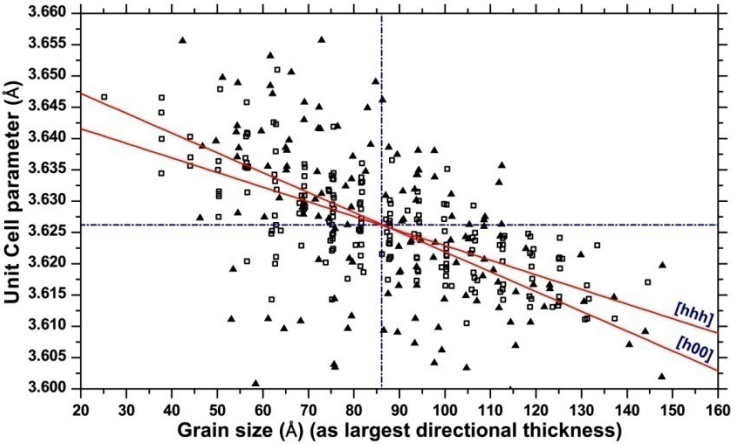

Figure VI - 3. Unit cell parameter as a function of the largest thickness along the direction considered. See text for details. Dash lines represent the average values.

6.3.1 Directional - Pair Distribution Function (D-PDF)

The D-PDF is a convenient concept to represent strain effects on the diffraction line profiles. It is obtained by counting the number of atom pairs for each distance *L* along the [hkl] direction of the scattering vector in a given grain of the cluster. As shown in Figure (4), it is the projection along [hkl] of the atom-atom displacement ΔL which is considered: the D-PDF in then made of a series of histogram distributions, centred on the mean distance between n-*th* neighbour atoms, ranging from the closest neighbour to the longest distance in the grain along [hkl]. Each distribution $p_L\left(\Delta L_{hkl}\right)$ can be calculated as said above, along [hkl] of a given grain, or be averaged over all crystallographically equivalent <hkl> directions in the grain, or be averaged over all equivalent directions of all grains in the cluster (so called Super D-PDF).

It is important to note that the D-PDF along [hkl] directions belonging to the same <hkl> family, even if crystallographically equivalent, are in general different, because the strain field caused by the neighbouring grains is not subject to any symmetry restrictions. These differences, however, tend to disappear in the average for a given grain or for the entire cluster.

As an example, Figure (4a) shows the D-PDF along the [h00] direction of grain #33 in the cluster, with one such distribution shown in detail in Figure (4b). The trend of the normalised area of the $p_L\left(\Delta L_{h00}\right)$ as a function of the pair distance is shown in Figure (4c). This quantity is equivalent to the Common Volume Function (CVF), as introduced by Stokes and Wilson (Stokes, et al., 1944), representing the intersection volume between a crystalline domain and its "ghost", i.e., the same domain shifted a distance *L* along [hkl] (inset of Figure (4c)). As shown by several authors ((Warren, 1990), (Wilson, 1962), (Guinier, 1963)), within reasonable approximations the Fourier Transform (FT) of the CVF gives the so-called size component of the diffraction line profile, due to the finite size of the crystalline domain along the given [hkl]. As the D-PDF is not normalized, the corresponding diffraction line profile obtained by FT includes the appropriate weight (volume or number of atoms) for the given grain.

The D-PDF concept allows for a simple and reliable way to separate the effects of domain size/shape from those due to lattice defects and microstructural features in general. While the $p_L\left(\Delta L_{hkl}\right)$ area is related to the domain size/shape component of the line profile, width and shape of the D-PDF provide a detailed description of the atomic displacement over different distances.

As shown below, this is the same representation of strain effects on line profiles as that used by traditional LPA based on Fourier analysis, like the WA method ((Warren, et al., 1950), (Warren, et al., 1952), (Warren, 1955), (Warren,

1959)) and methods proposed by Stokes and Wilson ((Stokes, et al., 1944), (Eastabrook, et al., 1952)).

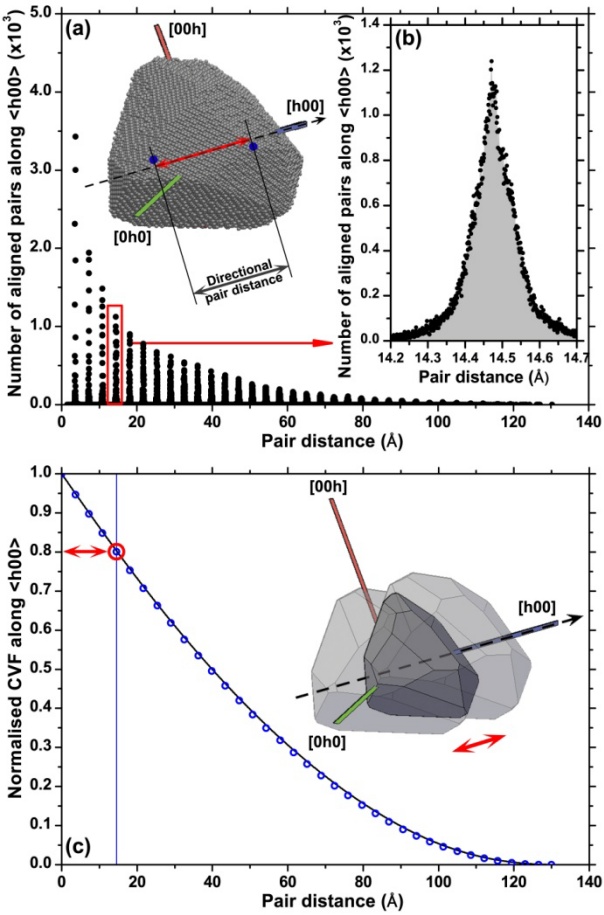

Figure VI - 4. Directional - Pair Distribution Function for grain #33 in the cluster along the [h00] direction (a); example of distribution for *L*=14.485 Å(b), whose area corresponds to the circled value of normalized Common Volume Function (CVF) in (c). The inset in (c) illustrates the concept of "ghost" (see text for details).

It is convenient to introduce the strain over a distance *L* along the [hkl] direction, $\varepsilon_{hkl}(L) \equiv \Delta L_{hkl}/L$, and the wavevector transfer modulus, $q = 4\pi \sin\theta/\lambda$. As originally shown by Stokes and Wilson under quite reasonable

approximations ((Stokes, et al., 1944), (Wilson, 1962)), the FT of the peak profile component due to the local atomic strain, $Y_{hkl}^{D}\left(L\right)$, can be written as:

$$\begin{aligned} Y_{hkl}^{D}\left(L\right) &= \left\langle \exp\left[iqL\varepsilon_{hkl}\left(L\right)\right]\right\rangle \\ &= A_{hkl}^{D}\left(L\right) + iB_{hkl}^{D}\left(L\right) \\ &= \int \exp\left[iqL\varepsilon_{hkl}\left(L\right)\right] p_{L}\left(\varepsilon_{hkl}\right) d\varepsilon_{hkl} \end{aligned} \tag{1}$$

where a $\left|\mathbf{F}\right|^{2}$ term (related to the structure factor, *F*) was omitted for simplicity. As shown by the right side of eq. (1), $Y_{hkl}^{D}\left(L\right)$ is the Fourier transform of the D-PDF, which is a complex quantity unless the D-PDF is symmetrical. In eq. (1) the D-PDF was written for strain, which is straightforward considering that $p_{L}\left(\varepsilon\right)d\varepsilon = p_{L}\left(\Delta L\right)L^{-1}d\Delta L$.

The normalization used in eq. (1) is such that $Y_{hkl}^{D}\left(0\right)=1$, so it is convenient to represent the CVF in normalized form too:

$$A_{hkl}^{S}\left(L\right) = N_{hkl}\left(L\right)/N\left(0\right) = V_{hkl}\left(L\right)/V_{grain} \tag{2}$$

where $N_{hkl}\left(L\right)$ is the number of atom couples at distance *L* along [hkl], and $N\left(0\right)$ is the total number of atoms in a given grain; correspondingly, $V_{hkl}\left(L\right)$ is the CVF along [hkl], and V_{grain} the volume of the given grain. It is worth noting here that the present description in terms of D-PDF is on a finer and generally more precise atomic scale, whereas traditional LPA usually considers unit cells as smallest units ((Wilson, 1962), (Warren, 1990)).

Within the limit of the Stokes & Wilson's ((Stokes, et al., 1944), (Eastabrook, et al., 1952)), the FT of the overall line profile for the [hkl] direction in a given grain of the cluster is:

$$Y_{hkl}\left(L\right) = A_{hkl}\left(L\right) + iB_{hkl}\left(L\right) = V_{grain}A_{hkl}^{S}\left(L\right)\left(A_{hkl}^{D}\left(L\right) + iB_{hkl}^{D}\left(L\right)\right) \tag{3}$$

A special and frequently considered assumption is that $p_{L}\left(\Delta L_{hkl}\right)$ be symmetrical ($B_{hkl}^{D}=0$), and Gaussian in particular, so that:

$$Y_{hkl}^{D}\left(L\right) \simeq A_{hkl}^{D}\left(L\right) = \exp\left[-q^{2}L^{2}\left\langle \varepsilon_{hkl}^{2}\left(L\right)\right\rangle /2\right] \tag{4}$$

This is the underlying hypotheses of the WA method ((Warren, et al., 1950), (Warren, et al., 1952), (Warren, 1955), (Warren, 1959), (Warren, 1990)), which can be shown to be still approximately valid even if the distribution is not exactly Gaussian, provided it is a bell-shaped, symmetrical distribution function (Warren, 1959). As further discussed below, the D-PDFs for the studied cluster are neither Gaussian nor symmetrical.

The powder diffraction pattern for a cluster of grains can be obtained by adding all contributions as:

$$I(q) \propto \sum_{grain} V_{grain} \sum_{hkl} \int_{-\infty}^{\infty} A_{hkl}^{S}(L)\left[A_{hkl}^{D}(L)\cos(qL) + B_{hkl}^{D}(L)\sin(qL) \right] dL \quad (5)$$

where the proportionality factor includes $|\mathbf{F}|^2$, several constants and known trigonometric terms, whereas the actual integration limits are determined by the longest atom-atom distance along [hkl] of the given grain. The two sums extend to all grains and to all crystallographically equivalent directions, respectively.

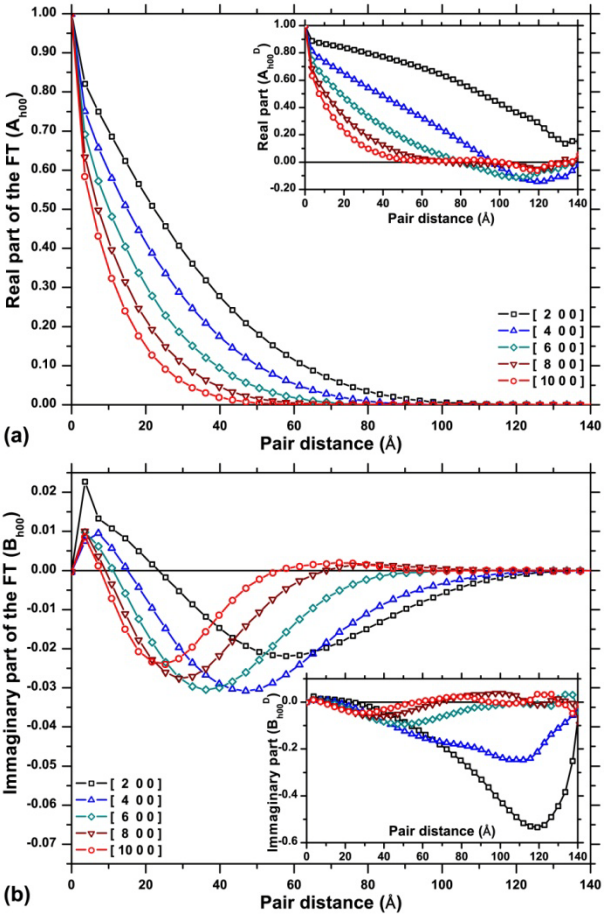

Figure VI - 5. Real (a) and imaginary (b) part of the Fourier Transform of the peak profile; the example refers to the h00 family of diffraction peaks (see text for details).

As an example of application of the D-PDF, Figure (5a) and (5b) show, respectively, real and imaginary parts of the FT for several orders of reflections belonging to the {h00} family, $Y_{h00}^{D}(L) = A_{h00}^{D}(L) + iB_{h00}^{D}(L)$. The real part decays increasingly faster for higher orders of reflections, whereas the imaginary part sensibly deviates from zero, as an effect of the asymmetry of D-PDFs. It is possible to see the combined effect of domain size and strain effects, with the trends of $A_{h00} = A_{h00}^{S} A_{h00}^{D}$ and $B_{h00} = A_{h00}^{S} B_{h00}^{D}$ (assuming $V_{grain} = 1$ for simplicity).

The decay of the real part is smooth and demonstrates that the integration limits in eq. (5) do not need to extend beyond ca 120 Å, in this specific case, as an effect of the finite size of the domain. The fact that different orders of reflections belonging to the same family have different trends, with a faster decay for the higher orders (i.e., larger q values), clearly demonstrates the presence of a strain broadening component.

6.3.2 Powder pattern from a nano-polycrystalline microstructure

As already pointed out in the Introduction, the most straightforward and correct way to calculate the powder diffraction pattern for an atomistic model is by the Debye Scattering Equation ((Derlet, et al., 2005), (Cervellino, et al., 2010), (Cervellino, et al., 2003)). The DSE makes no assumptions on crystalline structure and lattice defects, as it is based only on correlations between all possible couples of atoms. As such it can be computationally demanding (although nowadays entirely viable (Gelisio, et al., 2010)) but quite rigorous, so that we can consider the DSE result as an “experimental” pattern, to which the D-PDF analysis discussed above can be compared.

As remarked in the introduction, the purpose is to test the D-PDF approach, to better understand and validate the traditional LPA methods and their results, but also to study the features of a nano-polycrystalline microstructure obtained by MD in terms of a well-known, easy to perform experimental technique like diffraction.

As a first test we considered the starting cluster, just after the atom filling procedure, but before any energy minimization and thermalization steps. This corresponds to a system of perfect crystalline grains, where the only effect on line profiles is that of the finite domain size. As shown in Figure (6), the match between the DSE pattern and that generated by using eq. (5) is remarkably good ((Leonardi, et al., 2012(a)), (Leonardi, et al., 2012(c))). This result is somehow expected, as no strain and no deviation from a perfect crystalline order is present, but is important to assess the quality of the hypotheses underlying eq. (5), among which the Tangent Plane Approximation (Beyerlein, et al., 2011), and the lack in eq. (5) of grain-grain correlations, which are instead considered by the DSE.

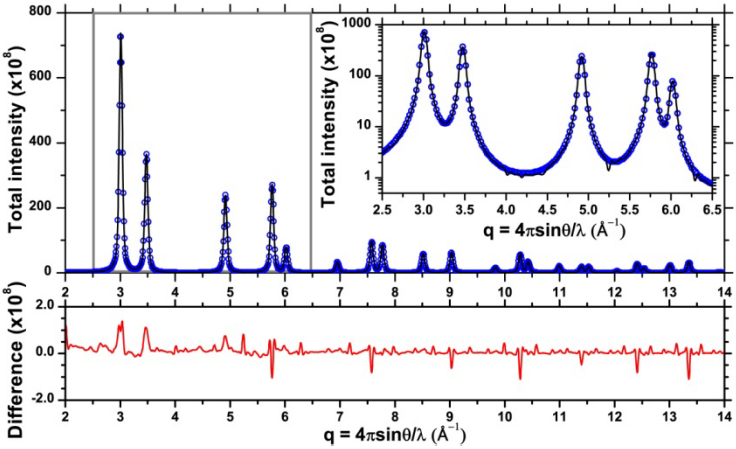

Figure VI - 6. Powder diffraction pattern of the cluster of Figure (1) as obtained by DSE (circle) and the D-PDF approach (eq. (5), line). Difference is shown below. Inset highlights details in the peak tail region.

The MD equilibration procedure introduces strains in the system, leading to a static component of the atomic displacement, which adds up to the dynamical component due to the thermal vibrations. At any given instant (frame) of the MD trajectory, the atom-atom displacement can be written as $\Delta L(t) = \Delta L_{stat} + \Delta L_{dyn}(t)$. Thermal effects, at least in an approximate way, might be added to the simulation of the powder pattern (e.g., by introducing a Debye-Waller factor and a Temperature Diffuse Scattering ((Beyerlein, et al., 2012), (Warren, 1990)). However, to the purpose of studying the static component it is more convenient to introduce the concept of Time-averaged Atomic Coordinates (TACs): the atomic coordinates of all atoms in the studied system are averaged over a suitably large number of time frames of the MD trajectory, so that $\overline{\Delta L(t)} = \Delta L_{stat}$. In this way we can get rid of the dynamical component of atomic displacement and refer the diffraction LPA to the static component only. Once the TACs are known, the DSE pattern is easily obtained as explained before. The D-PDF pattern is then built according to eqs. (1) and (5).

If we now consider the system after MD, Figure (7a) shows the detail for the (200) peak, as obtained by adding all {200} reflections in the cluster. While the inset points out the <h00> directions in different grains, the plot below shows an interesting feature of the position (q_B) of the (h00) peaks in the cluster, which changes as a function of the size of the corresponding grain, as an effect of the strain dependence on the grain size (cf. Figure (3)).

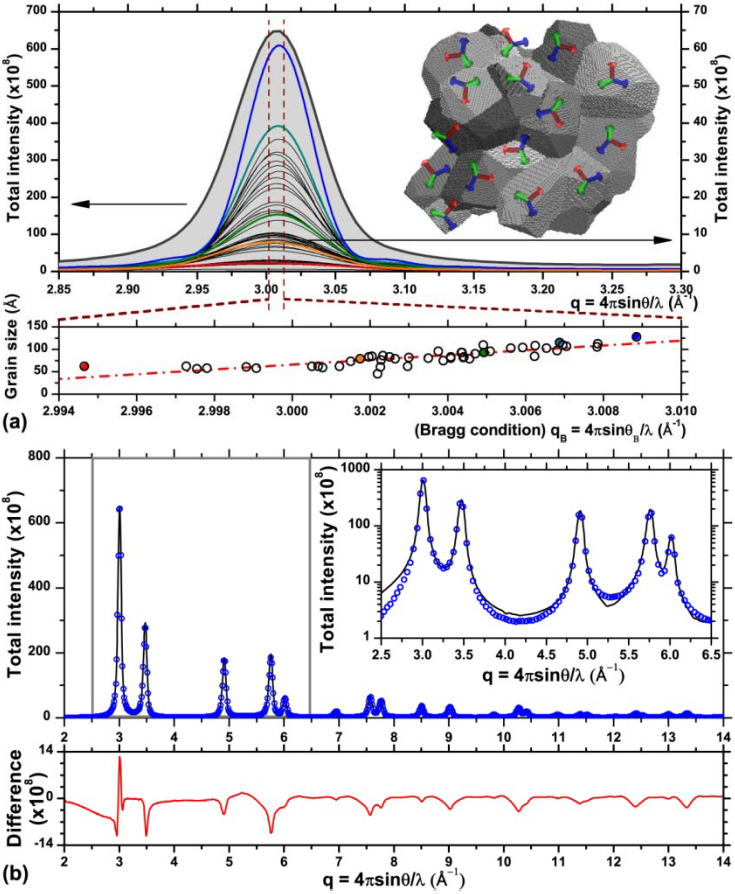

Figure VI - 7. Powder pattern of the system of Figure (1) after MD: detail of (200) peak as built from the D-PDF method of eq.(5) (a); comparison between DSE (circle) and D-PDF patterns (line), with difference plot below (b).

Figure (7b) shows a comparison between the patterns for the equilibrated system, as obtained by DSE and D-PDF. Differences, which are small but visible, are expected and suggest interesting features of the strain field. While the DSE includes all regions of the cluster independently of their order, whether they are crystalline or amorphous, the D-PDF refers by definition to an underlying crystalline lattice: local atomic displacement is allowed (D-PDF position, width and shape) but in any case within the limits of an average crystalline framework. The residual in Figure (7b) is therefore related to a high strain region, somehow in between a highly distorted crystalline lattice and an amorphous phase, which is very likely the grain boundary area. Moreover, while the DSE is sensitive to all possible correlations within the

cluster, i.e., between atoms inside each grain as well as between atoms of different grains (Leonardi, et al., 2012(b)), the D-PDF approach only considers the former correlations.

To test this hypothesis the DSE and the D-PDF patterns where calculated again, on the same equilibrated cluster but after removing respectively one, two or three external atomic layers from all grains. In this way the grain boundary region is progressively eliminated (Figure (8)).

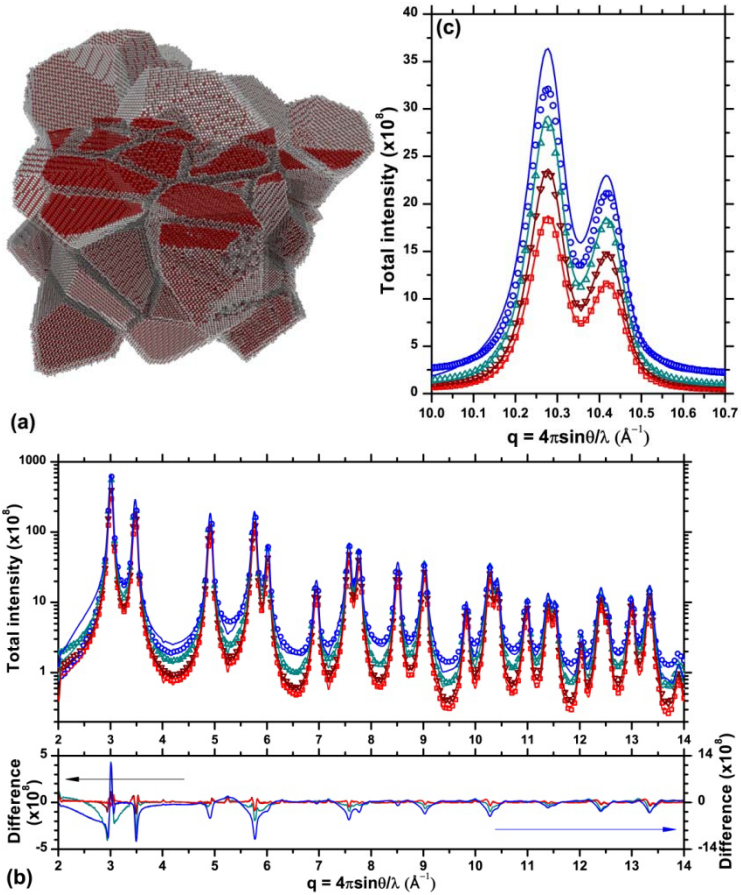

Figure VI - 8. MD equilibrated cluster of Figure (1) after removal of one atomic layer from each grain (a). DSE pattern for the equilibrated cluster (open circle) and after removal of 1 (upward triangle), 2 (downward triangle) and 3 (square) layers. Line refers to the corresponding patterns calculated from the D-PDF approach of eq. (5) (b); difference between DSE and D-PDF patterns is shown below. A detail for (531) and (442)/(600) peaks is shown in (c).

As shown in Figure (8c) for restricted angular region at relatively high q, the match between the DSE and the D-PDF patterns markedly improves by removing surface layers. As soon as the first layer is removed then only fully coordinated atoms are considered and most of the discrepancy disappears (Figure (8c)). Besides zeroing the peaks in the low-q region of the residual, this step also eliminates nearly completely the diffuse scattering at higher q values. This last detail is visible by comparing the insets of Figures (7b) and (8b).

These results show how studying clusters with progressive layer removal can help investigating the degree of disorder in the grain boundary region, the contribution of this region to the strain field in the grains, and corresponding line broadening and diffuse scattering. Results suggest that the grain boundary region – as obtained from the adopted MD equilibration procedure – is highly distorted: it cannot be said truly crystalline but it is not even a completely amorphous phase (Leonardi, et al., 2012(b)). Effects on line profiles are clearly visible, even more so the smaller the crystalline domains.

6.3.3 D-PDF and r.m.s strain

It is interesting to consider again the DSE pattern as an "experimental" pattern from a nano-polycrystalline system, and make a traditional line profile analysis. As a first step, which is ordinary practice in real cases of study, profile fitting is used to separate contributions from the different, strongly overlapping peaks (Dong, et al., 2000). Fitting results shown in Figure (9) are reasonably good, although less satisfactory for the peaks at lower q, which are more affected by the grain boundary and the grain-grain correlations discussed in the previous paragraph. From this analysis (Dong, et al., 2000) it is straightforward to obtain the plot of Figure (10), i.e., the logarithm of the Fourier Transform of the line profiles as a function of q^2 $((q/2\pi)^2$ for historical reasons), for different pair distances L.

According to Warren and Averbach, the observed data can be described as ((Warren, et al., 1950), (Warren, et al., 1952), (Warren, 1955), (Warren, 1959), (Warren, 1990)):

$$\begin{aligned} \ln\left[Y_{hkl}(L)\right] &\simeq \ln\left[A^S_{hkl}(L)\,A^D_{hkl}(L,q)\right] \\ &= \ln\left[A^S_{hkl}(L)\right] - 2\pi^2 L^2 \left\langle \varepsilon^2_{hkl}(L)\right\rangle (q/2\pi)^2 \end{aligned} \qquad (6)$$

so that information on the domain size and variance of the strain distribution $\left\langle \varepsilon^2_{hkl}(L)\right\rangle$ (or of the displacement distribution, $\left\langle (\Delta L)^2_{hkl}\right\rangle = L^2\left\langle \varepsilon^2_{hkl}(L)\right\rangle$) can be obtained, respectively, from intercept and slope of the trends in Figure (10) for different pair distance values. To properly account for a possible dependence on the crystallographic direction, the procedure is performed separately for peak profiles belonging to different {hkl} families (Warren, 1959), although an analysis involving all observed peaks can also be informative.

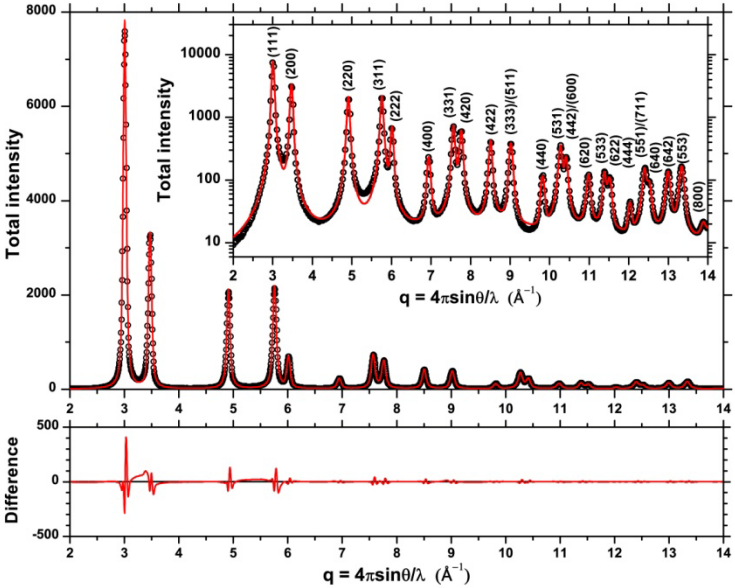

Figure VI - 9. Result of profile fitting of the pattern given by the Debye scattering Function for the studied metallic cluster: DSE data (circle), best fit with pseudoVoigt functions (line) and difference between the two (residual, line below). Corresponding Miller indices are shown in the log-scale plot in the inset.

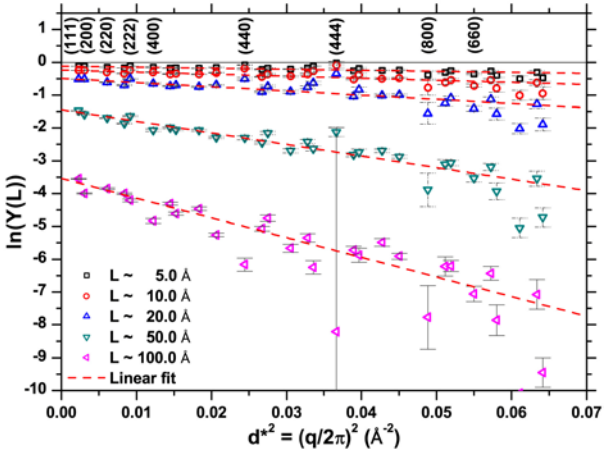

Figure VI - 10. Warren-Averbach plot: logarithm of the Fourier Transform of the peak profiles (from profile fitting in Figure (9)) as a function of the square of the scattering vector, $(q/2\pi)$, for a selection of pair distances, L (5, 10, 20, 50, 100 Å). Points with the same $(q/2\pi)^2$ correspond to a given set of Miller indices, shown on top for the {hhh} and {h00} families ((333) and (600) are not considered as they overlap with other reflections).

Figure (11) shows the standard deviation $\sqrt{\left\langle (\Delta L)^2_{hkl} \right\rangle}$ as a function of *L* for (111)/(222)/(444) and (200)/(400)/(800) ((333) and (600) were excluded as they overlap, respectively, with (531) and (442)). As shown in the original paper by Warren and Averbach (Warren, et al., 1950), all trends should start from the origin: while this happens for the {h00} family, it is not the case for the {hhh} family, which gives a trend crossing the abscissa just above *L*=20 Å. This is an artefact at least partly caused by systematic errors in the profile fitting (e.g. of the (111) peak, see Figure (9)) and by the severe overlapping of the peak profiles (especially relevant for the weak (444) peak), which are typical problems also in real cases of study. However, as expected for the elastic anisotropy of copper, the r.m.s. displacement is higher for {h00} than for {hhh}, while results from other {hkl} families fall between these two limits.

In Figure (11) it is also shown the result from all observed peak profiles: this procedure disregards the elastic anisotropy, but helps averaging the effects of a not perfect fitting of the peak profiles. Several studies have proposed an interpretation of the trends in Figure (11). According to Adler and Houska (Adler, et al., 1979), the data of Figure (11) should obey a simple power law, $\sqrt{<(\Delta L)^2_{hkl}>} = k \cdot L^{r+1}$, with $-1 \le r \le 0$. The value found for {h00} is $r = -0.44(2)$, whereas the fit to the data from all peak profiles gives $r = -0.47(1)$. A value around $r = -0.5$ is considered as typical of cold-worked metals, and would be due to the non-uniform strain field of dislocations (Adler, et al., 1979).

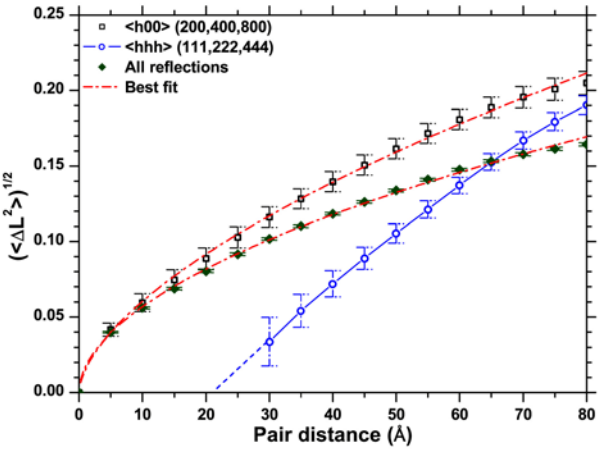

Figure VI - 11. Warren's plot: standard deviation of the $p_L\left(\Delta L_{hkl}\right)$ distribution as a function of the atomic pair distance along <h00> (square), <hhh> (circle), and average over all <hkl>; best fit (dash-dot) refers to a power law (see text for details).

Before considering the correct trend of $\sqrt{\langle (\Delta L)^2_{hkl} \rangle}$ from the D-PDF analysis, it is worth analysing the results on the domain size obtained from the intercepts in Figure (10). For simplicity we consider the {h00} family, which gave a plausible trend in Figure (11). It can be shown that in a plot of the size coefficients $A^S_{hkl}(L)$ as a function of *L*, the intercept with the abscissa of the tangent to the curve in $L = 0$ is a surface-weighted mean domain size, $< D >_S$; the second derivative of $A^S_{hkl}(L)$, instead, is proportional to the domain's length distribution along the scattering vector direction (so-called column length), from which it can be calculated a volume-weighted mean domain size, $< D >_V$ ((Warren, 1990), (Bertaut, 1950), (Bertaut, 1952)). Figure (12) shows the column length distribution along [h00]; mean sizes are $< D >_S = 48$ Å and $< D >_V = 62$ Å.

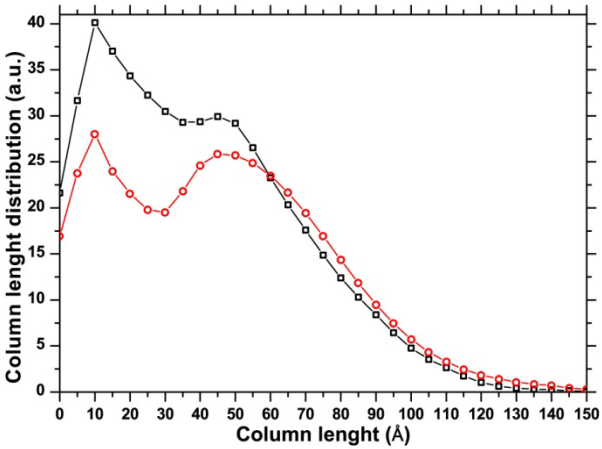

Figure VI - 12. Column length distributions along [h00], as obtained from the Warren-Averbach analysis of profile data from the DSE pattern (circle) and directly from the D-PDF analysis (square).

These results can be compared with the values provided by the D-PDF analysis, which can be considered "exact", in that directly obtained from the known parameters of the cluster. The CVF is obtained from the area of D-PDF curves (e.g., those in Figure (4)), and after normalization to the grain volume it provides the size coefficients for the given grain and [hkl] direction. The $A^S_{hkl}(L)$ are then calculated by averaging the coefficients over all grains in the cluster, and the second derivative provides the column length distribution. This procedure, applied to the [h00] direction, gives $< D >_S = 40$ Å and $< D >_V = 59$ Å, and the column length

distribution shown in Figure (12). Despite the quite different procedures involved, the column length distributions are remarkably similar. The Warren-Averbach method based on the profile fitting tends to overestimate the size, the discrepancy being larger for $< D >_S$ than for $< D >_V$, as the former is more influenced by the shorter lengths, which in turn depend more directly on the peak profile tail region less accurately described by the profile fitting.

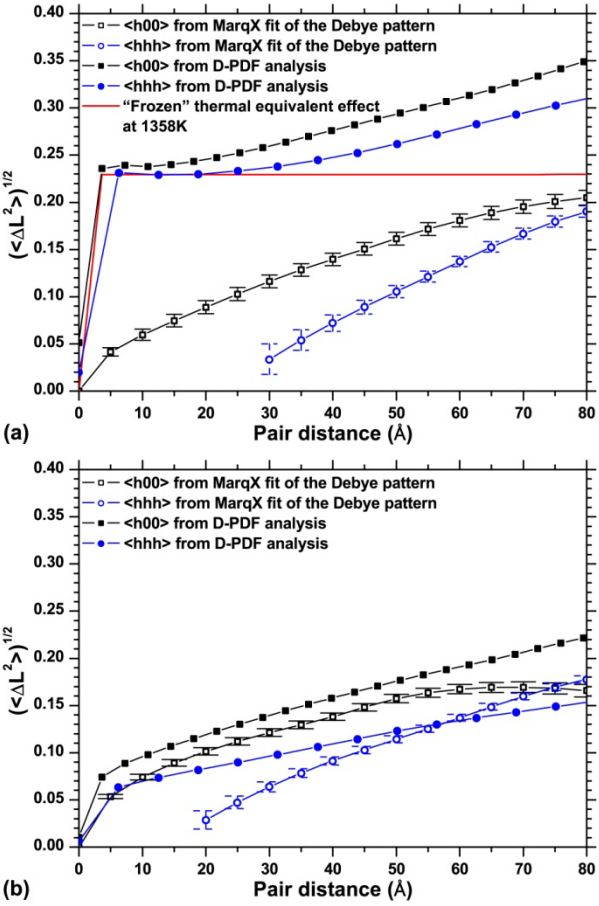

Figure VI - 13. Warren's plot comparing results of Figure (11), obtained from the Warren-Averbach analysis of profile data from the DSE pattern (full symbol), with the standard deviation of the strain distribution directly calculated from the D-PDFs. Results refer to the microstructure of Figure (1) after MD equilibration (a) and after removal of one atomic layer from the surface of all grains in the cluster (b). Full line in (a) indicates the equivalent thermal strain at melting temperature.

Standard deviations of the strain distribution are easily calculated numerically for each D-PDF curve, and averaging this result over equivalent directions of all grains provides $\sqrt{\left\langle (\Delta L)_{hkl}^2 \right\rangle}$ for the cluster. Trends for the [h00] and [hhh] directions are shown in Figure (13), together with the corresponding results from the Warren-Averbach method.

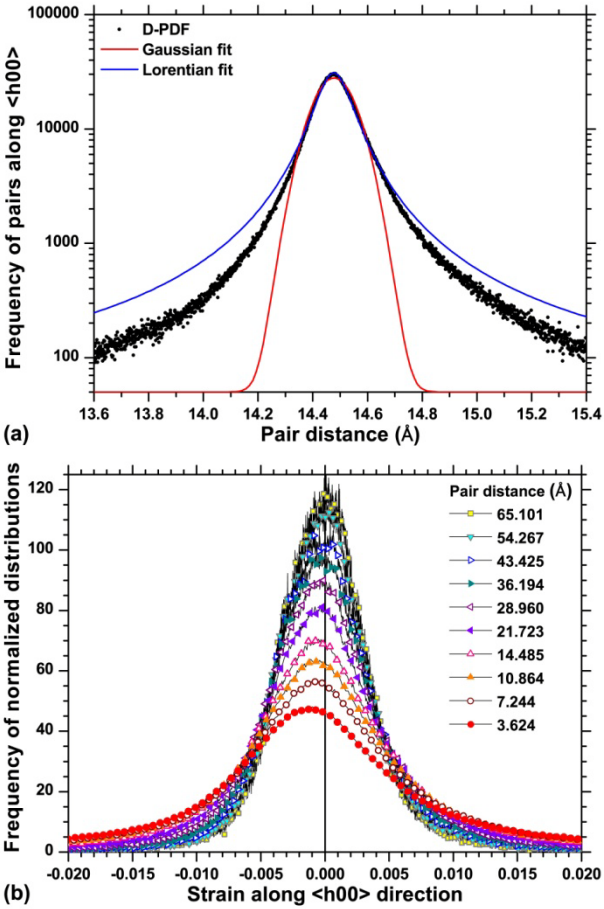

Figure VI - 14. Example of a $p_L(\Delta L_{hkl})$ distribution for L=14.485 Å (average over the whole cluster for the [h00] direction) with best fit of a Gaussian and of a Lorentzian function (a); corresponding strain distributions $p_L(\varepsilon_{hkl})$ for different L values (b).

While the agreement between results on domain size was good, the standard deviations of the displacement distribution look completely different. Reasons for this discrepancy can be found in the fine features of the D-PDF curves, and in the simplifying assumptions underlying the Warren-Averbach method.

As shown in Figure (14), the assumption of a Gaussian and symmetrical $p_L\left(\Delta L_{hkl}\right)$ is far from being correct; moreover, the shape of the strain distribution changes for different pair distances (Figure (14b)). However, the non-Gaussian (and asymmetrical) nature of the $p_L\left(\Delta L_{hkl}\right)$ alone cannot explain the large discrepancy in the results of Figure (13). An interesting feature, visible in the log scale plot of Figure (14a), is the constant "background", i.e., the fact that the distributions do not fall to zero with increasing distance from the expected (perfect crystal) value of atomic pair distance *L*. This constant component is due to the highly disordered grain boundary region, which contributes to the peak profiles with an atomic displacement effect independent of *L*. This is similar to the effect explained by Warren and Averbach for the thermal vibrations, with the important difference that the strain component involved here is static, as the dynamic component was removed before producing the DSE pattern.

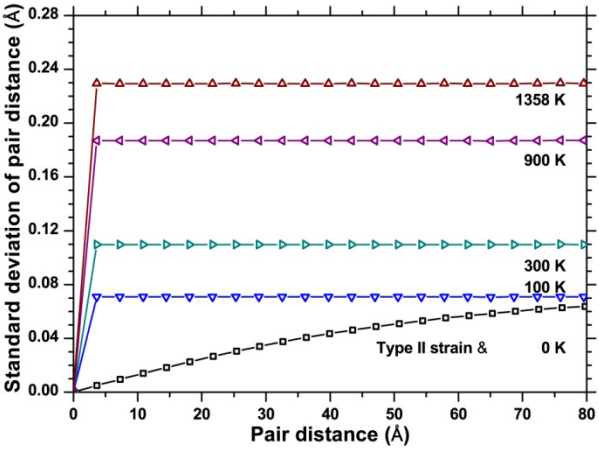

Figure VI - 15. Standard deviation of a strain distribution simulated by adding increasing levels of random static disorder, with indication of the corresponding equivalent temperature. Type II strain effect is also shown (see text for details).

To test this hypothesis, starting from the "crystallographic" system (i.e., before any energy minimization and thermalisation procedure), we added increasing levels of random static disorder (as in a "frozen" thermal effect). The D-PDF analysis gives the $\sqrt{\left\langle (\Delta L)^2_{hkl} \right\rangle}$ trends in Figure (15), showing a constant value increasing with the

equivalent temperature, up to $\sqrt{\left\langle (\Delta L)^2_{hkl} \right\rangle} \approx 0.23$ for an effect equivalent to the melting point of copper (ca 1358K). As shown by the dash line in Figure (13a), this value agrees quite well with the sharp step in the $\sqrt{\left\langle (\Delta L)^2_{hkl} \right\rangle}$ trend.

A further contribution to the observed strain is of course given by the non-uniform strain across grains, and from grain to grain, shown in Figures (2) and (3). These are responsible for the *L*-dependent component of the trend in Figure (13), and could be schematically labelled as strains of II (inter-granular) and III (intra-granular) type ((Van Houtte, 1993), (Hutchings, et al., 2005)). For a simplified estimate of this complex effect, we added to the crystallographic cluster a pure type II strain. This was made by changing the mean unit cell parameter of each grain according to values of Figure (3), resulting in a nearly linear increase of the standard deviation with the pair distance (Figure (15)). A combination of the two effects, II type and random static disorder equivalent to 1358K, explains at least qualitatively the trend observed in Figure (13). Differences are due to the simplification of considering a type II strain only, whereas the strain also changes inside each grain with a type III component. Moreover, elastic anisotropy should also be taken into account.

Indeed, as shown in Figure (13) for the two extreme directions <h00> and <hhh>, the standard deviation of the atomic displacement distribution depends on the crystallographic direction. Further evidence is provided by Figure (3), where the trend of the unit cell parameter as a function of the largest thickness in a grain depends on the crystallographic direction considered. This anisotropic behaviour can be investigated following the idea originally proposed by Stokes and Wilson (Stokes, et al., 1944).

In Figure (16) the average variance $\left\langle (\Delta L)^2_{hkl} \right\rangle$ for different *L* values is plotted as a function of the invariant for the (cubic) Laue group of copper, $H = \left(h^2k^2 + k^2l^2 + l^2h^2\right) \Big/ \left(h^2 + k^2 + l^2\right)^2$. Apart from the very low *L* values (up to about 20 Å), the trend is reasonably linear. It should be considered that the first step in the D-PDF is of different length for the different hkls (high indices can have rather long distances between neighbours). This can explain the scatter observed for low *L* values, where the highly disordered grain boundary contribution also plays the main role.

It is also possible to plot the standard deviation $\sqrt{\left\langle (\Delta L)^2_{hkl} \right\rangle}$ as a function of *H* (Figure (16)). The fit is also acceptably linear, but the best regression is obtained for the $\left\langle (\Delta L)^2_{hkl} \right\rangle$ vs. *H* plot. We could further speculate on this result, to find the best functional dependence of $\sqrt{\left\langle (\Delta L)^2_{hkl} \right\rangle}$ on *H*, but the main conclusion is that this correlation is a consequence of the elastic anisotropy of the metal. A similar effect is

also observed when dislocations are responsible for line broadening, and can be expressed via the Contrast Factor concept ((Wilkens, 1970), (Wilkens, 1969), (Martinez-Garcia, et al., 2009)), but in our case, quite evidently, no dislocations are present. This suggests great caution in univocally attributing line profile broadening anisotropy to dislocations, which, quite evidently, are just one possible source for this directional effect.

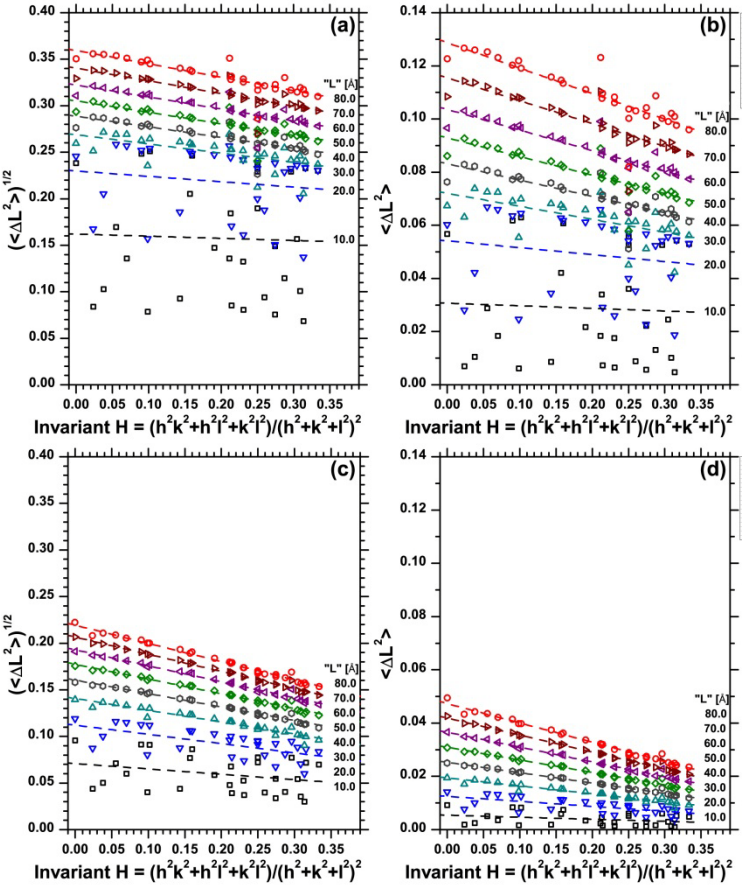

Figure VI - 16. Standard deviation (a,c) and variance (b,d) of the strain distribution as a function of the invariant form *H*, for different values of the pair distance, *L*. Results refer to the MD equilibrated system before (a, b) and after removal of one atomic layer from all grains (c,d).

The analysis presented in this paragraph can be repeated on the DSE patterns of Figure (8). After removal of one surface layer from each grain

(corresponding to remove all atoms with coordination lower than 12), all D-PDFs are in general much narrower than those of the complete MD equilibrated cluster. In addition to that, as shown in Figure (17), the removal of a surface layer drastically reduces the extension of the distribution tails and of the constant component, which was interpreted as "frozen" thermal-like effect of the disordered grain boundary region. An additional layer removal further extends this effect.

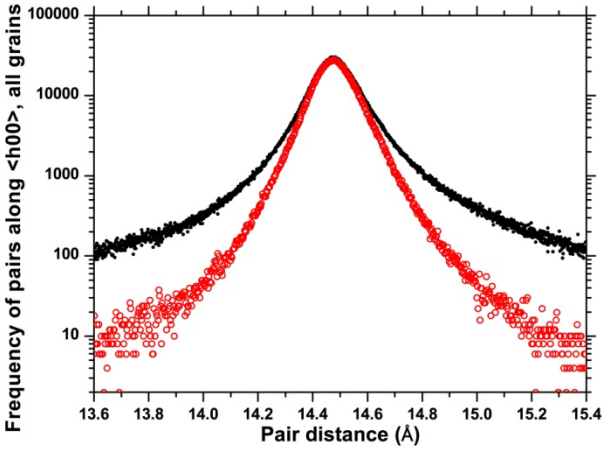

Figure VI - 17. Example of a $p_L(\Delta L_{hkl})$ distribution from Figure (14a) for the MD equilibrated system (full circle) and after removal of one atomic layer from all grains (open circle).

The standard deviation of the atomic displacement is consequently smaller than in the starting cluster. The observed trend in Warren's plot (Figure (13b)) is much more "regular", i.e., as expected from the Warren-Averbach model (Warren, et al., 1950), as a consequence of the much reduced (nearly eliminated) constant contribution of the grain boundary. This further confirms the role of the grain boundary as a region with high disorder but still contributing to the coherent scattering of the crystalline grains: not all scattering from the grain boundary is diffuse scattering. As a further support to this interpretation, Figure (13b) shows that the WA analysis on the DSE pattern after removal of one surface layer from each grain leads to results much closer to those from the D-PDF analysis than for the starting cluster (cfr Figure (13a)). Finally, it is also worth noting that after one layer removal the anisotropy of line broadening is more evident, even if the total strain is lower than in the original cluster. As shown in Figure (16d), the plot of the variance as a function of *H* gives linear correlations for any *L* value with a lower data scatter than in Figure (16b).

6.4 Conclusions

The concept of Directional - Pair Distribution Function has been introduced to support a better understanding of the line broadening effects of diffraction peak profiles from nano-polycrystalline microstructures. The new concept, illustrated for a simple system made of (nearly equiaxed) nanocrystalline Cu grains equilibrated by MD, can easily be applied to any simulated microstructure, also including lattice defects and crystalline domains of any shape.

The D-PDF analysis shows in detail how the local atomic displacement influences line profiles, also taking into account the anisotropy of the strain distribution. Most importantly, the D-PDF approach leads to results equivalent to a traditional Line Profile Analysis based on a Fourier analysis, like the method of Warren and Averbach, thus providing a direct possibility to understand the meaning of LPA results in terms of an atomistic model of the microstructure. This possibility can be especially useful for a correct interpretation experimental LPA results, and can provide further insights into the analysis of diffraction phenomena.

Chapter VII

Conclusion and Future Perspectives

This Thesis work focused on sample microstructures of metallic nano-polycrystalline materials, trying to combine the language of continuum mechanics with the specificity of the powder diffraction theory. As already pointed out in the Introduction, the main goal was to couple X-ray powder diffraction with a description of the local atomic environment, to better understand those fine effects of diffraction which can disclose important information on the properties of materials at the nano scale.

First part of the work concerned the generation of model microstructures. A modification of the existing algorithms was necessary to remove some of the geometrical constraints of existing space tessellation methods and to simultaneously take several statistical and geometrical properties into account. Realistic microstructures can now be generated e.g. with any assigned size distribution, shape of the grains (cells). Stress-strain relationships in a model nano-polycrystalline system were described in terms of CCD, VCD and eVCD, to determine in a consistent way strain and stress tensors on a local (i.e., atomic) scale.

Based on the results of the first part, the research addressed the main theme of the Thesis, i.e. establishing a direct connection between parameters typical of powder diffraction and the strain field, as described by continuum mechanics. Different contributions to the diffraction signal, such as size and shape of the coherently scattering domains (by means of the Common Volume Function concept), and distortion field of the crystalline lattice, were singled out and described. The contribution to diffraction arising from the interference between domains was studied

as well. The result is that domains in a cluster can show some degree of coherence and the contribution from the grain boundary region can be peaked in Bragg position and not being just diffuse (as e.g. in an amorphous case).

The relationship between lattice distortion and diffraction line profile was described in terms of Directional - Pair Distribution Functions (D-PDF). By means of this new approach, the concept of deformation expressed by continuum mechanics could be applied to the study and modelling of the powder diffraction line profiles.

Besides providing a clear understanding of the hybrid nature of the grain boundary region in nano-polycrystalline aggregates (which is neither crystalline nor completely amorphous), the D-PDF approach provides a better description for the traditional Line Profile Analysis methods like the Williamson-Hall plot and the Warren-Averbach method. In this context, it was shown how using those LPA methods without the support of suitable atomistic models can lead to erroneous results.

Even if the study was made on a cluster of grains with no defects other than the grain boundary, and with strains due to the equilibration process (energy minimization and thermalisation by Molecular Dynamics) only, the methods developed during this work can be considered of general applicability. It is envisaged the use on more complex systems, also including other lattice defects.

Properties like grain orientation (as of interest in textured materials) and other geometrical-topological features of the microstructure can be discussed in terms of their contribution to the macroscopic properties as well as the local atomic arrangement. In addition to the role of the grain boundary, different sources of lattice distortion can be investigated, also under the effect of external stresses applied to the studied cluster. Then it should be possible to study, in addition to the strain and stress of equilibrated nano-polycrystalline systems, also important transient phenomena like the slip of dislocations and the formation of planar defects (e.g. twins and stacking faults in general). The study of lattice defects can be made while external loads are applied to the system, or by following the evolution of the system from a starting non-equilibrium configuration.

In all of these studies, the relations between lattice defects and crystalline domains could be studied by powder diffraction, also including possible interference effects. Line Profile Analysis can benefit of the D-PDF concept to provide a much deeper understanding at the atomic level and improved stability for any of the existing or new profile fitting and modelling methods.

List of abbreviation and acronyms

AD…….. Atomic Density
AF…….. Averaged Frame
CCD……. Crystallographic Cell Deformation
CCP……. Cell Centre Position
CDF…….. Cumulative Distribution Function
CGF……. Cell Growth Factor
CL…….. Coordination Level
CMVT…… Constrained Modified Voronoi Tessellation
CPU……. Central Processing Unit
CSD……. Cell Surface Density
CVF……. Common Volume Function
CVT……. Constrained Voronoi Tessellation
D-PDF…… Directional - Pair Distribution Function
DSE……. Debye Scattering Equation
DT…….. Delaunay Triangulation
EAM……. Embedded Atom Method
ECS……. Equilibrium Crystal Shape
eVCD……. evolutional Voronoi Cell Deformation
FGF……. Face Growth Factor
FT…….. Fourier Transform
GB…….. Grain Boundary
GF…….. Growth Factor
GPU……. Graphics Processing Unit
IEP……. Interference Effects Plot
JMT……. Johnson-Mehl Tessellation
KM……. Key Model
KS…….. Kolmogorov-Smirnov
LAMMPS.. Large-scale Atomic/Molecular Massively Parallel Simulator

LJ……. Lennard-Jones

LPA…… Line Profile Analysis

LT……. Laguerre Tessellation

LVT…… Laguerre Voronoi Tessellation

m(NF)…. average number of faces in all neighbouring cells to a cell of NF faces

MD……. Molecular Dynamics

MSD……. Mean Square Displacement

MVT……. Modified Voronoi Tessellation

NA…….. Neighbours Analysis

NE…….. Number of Edges

NF…….. Number of Faces

NPT…… isothermal-isobaric time integration on Nose-Hoover style non-Hamiltonian equations

NV…….. Number of Vertices

NVT…… canonical time integration on Nose-Hoover style non-Hamiltonian equations

PBC……. Periodic Boundary Condition

PDF……. Probability Density Function

PIO……. Plane Interface Orientation

PIP……. Plane Interface Position

PVT…….. Poisson Voronoi Tessellation

r.m.s…… root mean square

RCPS…… Random Close Packing of Spheres

RF…….. Rotation Factor

RMC…….. Reverse Monte-Carlo

RS…….. Reciprocal Space

S……. Surface

SA/V…….. Surface-Area-to-Volume ratio

Sf……. Space filling

SF…….. Single Frame

TA…….. Time Average

TAC……. Time-averaged Atomic Coordinates

TPA……. Tangent Plane Approximation

V…….. Volume

VC…….. Voronoi Cell

VCD……. Voronoi Cell deformation

VmmCD.... Voronoi moment of mass Cell Deformation

VT…….. Voronoi Tessellation

WA……. Warren-Averbach

WH……. Williamson-Hall

WPPM…… Whole Powder Pattern Modelling

XRD……. X-Ray Diffraction

Ψ……. Sphericity

References

[1] Aboav, D. A., & Langdon, T. G. (1969). The distribution of grain diameters in polycrystalline magnesium oxide. *Metallography , 1* (3-4), 333-340.

[2] Ackland, G. J., & Jones, A. P. (2006). Applications of local crystal structure measures in experiment and simulation. *Physical Review B , 73*, 054104.

[3] Adler, T., & Houska, C. R. (1979). Simplifications in the x-ray line-shape analysis. *Journal of Applied Physics , 50*, 3282-3287.

[4] Allegra, G., & Wilson, A. J. C. (1983). Line profiles for a collection of identical crystals: effect of a linear transformation of shape. *Acta Crystallographica A , 39*, 280-282.

[5] Aurenhammer, F. (1991). Voronoi Diagrams - A Survey of a Fundamental Geometric Data Structure. *ACM Computing Surveys , 23* (3), 345-405.

[6] **Baccelli, F., & Błaszczyszyn, B. (2001)**. On a coverage process ranging from the Boolean model to the Poisson–Voronoi tessellation with applications to wireless communications. *Advances in Applied Probability , 33* (2), 293-323.

[7] Baletto, F., Mottet, C., & Ferrando, R. (2000). Molecular dynamics simulations of surface diffusion and growth on silver and gold clusters. *Surface Science , 446* (1-2), 31-45.

[8] Barabash, R. I., & Klimanek, P. (1999). X-ray scattering by crystals with local lattice rotation fields. *Journal of Applied Crystallography , 32* (6), 1050-1059.

[9] Beck, P. A. (1954). Annealing of cold worked metals. *Advances in Physics , 3* (11), 245-324.

[10] Bertaut, E. F. (1950). Raies de Debye-Scherrer et repartition des dimensions des domaines de Bragg dans les poudres polycristallines. *Acta Crystallographica , 3* (1), 14-18.

[11] Bertaut, E. F. (1952). Sur la correction de la transformée de Fourier d'une raie de Debye-Scherrer dans la mesure de dimensions cristallines. *Acta Crystallographica , 5* (1), 117-121.

[12] Beyerlein, K. R., Leoni, M., & Scardi, P. (2012). Temperature diffuse scattering of nanocrystals. *Acta Cristallographica A , 68* (3), 382-392.

[13] Beyerlein, K. R., Snyder, R. L., & Scardi, P. (2011). Powder diffraction line profiles from the size and shape of nanocrystallites. *Journal of Applied Crystallography , 44* (5), 945-953.

[14] Beyerlein, K. R., Snyder, R. L., Li, M., & Scardi, P. (2010). Application of the Debye function to system of crystallites. *Philosophical Magazine , 90* (29), 3891-3905.

[15] Bulatov, V., Abraham, F. F., Kubin, L., Devincre, B., & Yip, S. (1998). Connecting atomistic and mesoscale simulations of crystal plasticity. *Nature , 391*, 669-672.

[16] Calka, P. (2003). Precise formulae for the distributions of the principal geometric characteristics of the typical cells of a two-dimensional Poisson-Voronoi tessellation and a Poisson line process. *Advances in Applied Probability , 35* (3), 551-562.

[17] Cao, A. (2009). Molecular Dynamics Simulations of Nanocrystalline Nickel and Copper Revealing Different Failure Model of FCC Metals. *Materials Science Forum , 633 - 634*, 31-38.

[18] Cao, A., Wei, Y., & Ma, E. (2008). Grain boundary effects on plastic deformation and fracture mechanisms in Cu nanowires: Molecular dynamics simulations. *Physical Review B , 77*, 195429.

[19] Cervellino, A., Giannini, C., & Guagliardi, A. (2010). DEBUSSY: a Debye user system for nanocrystalline materials. *Journal of Applied Crystallography , 43* (6), 1543-1547.

[20] Cervellino, A., Giannini, C., & Guagliardi, A. (2003). Determination of nanoparticle structure type, size and strain distribution from X-ray data for monatomic f.c.c.-derived non-crystallographic nanoclusters. *Journal of Applied Crystallography , 36* (5), 1148-1158.

[21] Chen, S., Wang, Z. L., Ballato, J., Foulger, S. H., & Carroll, D. L. (2003). Monopod, Bipod, Tripod, and Tetrapod Gold Nanocrystals. *Journal of American Chemical Society , 125* (52), 16186-16187.

[22] Chiu, S. N. (1995). Aboav-Weaire's and Lewis' laws—A review. *Materials Characterization , 34* (1), 149-165.

[23] Christ, N. H., Friedberg, R., & Lee, T. D. (1982). Random lattice field theory: General formulation. *Nuclear Physics B , 202* (1), 89-125.

[24] Daw, M. S., & Baskes, M. I. (1983). Embedded-atom method: Derivation and application to impurities, surfaces, and other defects in metals. *Physical Review B , 29* (12), 6443-6453.

[25] Debye, P. (1915). Zerstreuung von Röntgenstrahlen. *Annalen der Physik , 351* (6), 809-823.

[26] Delaunay, B. N. (1934). Sur la sphère vide. *Bulletin of Academy of Sciences of the USSR* (6), 793-800.

[27] Derlet, P. M., & Van Swygenhoven, H. (2006). Application of Green's function and molecular dynamics to dislocations and lattice vibrations in small metal grains and grain boundaries. *SRMS-5 Conference*, (p. 138). Chicago.

[28] Derlet, P. M., & Van Swygenhoven, H. (2003). Atomic positional disorder in fcc metal nanocrystalline grain boundaries. *Physical Review B , 67*, 014202.

[29] Derlet, P. M., Van Pentegem, S., & Van Swygenhoven, H. (2005). Calculation of x-ray spectra for nanocrystalline materials. *Physical Review B , 71*, 024114.

[30] Dierickx, D., Basu, B., Vleugels, J., & Van der Biest, O. (2000). Statistical extreme value modeling of particle size distributions: experimental grain size distribution type estimation and parameterization of sintered zirconia. *Materials Characterization , 45* (1), 61-70.

[31] Dong, Y. H., & Scardi, P. (2000). MarqX: a new program for whole-powder-pattern fitting. *Journal of Applied Crystallography , 33* (1), 184-189.

[32] Drouffe, J. M., & Itzykson, C. (1984). Random geometry and the statistics of two-dimensional cells. *Nuclear Physics B , 235* (1), 45-53.

[33] Eastabrook, J. N., & Wilson, A. J. C. (1952). The Diffraction of X-Rays by Distorted-Crystal Aggregates III: Remarks on the Interpretation of the Fourier Coefficients. *Proceedings of the Physical Society B , 65* (1), 67-75.

[34] Egami, T., Maeda, K., & Vitek, V. (1980). Structural defects in amorphous solids A computer simulation study. *Philosophical Magazine A , 41* (6), 883-901.

[35] Fan, Z., Wu, Y., Zhao, X., & Lu, Y. (2004). Simulation of polycrystalline structure with Voronoi diagram in Laguerre geometry based on random closed packing of spheres. *Computational Materials Science , 29* (3), 301-308.

[36] Farjas, J., & Roura, P. (2008). Cell size distribution in a random tessellation of space governed by the Kolmogorov-Johnson-Mehl-Avrami model: Grain size distribution in crystallization. *Physical Review B , 78* (14), 144101.

[37] Fátima Vaz, M., & Fortes, M. A. (1988). Grain size distribution: The lognormal and the gamma distribution functions. *Scripta Metallurgica , 22* (1), 35-40.

[38] Fedorov, E. S. (1971). *Symmetry of crystals* (Vol. 7). American Crystallographic Association.

[39] Ferenc, J.-S., & Néda, Z. (2007). On the size distribution of Poisson Voronoi cells. *Physica A , 385*, 518-526.

[40] Foiles, S. M., Baskes, M. I., & Daw, M. S. (1986). Embedded-atom-method functions for the fcc metals Cu, Ag, Au, Ni, Pd, Pt, and their alloys. *Physical Review B , 33* (12), 7983-7991.

[41] Förster, S., Timmann, A., Schellbach, C., Frömsdorf, A., Kornowski, A., Weller, H., et al. (2007). Order causes secondary Bragg peaks in soft materials. *Nature Materials , 6* (11), 888-893.

[42] Frøseth, A. G., Van Swygenhoven, H., & Derlet, P. M. (2005). Developing realistic grain boundary networks for use in molecular dynamics simulations. *Acta Materialia , 53* (18), 4847-4856.

[43] Fung, Y.-C., & Tong, P. (2001). *Classical and Computational Solid Mechanics* (Vol. 1). Singapore: World Scientific Publishing Co.Pte.Ltd.

[44] Gelisio, L., & Scardi, P. (2012). X-ray interference by nanocrystalline domains. *Nanoscience Nanotechnology* , in Press.

[45] Gelisio, L., Azanza Ricardo, C. L., Leoni, M., & Scardi, P. (2010). Real-space calculation of powder diffraction patterns on graphics processing units. *Journal of Applied Crystallography , 43* (3), 647-653.

[46] Gelisio, L., Azanza Ricardo, C. L., Leoni, M., & Scardi, P. (2011). Real-space powder diffraction computing on clusters of Graphics Processing Units. *Zeitschrift für Kristallographie Proceedings , 1*, 189-194.

[47] Gilbert, E. N. (1962). Random Subdivisions of Space into Crystals. *Annals of Mathematical Statistics , 33* (3), 958-972.

[48] Gleiter, H. (2000). Nanostructured materials: basic concepts and microstructure. *Acta Materialia , 48* (1), 1-29.

[49] Godeke, A., ten Haken, B., & ten Kate, H. H. J. (2002). The deviatoric strain description of the critical properties of Nb3Sn conductors. *Physica C , 372-376* (3), 1295-1298.

[50] Goldman, A. (2010). The Palm measure and the Voronoi tessellation for the Ginibre process. *Annals of Applied Probability , 20* (1), 90-128.

[51] Goldman, A., & Calka, P. (2003). On the spectral function of the Poisson–Voronoi cells. *Annales de l'Institut Henri Poincare (B) Probability and Statistics , 39* (6), 1057-1082.

[52] Gravner, J., & Griffeath, D. (1997). Multitype threshold growth: convergence to Pisson-Voronoi tessellations. *Annals of Applied Probability , 7* (3), 615-647.

[53] Greaves, G. N., Greer, A. L., Lakes, R. S., & Rouxel, T. (2011). Poisson's ratio and modern materials. *Nature materials , 10*, 823-837.

[54] Gross, D., & Li, M. (2002). Constructing microstructures of poly- and nanocrystalline materials for numerical modeling and simulation. *Applied Physics Letters , 80* (5), 746-748.

[55] Groth, P. (1901). *Zeitschrift für Krystallographie und Mineralogie* (Vol. 34). Lepzig: Wilhelm Engelman.

[56] Guinier, A. (1963). *X-Ray Diffraction: In Crystals, Imperfect Crystals, and Amorphous Bodies.* San Francisco: W. H. Freeman and Company.

[57] Guo, Y.-B., Xu, T., & Li, M. (2012). Atomistic calculation of internal stress in nanoscale polycrystalline materials. *Philosophical Magazine , 92* (24), 3064-3083.

[58] Hasnaoui, A., Van Swygenhoven, H., & Derlet, P. M. (2002). Cooperative processes during plastic deformation in nanocrystalline fcc metals: A molecular dynamics simulation. *Physical Review B , 66*, 184112.

[59] Hilhorst, H. J. (2005). Asymptotic statistics of the n-sided planar Poisson–Voronoi cell: I. Exact results. *Journal of Statistical Mechanics: Theory and Experiment* , P09005.

[60] Hilhorst, H. J. (2009). Heuristic theory for many-faced d-dimensional Poisson–Voronoi cells. *Journal of Statistical Mechanics: Theory and Experiment* , P08003.

[61] Hinde, A. L., & Miles, R. E. (1980). Monte carlo estimates of the distributions of the random polygons of the voronoi tessellation with respect to a poisson process. *Journal of Statistical Computation and Simulation , 10* (3-4), 205-223.

[62] Honeycutt, J. D., & Andersen, H. C. (1987). Molecular dynamics study of melting and freezing of small Lennard-Jones clusters. *Journal of Physical Chemistry , 91* (19), 4950-4963.

[63] Hung, L.-I., Tsung, C.-K., Huang, W., & Yang, P. (2010). Room-Temperature Formation of Hollow Cu2O Nanoparticles. *Advanced Materials , 22*, 1910-1914.

[64] Hutchings, M. T., Withers, P. J., Holden, T. M., & Lorentzen, T. (2005). *Introduction to the Characterization of Residual Stress by Neutron Diffraction.* Boca Raton: CRC Press Taylor & Francis Group.

[65] Ibers, J. A., & Hamilton, W. C. (1974). *International Tables for Crystallography* (Vol. IV). Birminghm, England: The Kynoch Press.

[66] Ino, T., & Minami, N. (1979). X-ray diffraction by small crystals. *Acta Crystallographica A , 35*, 163-170.

[67] Ishihara, K. N., & Shingu, P. H. (1986). Calculation of Structure Factor for Thee-Dimensional Penrose Tilting. *Journal of the Physical Society of Japan , 55* (6), 1795-1798.

[68] Jacobsen, K. W., Norskov, J. K., & Puska, M. J. (1987). Interatomic interactions in the effective-medium theory. *Physical Review B , 35* (14), 7423-7442.

[69] Jang, D., & Atzmon, M. (2006). Grain-boundary relaxation and its effect on plasticity in nanocrystalline Fe. *Journal of Applied Physics , 99*, 083506.

[70] Jang, D., Li, X., Gao, H., & Greer, J. R. (2012). Deformation mechanisms in nanotwinned metal nanopillars. *Nature nanotechnology , 7*, 594-601.

[71] Krivoglaz, M. A. (1996). *X-Ray and Neutron Diffraction in Nonideal Crystals.* Berlin: Springer-Verlag.

[72] Kumar, S., Kurtz, S. K., Banavar, J. R., & Sharma, M. G. (1992). Properties of a three-dimensional Poisson-Voronoi tesselation: A Monte Carlo study. *Journal of Statistical Physics , 67* (3-4), 523-551.

[73] Kurzydzsowski, K. J. (1990). A model for the flow stress dependence on the distribution of grain size in polycrystals. *Scripta Metallurgica et Materialia , 24*, 879-883.

[74] Langford, J. I., & Wilson, A. J. C. (1978). Scherrer after sixty years: A survey and some new results in the determination of crystallite size. *Journal of Applied Crystallography , 11*, 102-113.

[75] Lautensack, C., & Zuyev, S. (2008). Random Laguerre Tessellation. *Advances in Applied Probability , 40* (3), 630-650.

[76] Leonardi, A., Beyerlein, K. R., Xu, T., Li, M., Leoni, M., & Scardi, P. (2011). Microstrain in nanocrystalline samples from atomistic simulation. *Zeitschrift für Kristallographie , 1*, 37-42.

[77] Leonardi, A., Leoni, M., & Scardi, P. (2012(a)). Atomistic interpretation of microstrain in diffraction line profile analysis. *Thin Solid Films* , In press.

[78] Leonardi, A., Leoni, M., & Scardi, P. (2013). Atomistic modelling of polycrystalline microstructures: an evolutional approach to overcome topological restrictions. *Computational Materials Science , 67*, 238-242.

[79] Leonardi, A., Leoni, M., & Scardi, P. (2012(b)). Interference Effects in Nanocrystalline Systems. *Metallurgical and materials transactions A* , In press.

[80] Leonardi, A., Leoni, M., Li, M., & Scardi, P. (2012(c)). Strain in atomistic models of nanocrystalline clusters. *Journal of Nanoscience and Nanotechnology* , Accepted for pubblication.

[81] Leonardi, A., Scardi, P., & Leoni, M. (2012(d)). Realistic nano-polycrystalline microstructures: beyond the classical Voronoi tessellation. *Philosophical Magazine , 92* (8), 986-1005.

[82] Levine, L. E., Geantil, P., Larson, B. C., Tischler, J. Z., Kassner, M. E., Liu, W., et al. (2011). Disordered long-range internal stresses in deformed copper and the mechanisms underlying plastic deformation. *Acta Materialia , 59* (14), 5803-5811.

[83] Lewis, F. T. (1928). The correlation between cell division and the shapes and sizes of prismatic cells in the epidermis of cucumis. *Anatomical Record , 38* (3), 341-476.

[84] Li, J., & Shimizu, F. (2005). Least-Square Atomic Strain. *Unpublished* . http://li.mit.edu/Archive/Graphics/A/annotate_atomic_strain/Doc/main.pdf.

[85] Li, Q.-K., & Li, M. (2006). Atomic scale characterization of shear bands in an amorphous metal. *Journal of Applied Physics Letters , 88*, 241903.

[86] Link, S., Burda, C., Wang, Z. L., & El-Sayed, M. A. (1999). Electron dynamics in gold and gold–silver alloy nanoparticles: The influence of a nonequilibrium electron distribution and the size dependence of the electron–phonon relaxation. *Journal of Chemical Physics , 111* (3), 1255-1264.

[87] Liu, Y., Zhou, J., & Ling, X. (2010). Impact of grain size distribution on the multiscale mechanical behavior of nanocrystalline materials. *Materials Science and Engineering A , 527* (7-8), 1719-1729.

[88] Lochmann, K., Oger, L., & Stoyan, D. (2006). Statistical analysis of random sphere packings with variable radius distribution. *Solid State Science , 8*, 1397-1413.

[89] Lou, X. W., Archer, L. A., & Yang, Z. (2008). Hollow Micro-/Nanostructures: Synthesis and Applications. *Advanced Materials , 20* (21), 3987-4019.

[90] Lucarini, V. (2008). From Symmetry Breaking to Poisson Point Process in 2D Voronoi Tessellations: the Generic Nature of Hexagons. *Journal of Statistical Physics , 130* (6), 1047-1062.

[91] Lucarini, V. (2009). Three-Dimensional Random Voronoi Tessellations: From Cubic Crystal Lattices to Poisson Point Processes. *Journal of Statistical Physics , 134* (1), 185-206.

[92] Mackay, A. L. (1982). Crystallography and the penrose pattern. *Physica A: Statistical Mechanics and its Applications , 114* (1-3), 609-613.

[93] Mackenzie, J. K. (1958). Second paper on statistical associated with the random disorientation of cubes. *Biometrika , 45* (1-2), 229-240.

[94] Mahadevan, S., & Zhao, Y. (2002). Advanced computer simulation of polycrystalline microstructure. *Computer Methods in Applied Mechanics and Engineering , 191* (34), 3651–3667.

[95] Martinez-Garcia, J., Leoni, M., & Scardi, P. (2009). A general approach for determining the diffraction contrast factor of straight-line dislocations. *Acta Crystallographica A , 65* (1), 109-119.

[96] Meijering, J. L. (1953). Interface area, edge lenght, and number of vertices in crystal aggregates with random nucleation. *Philips Research Report , 8*, 270-290.

[97] Miles, R. E., & Maillardet, R. J. (1982). The Basic Structures of Voronoi and Generalized Voronoi Polygons. *Journal of Applied Probability , 19*, 97-111.

[98] Mittemeijer, E. J., & Scardi, P. (2004). *Diffraction Analysis of the Microstructure of Materials* (Vol. 68). Berlin: Springer-Verlag.

[99] Møller, J. (1994). *Lectures on random Voronoi tessellations.* Springer-Verlag.

[100] Møller, J. (1992). Random Johnson-Mehl Tessellations. *Advances in Applied Probability , 24* (4), 814-844.

[101] Morawiec, A. (1995). Misorientation-Angle Distribution of Randomly Oriented Symmetric Objects. *Journal of Applied Crystallography , 28* (3), 289-293.

[102] Mott, P. H., Argon, A. S., & Suter, U. W. (1992). The atomic strain tensor. *Journal of Computational Physics , 101* (1), 140-150.

[103] Muche, L. (1996). Distributional Properties of the Three-Dimensional Poisson Delaunay Cell. *Journal of Statistical Physics , 84* (1-2), 147-167.

[104] Narasimhan, M. N. L. (1993). *Principles of Continuum Mechanics.* New York: Wiley-Interscience.

[105] Norris, S. A., Samela, J., Bukonte, L., Backman, M., Djurabekova, F., Nordlund, K., et al. (2011). Molecular dynamics of single-particle impacts predicts phase diagrams for large scale pattern formation. *Nature Comunications , 2*, 276.

[106] O'Keeffe, M. (1979). A proposed rigorous definition of coordination number. *Acta Crystallographica A , 35* (5), 772-775.

[107] Penrose, R. (1974). The Role of Aesthetics in Pure and Applied Mathematical Research. *Bulletin of the Institute of Mathematics and Its Applications , 10* (7-8), 266-271.

[108] Pineda, E., Bruna, P., & Crespo, D. (2004). Cell size distribution in random tessellations of space. *Physical Review E , 70*, 066119.

[109] Plimpton, S. (1995). Fast Parallel Algorithms for Short-Range Molecular Dynamics. *Journal of Computational Physics , 117* (1), 1-19.

[110] Rafaja, D., Klemm, V., Schreiber, G., Knapp, M., & Kuzel, R. (2004). Interference phenomena observed by X-ray diffraction in nanocrystalline thin films. *Journal of Applied Crystallography , 37* (4), 613-620.

[111] Rafaja, D., Poklad, A., Klemm, V., Schreiber, G., Heger, D., Šíma, M., et al. (2006). Some consequences of the partial crystallographic coherence between nanocrystalline domains in Ti–Al–N and Ti–Al–Si–N coatings. *Thin Solid Films , 514* (1-2), 240-249.

[112] Rafaja, D., Valvoda, V., Kub, J., Temst, K., Van Bael, M. J., & Bruynseraede, Y. (2000). Long-range periodicity and disorder in two-dimensional arrays of metallic dots studied by x-ray diffraction. *Physical Review B , 61* (23), 16144-16153.

[113] **Rafaja, D., Wüstefeld, C., Dopita, M., Růžička, M., Klemm, V., Sc**hreiber, G., et al. (2007). Internal structure of clusters of partially coherent nanocrystallites in Cr–Al–N and Cr–Al–Si–N coatings. *Surface and Coatings Technology , 201* (24), 9476-9484.

[114] Rhines, F. N., & Patterson, B. R. (1982). Effect of the Degree of Prior Cold Work on the Grain Volume Distribution and the Rate of Grain Growth of Recrystallized Aluminum. *Metallurgical Transactions A , 13* (6), 985-993.

[115] Rivier, N. (1985). Statistical crystallography Structure of random cellular networks. *Philosophical Magazine B , 52* (3), 795-819.

[116] Robinson, I., & Harder, R. (2009). Coherent X-ray diffraction imaging of strain at the nanoscale. *Nature Materials , 8*, 291-298.

[117] Samaras, M., Derlet, P. M., Van Swygenhoven, H., & Victoria, M. (2003). Movement of interstitial clusters in stress gradients of grain boundaries. *Physical Review B , 68*, 224111.

[118] Scardi, P., & Leoni, M. (2004(a)). Diffraction line profiles from polydisperse crystalline systems. *Acta Crystallographica A , 57* (5), 604-613.

[119] Scardi, P., & Leoni, M. (2006). Line profile analysis: pattern modelling versus profile fitting. *Journal of Applied Crystallography , 39* (1), 24-31.

[120] Scardi, P., & Leoni, M. (2002). Whole powder pattern modelling. *Acta Crystallographica A , 58* (2), 190-200.

[121] Scardi, P., Leoni, M., & Delhez, R. (2004(b)). Line broadening analysis using integral breadth methods: a critical review. *Journal of Applied Crystallography* (37), 381-390.

[122] Scardi, P., Leoni, M., Müller, M., & Di Maggio, R. (2010). In situ size-strain analysis of nanocrystalline ceria growth. *Materials Science and Engineering A, 528* (1), 77-82.

[123] Scherrer, P. (1918). Bestimmung der Grosse und der inneren Struktur von Kolloidteilchen mittels Rontgenstrahlen. *Nachrichten von der Koeniglichen Gesellschaft der Wissenschaften zu Goettingen, Mathematisch-Physikalische Klasse , 2*, 98-100.

[124] Sibson, R. (1980). The Dirichiet Tessellation as an Aid in Data Analysis. *Scandinavian Journal of Statistics , 7* (1), 14-20.

[125] Spencer, A. J. (1980). *Continuum Mechanics.* London: Longman Group UK.

[126] Stokes, A. R., & Wilson, A. J. C. (1942). A method of calculating the integral breadths of Debye Scherrer lines. *Mathematical Proceedings of the Cambridge Philosophical Society , 38* (3), 313-322.

[127] Stokes, A. R., & Wilson, A. J. C. (1944). The diffraction of X rays by distorted crystal aggregates - I. *Proceedings of the Physical Society , 56*, 174.

[128] Stukowski, A., Markmann, J., Weissmüller, J., & Albe, K. (2009). Atomistic origin of microstrain broadening in diffraction data of nanocrystalline solids. *Acta Materialia , 57* (5), 1648-1654.

[129] Suryanarayana, C., & Koch, C. C. (2000). Nanocrystalline materials – Current research and future directions. *Hyperfine Interactions , 130* (1-4), 5-44.

[130] Suzudo, T., & Kaburaki, H. (2009). An evolutional approach to the numerical construction of polycrystalline structures using the Voronoi tessellation. *Physics Letters A , 373* (48), 4484-4488.

[131] Takayama, Y., Furushiro, N., Tozawa, T., Kato, H., & Hori, S. (1991). A Significant Method for Estimation of the Grain Size of Polycrystalline Materials. *Materials Transactions, JIM , 32* (3), 214-221.

[132] Tanemura, M. (1988). Random packing and random tessellation in relation to the dimension of space. *Microscopy , 151* (3), 247-255.

[133] Tanemura, M. (2003). Statistical Distributions of Poisson Voronoi Cells in Two and Three Dimensions. *Forma , 18* (4), 221-247.

[134] Thomas, N. W. (1996). An extension of the Voronoi analysis of crystal structures. *Acta Crystallographica B , 52* (6), 939-953.

[135] Thomas, O. (2008). Diffraction analysis of elastic strains in micro and nanostructures. *Zeitschrift für Kristallographie , 223* (9), 569-574.

[136] Ting, T. C. T. (1996). *Anisotropic Elasticity: Theory and Applications.* New York: Oxford Science Pubblications.

[137] Tuzikov, A. V., Sheynin, S. A., & Vasiliev, P. V. (2003). Computation of volume and surface body moments. *Pattern Recognition , 36* (11), 2521-2529.

[138] Ungàr, T., Gubicza, J., Tichy, G., Pantea, C., & Zerda, T. W. (2005). Size and shape of crystallites and internal stresses in carbon blacks. *Composites Part A: Applied Science and Manufacturing , 36* (4), 431-436.

[139] Van de Weygaert, R. (1994). Fragmenting the Universe. 3: The constructions and statistics of 3-D Voronoi tessellations. *Astronomy and Astrophysics , 283* (2), 361-406.

[140] Van Houtte, P. (1993). Stress Measurements in Textured Materials. *Materials Science Forum , 133-136*, 97-110.

[141] Van Swygenhoven, H. (2002). Grain Boundaries and Dislocations. *Science , 296* (5565), 66-67.

[142] Van Swygenhoven, H., Farkas, D., & Caro, A. (2000). Grain-boundary structures in polycrystalline metals at the nanoscale. *Physical Review B , 62*, 831-838.

[143] Vitos, L., Ruban, A. V., Skriver, H. L., & Kollàr, J. (1998). The surface energy of metals. *Surface Science , 411* (1-2), 186-202.

[144] Wadell, H. (1935). Volume, Shape and Roundness of Quartz Particles. *Journal of Geology , 43* (3), 250-280.

[145] Wang, C., Liu, G., Wang, G., & Xue, W. (2007). Three-dimensional grain size distribution: Comparison of an analytical form under a topology-related rate equation with computer simulations and experimental data. *Materials Science and Engineering A , 454-455*, 547-551.

[146] Wang, Z. L., & Feng, X. (2003). Polyhedral Shapes of CeO2 Nanoparticles. *Journal of Physical Chemistry B , 107* (49), 13563-13566.

[147] Warren, B. E. (1955). A generalized Treatment of Cold Work in Powder Patterns. *Acta Crystallographica , 8*, 483-486.

[148] Warren, B. E. (1990). *X-Ray Diffraction* (Vol. 1). New-York: Dover.

[149] Warren, B. E. (1959). X-Ray Studies of Deformed Metals. *Progrress in Metal Physics , 8*, 147-202.

[150] Warren, B. E., & Averbach, B. L. (1950). The Effect of Cold-Work Distortion on X-Ray Pattems. *Journal of Applied Physics , 21*, 595-599.

[151] Warren, B. E., & Averbach, B. L. (1952). The Separation of Cold-Work Distortion and Particle Size Broadening in X-Ray Patterns. *Journal of Applied Physics , 23*, 497-498.

[152] Watari, M., McKendry, R. A., Vögtli, M., Aeppli, G., Soh, Y.-A., Shi, X., et al. (2011). Differential stress induced by thiol adsorption on facetted nanocrystals. *Nature Materials , 10*, 862-866.

[153] Wilkens, M. (1970). The determination of density and distribution of dislocations in deformed single crystals from broadened X-ray diffraction profiles. *Physica status solidi (a) , 2* (2), 359-370.

[154] Wilkens, M. (1969). Theoretical Aspects of Kinematical X-Ray Diffraction Profiles from Crystals Containing Dislocation Distributions. In R. de Wit, & R. Bullough (Ed.), *Fundamental aspects of dislocation theory. 2*, pp. 1195-1221. Washington: J. A. Simmons.

[155] Williamson, G. K., & Hall, W. H. (1953). X-ray line broadening from filed aluminium and wolfram. *Acta Metallurgica , 1* (1), 22-31.

[156] Wilson, A. J. C. (1962). *X-ray optics: the diffraction of X-rays by finite and imperfect crystals.* London: Methuen.

[157] Withers, P. J., & Bhadeshia, H. K. D. H. (2001). Residual Stress Part 1 - Measurement Techniques. *Materials Science and Technology , 17*, 355-365.

[158] Wu, Y., Zhou, W., Wang, B., & Yang, F. (2010). Modeling and characterization of two-phase composites by Voronoi diagram in the Laguerre geometry based on random close packing of spheres. *Computational Materials Science , 47* (4), 951-961.

[159] Xia, Y., Xiong, Y., Lim, B., & Skrabalak, S. E. (2008). Shape-Controlled Synthesis of Metal Nanocrystals: Simple Chemistry Meets Complex Physics? *Angewandte Chemie , 48* (1), 60-103.

[160] Xu, T., & Li, M. (2010). Geometric methods for microstructure rendition and atomic characterization of poly- and nano-crystalline materials. *Philosophical Magazine , 90* (16), 2191-2222.

[161] Xu, T., & Li, M. (2009). Topological and statistical properties of a constrained Voronoi tessellation. *Philosophical Magazine , 89* (4), 349-374.

[162] Xue, X., Righetti, F., Telley, H., Liebling, T. M., & Mocellin, A. (1997). The laguerre model for grain growth in three dimensions. *Philosophical Magazine B , 75* (4), 567-585.

[163] Yang, R. Y., Zou, R. P., & Yu, A. B. (2002). Voronoi tessellation of the packing of fine uniform spheres. *Physical Review E , 65*, 041320(1-8).

[164] Zeghadi, A., N'guyen, F., Forest, S., Gourgues, F., & Bouaziz, O. (2007(a)). Ensemble averaging stress–strain fields in polycrystalline aggregates with a constrained surface microstructure – Part 1: anisotropic elastic behaviour. *Philosophical Magazine , 87* (8-9), 1401-1424.

[165] Zeghadi, A., N'guyen, F., Forest, S., Gourgues, F., & Bouaziz, O. (2007(b)). Ensemble averaging stress–strain fields in polycrystalline aggregates with a constrained surface microstructure – Part 2: crystal plasticity. *Philosophical Magazine , 87* (8-9), 1425-1446.

[166] Zheng, G.-P., Gross, D., & Li, M. (2005). The effect of microstructure on magnetic phase transitions in an Ising model. *Physica A: Statistical Mechanics and its Applications , 355* (2-4), 355-373.

[167] Zheng, H., Cao, A., Weinberger, C. R., Huang, Y. J., Du, K., Wang, J., et al. (2010). Discrete plasticity in sub-10-nm-sized gold crystals. *Nature , 1* (144), 1-8.

[168] Zhu, B., Asaro, R. J., Krysl, P., Zhang, K., & Weertman, J. R. (2006). Effects of grain size distribution on the mechanical response of nanocrystalline metals: Part II. *Acta Materialia , 54* (12), 3307-3320.

[169] Zimmerman, J. A., Webb III, E. B., Hoyt, J. J., Jones, R. E., Klein, P. A., & Bammann, D. J. (2004). Calculation of stress in atomistic simulation. *Modelling and Simulation in Materials Science and Engineering , 12* (4), S319-S332.

Scientific Production

Modelling of Material Microstructures

1. "Realistic nano-polycrystalline microstructures: beyond the classical Voronoi Tessellation",
   Alberto Leonardi, Paolo Scardi, Matteo Leoni,
   Philosophical Magazine, 92 – 8 (2012) 986-1005.
   DOI: 10.1080/14786435.2011.637984
2. "Atomistic modelling of polycrystalline microstructures: An evolutional approach to overcome topological restrictions",
   Alberto Leonardi, Matteo Leoni, Paolo Scardi,
   Computational Materials Science, 67 (2013) 238-242.
   DOI: 10.1016/j.commatsci.2012.09.013

Analysis of Atomistic Simulation Data

3. "Microstrain in nanocrystalline samples from atomistic simulation",
   Alberto Leonardi, Kenneth Roy Beyerlein, Tao Xu, Mo Li, Matteo Leoni, Paolo Scardi,
   Zeitschrift für Kristallographie Proceeding, I (2011) 37-42.
   DOI: 10.1524/zkpr.2011.0005
4. "Strain in atomistic models of nanocrystalline clusters",
   Alberto Leonardi, Matteo Leoni, Mo Li, Paolo Scardi,
   Journal of Nanoscience and Nanotechnology, (2012) Accepted.

Intereference Effects in Nano-crystalline Systems

5. "Interference Effects in Nanocrystalline Systems",
   Alberto Leonardi, Matteo Leoni, Paolo Scardi,
   Metallurgical and MaterialsTransactions A,(2012) in press.
   DOI: 10.1007/s11661-012-1428-6

Common Volume Function & Diffraction Line Profile

6. "Common Volume Function and diffraction line profiles from polyhedral domains",
   Alberto Leonardi, Matteo Leoni, Stefano Siboni, Paolo Scardi,
   Journal of Applied Crystallography,45-6 (2012) 1162-1172.

Directional – Pair Distribution Function

7. "Atomistic interpretation of microstrain in diffraction line profile analysis",
   Alberto Leonardi, Matteo Leoni, Paolo Scardi,
   Thin Solid Films,(2012) in press.
   DOI: 10.1016/j.tsf.2012.05.037
8. "Directional Pair Distribution Function for diffraction Line Profile Analysis of atomistic models",
   Alberto Leonardi, Matteo Leoni, Paolo Scardi,
   Journal of applied Crystallography, (2012) submitted.

Nanocrystals under large hydrostatic pressure

9. "Diffraction-sensitive deformation of nanocrystals under large hydrostatic pressures"
   Michael Burgess, Alberto Leonardi, Matteo Leoni, Paolo Scardi,
   Powder Diffraction , (2012) in preparation.

Partecipation in
Congresses, Schools and Workshops

Materials Design Workshop
Trento (Italy) – 09.02.2010

8th European Conference on Residual Stresses (ECRS8)
Riva del Garda (Italy) – 26.06.2010

9th School Paolo Giordano Orsini
Trento (Italy) – 29.6.2010

12th European Powder Diffraction Conference (EPDIC12)
Darmstadt (Germany) – 27.08.2010
Poster presentation: *"Microstrain in nano-crystalline samples from atomistic simulation"*

E-MRS IUMRS ICAM 2011 Spring Meeting,
Nice (France) - 09.05.2011
Poster presentation: *"Strain in atomistic models of nano-polycrystalline clusters"*

II International Workshop on the Plasticity of Nanocrystalline Metals
Lake Bostal (Germany) – 25.09.2011
Poster presentation: *"Line broadening effect in X-ray Diffraction pattern from strain at the atomic level"*

Size Strain VI – Diffraction analysis of the microstructure of materials
Presqu'Ile de Giens, Hyères (Fraance) – 17.10.2011
Oral presentation: *"Atomistic interpretation of micro-strain effects in diffraction line profile analysis"*

Advanced Computational Methods Workshop
Trento (Italy) – 09.11.2011
Oral presentation:
"Computational efficiency in nano-polycrystalline microstructure modelling"

Escola de Altos Estudos em Cristalizacao e Cristalografia para America Latina (ECRISLA)
Florianopolis (Brazil) – 21.11.2011

Trento Innovation Conferences in Materials Engineering (TICME)
Trento (Italy) – 12.12.2011

13th European Powder Diffraction Conference (EPDIC13)
Grenoble (France) – 28.10.2012
Poster presentation:
"XRD line broadening effects in nanocrystals under hydrostatic pressure"

Implemented algorithms

Material Microstructures Modelling

1. SINGLE CRYSTAL MICROSTRUCTURE
2. POLYCRYSTALLINE MICROSTRUCTURE
    a. by Voronoi Tessellation
    b. by Modified Voronoi Tessellation
    c. by Laguerre Tessellation
    d. by Laguerre Voronoi Tessellation
    e. by Johnson-Mehl Tessellation
    f. by free Distance Function
    g. by collection of isolated particle

Reconstruction of nano-polycrytalline cluster from PBC

Atomistic Simulation Data Analysis

1. SURFACE MAP PROJECTION OF THE RADIAL DISTANCE FROM MASS CENTRE
2. NEIGHBOUR LIST DETECTION
3. SHELL INDEXING
4. LEVEL OF COORDINATION INDEXING
5. LOCAL CRYSTAL STRUCTURE DETECTION
6. LOCAL VORONOI CELL CONSTRUCTION
7. CRYSTAL CELL DEFORMATION ANALYSIS
8. VORONOI CELL DEFORMATION ANALYSIS
9. MASS VORONOI CELL DEFORMATION ANALYSIS (weighted and non-weighted)
10. EVOLUTIONARY VORONOI CELL DEFORMATION ANALYSIS
11. LOCAL POTENTIAL & KINETIC ENERGY COMPUTATION
12. LOCAL STRESS TENSOR ANALYSIS
13. DIRECTIONAL PAIR DISTANCE ANALYSIS

Common Volume Function Computation

1. SINGLE POLYHEDRAL SHAPES
2. COMPLEX MULTI-PARTICLE POLYHEDRAL SHAPES
3. HOLLOW AND NON CONVENTIONAL POLYEDRAL SHAPES

X-ray Powder Diffraction Modelling

1. DIRECT WILLIAMSON-HALL ANALYSIS FROM COMMON VOLUME FUNCTION
2. X-RAY POWDER DIFFRACTION PATTERN MODELLING
    a. by FOURIER TRANSFORM
    b. by POWDER INTEGRATION

Complementary algorithms

Acknowledgments

I have been really glad for the opportunity to attend the Doctoral School in Materials Science and Engineering. Despite my training in a different field such as architecture and civil engineering, I have been given the opportunity to grow and improve myself, by discovering a strong interest in materials science and computational physics. Hence, unsure of what awaits me in the future, I am particularly grateful to have overcome this challenge.

The support and inspiration of many people have allowed me to achieve the outcome of this thesis. In the first place, I would like to express my special gratitude and appreciation to my advisor Professor Paolo Scardi and co-advisor Professor Matteo Leoni for their essential guidance, support and valuable trust through the whole PhD course. They have provided for a brightening working group, where everyone has markedly shaped by useful discussions, international collaborations, and quest for excellence. I have also to thank a third mentor, Professor Mo Li, who has helped my understanding the basic of Molecular Dynamics simulations within a close collaboration, through fruitful exchanges of ideas and several intensive lectures.

Beyond traditional acknowledgments, I have to append an outstanding remark to Professor R. Di Maggio who allowed and pushed me to start the PhD, despite the significantly un-coherent background I had with material science and physic fields.

I would also like to thank all the colleagues and friends I have come to know during the past years for the friendly and inspiring co-operations. In particular for the helpful discussions and data supply, I am grateful to: L. Gelisio, K. R. Beyerlein, T. Xu, and M. Burgess. Furthermore, for the nice and fun time spent together in talking, eating and more, I am grateful to: C. L. Azanza Ricardo, M. Ortolani, G. Carlà, D. A. David, M. Müller, M. A. M Abdellatief, D. Regnicoli, C. Malerba, L. Rebuffi, M. Sukor Su'Ait, R. D'Angelo, R. Koch, M. D'Inkau and S. Setti.

Finally, I owe special gratitude to my family for continuously supporting all my undertakings, and encouraging my education. Last but not least, I have to save the most significant thank to my girlfriend A. Rosanna for her precious encouragement and help in overcoming the daily troubles. In developing my thesis, her listening and patience have been the most meaningful source.